Title
Synchrotron Vacuum-Ultraviolet Postionization Mass Spectrometry with Laser and Ion Probes for Intact Molecular Spatial Mapping of Lignin

Permalink
https://escholarship.org/uc/item/8j81249b

Author
Takahashi, Lynelle Kazue

Publication Date
2011

Peer reviewed|Thesis/dissertation

Synchrotron Vacuum-Ultraviolet Postionization Mass Spectrometry with Laser and Ion Probes for Intact Molecular Spatial Mapping of Lignin

by

Lynelle Kazue Takahashi

A dissertation submitted in partial satisfaction of the

requirements for the degree of

Doctor of Philosophy

in

Chemistry

in the

GRADUATE DIVISION

of the

UNIVERSITY OF CALIFORNIA, BERKELEY

Committee in Charge:

Professor Stephen R. Leone, Chair

Professor Gabor A. Somorjai

Professor Jan T. Liphardt

Fall 2011

Vacuum-Ultraviolet Postionization Mass Spectrometry with Laser and Ion Probes for Intact Molecular Spatial Mapping of Lignin

by

Lynelle Kazue Takahashi

Abstract

Vacuum-Ultraviolet Postionization Mass Spectrometry with Laser and Ion Probes for Intact Molecular Spatial Mapping of Lignin

by

Lynelle Kazue Takahashi

Doctor of Philosophy in Chemistry

University of California, Berkley

Professor Stephen R. Leone, Chair

A secondary ion mass spectrometer is coupled to a vacuum-ultraviolet (VUV) synchrotron beamline to perform neutral postionization experiments. The goal of the project is to develop a new molecule-specific imaging technique that can provide maximum chemical information of chemically heterogeneous samples while also maintaining information on their spatial distributions. Modifications are made to the beamline branchline to accommodate the new imaging instrument.

Initial experiments focus on the application of ion sputtering with VUV postionization to simple metal and semiconductor systems. From these experiments, VUV-secondary neutral mass spectrometry (VUV-SNMS) is established as a complementary imaging technique to SIMS. Signal intensities for select species are determined to be comparable to SIMS mass spectra, however VUV-SNMS signal intensities are more generally found to be limited by the low ionization cross sections of molecular analytes and low synchrotron flux. Despite this, it is observed that postionization significantly reduces the “matrix effects” that makes SIMS analysis difficult to quantitate. No significant differences were observed in the internal energies of atoms/clusters desorbed with different primary ions (Bi^+, Bi_3^+, and Bi_3^{2+}) from the photoionization efficiency curves of the sputtered atomic and cluster species. In atomic Au and As, no electronic excitation was observed.

Organic molecules are also investigated; however the non-electrically conductive nature of most organic surfaces leads to sample charging during VUV-SNMS analysis. To deal with this problem, a double pulse extraction scheme is developed. Organic test molecules thymine and tryptophan are examined and used as molecular thermometers to determine the approximate internal energies and temperatures of the ion-sputtered organics. By approximating the energies by two different methods, these molecules are found to have on the order of 2.5 eV to 3 eV of internal energy.

The feasibility of using VUV-SNMS for the study of lignin within plant systems is evaluated by studying the energetics and fragmentation mechanisms of coniferyl and sinapyl alcohol, two monomer units of the lignin polymer. The mass spectra are compared to those

obtained with positive mode secondary ion mass spectrometry (SIMS) and thermal desorption molecular beams (TDMB) mass spectrometry. While SIMS shows extensive fragmentation of the monolignols and a non-distinctive mass peak at the parent m/z, both TDMB and VUV-SNMS show prominent parent signal. Furthermore, it is found that many of the major VUV-SNMS peaks of the monolignols (m/z = 124 and 137) are observed in the TDMB mass spectra, suggesting that the fragments may arise due to dissociative photoionization of ion-sputtered molecular parent molecules. With the tunability of the synchrotron light, ionization energies of coniferyl alcohol are measured to be 7.60 eV ± 0.05 eV, and dihydrosinapyl and sinapyl alcohol were found to have ionization energies of <7.4 eV.

Alkali lignin from Sigma Aldrich is analyzed with VUV-SNMS. Extensive fragmentation is observed, and signatures from the monomer mass region provided the only characteristic ion signals in the mass spectra. Thus, while VUV-SNMS may be useful for probing monomer composition of lignin, it cannot provide much more chemical insight on lignin structure and how it changes upon different perturbations. Laser desorption is therefore developed in order to provide a desorption method that imparts less internal energy into the analyte molecules.

Lower internal energies can be achieved by using a nanosecond-UV desorption laser, which is applied to study coniferyl alcohol and lignin. As expected from previous VUV-laser desorption postionization (VUV-LDPI) work, coniferyl alcohol molecules are largely desorbed intact into the gas phase by minimizing the laser dosage and laser peak power. Similarly, when the laser is used to desorb molecules from the sample of alkali lignin, signatures in the dimer mass region appear. Several monomer masses are identified by their molecular weights and photoionization efficiency curves. Lignin dimers could not be assigned and are an area for much future work. Different mass spectral features are observed from different lignin extracts, illustrating that chemical differences between samples are reflected in the mass spectra. Preliminary results also suggest that it may be possible to follow the chemical changes that occur during laser pyrolysis of lignin and other important plant biopolymers.

For my family

Contents

List of Figures

List of Tables

Acknowledgments

Many people have helped me throughout my years in graduate school. First, I would like to acknowledge my advisor Professor Stephen R. Leone and my principal investigator, Dr. Musahid Ahmed for helping me to achieve depth and breadth in my research. From their combined guidance, they have helped me to achieve a balance in my work and to have a strong sense of purpose for my science.

I have had the opportunity to work with several great post-doctoral fellows in my years in Berkeley, including Dr. Leonid Belau, who was instrumental in the original design of the instrument setup, Dr. Jia Zhou, with whom I shared many night beam shifts, Dr. Oleg Kostko, who improved the laser desorption setup, and Drs. Suet-Yi Liu and Theresa Hofstetter, who have graciously accepted many beamline responsibilities during my dissertation writing.

I would also like to thank my collaborators in the Luke Hanley group (University of Illinois, Chicago) for many useful discussions and their patience in the first few years, as well as the Trent Northen Group (Lawrence Berkeley National Laboratory) for their support with MS/MS work. I would also acknowledge Dr. Hoi-Ying Holman for sharing her samples, enthusiasm for her science and many helpful discussions. For technical support, I would like to thank Corey Foster, Nathan Havercroft, Monroe Thomas, Felix Kollmer, and many members of the ALS support staff. Without the help of these individuals, the imaging project would likely not have progressed to the point it is now. Adam Bradford and Kathleen Fowler, the group administrative assistants, cannot be appreciated enough for their constant support behind the scenes. Last, but not least, I would like to thank my family, friends and the entire Leone group for their advice and support.

Chapter 1

Introduction

1.1 Motivation for New Neutrals Imaging Methods

Most chemical systems in nature are inherently heterogeneous. Plant cell walls, for example, are composed of several interacting polymers, including lignin, cellulose and hemi-cellulose. These polymers are not isotropically distributed throughout the sample, but occur in changing relative concentrations in different areas of tissue. Microbial species within biofilms have lipid membranes and may be embedded within polysaccharide and protein matrices. Atmospheric aerosols and soils can have both inorganic and organic layers, which react, mix, and age. Such systems involve complex heterogeneous chemical reactions, which can have dramatic ramifications in the areas of materials, renewable biofuels, geochemistry, global climate and health.

Understanding the chemical composition and transformation of such chemically heterogeneous systems is often difficult due to the many variables involved. In addition to understanding the chemistry of the individual chemical species, one must also understand the interactions between different components and their spatial and temporal characteristics. In such cases, bulk analyses such as mass spectral analysis of chemical extracts or purely spectroscopic investigations cannot provide comprehensive understanding of the chemical system. In order to visualize and understand the detailed chemistry taking place between individual components, imaging methods are necessary to provide simultaneously information of a sample's chemical composition and spatial heterogeneity.

1.2 Imaging the Chemistry of Plant Biomass Degradation

The breakdown of plant biomass into its constituent molecules is a complex process involving heterogeneous chemistry, and it is a problem that can be solved by the development of new imaging technologies. Plant biomass deconstruction is of interest due to the recent drive for developing renewable energy sources and converting plant lignocellulosic biomass into liquid fuels. Understanding the molecular transformations of plant biomass is crucial for improvement of the conversion process.

Plant material is a heterogeneous mixture composed of mainly cellulose, hemicelluloses and lignin. It can be converted into usable fuels in several different ways. Plant material can be directly burned to generate energy, or it can undergo partial combustion to make syn-gas (*i.e.*synthesis gas, a mixture of CO and hydrogen) or pyrolysis to produce biochar (*i.e.* charcoal). While these gaseous and solid fuel sources may be useful, arguably the most desirable type of energy product from plant biomass is liquid fuels such as biodiesel and bio-ethanol due to their potential use as transportation fuels. There is much debate on which source of renewable energy will dominate the future; however it is clear that each technology has barriers to its widespread use as an economically viable alternative to fossil fuels.

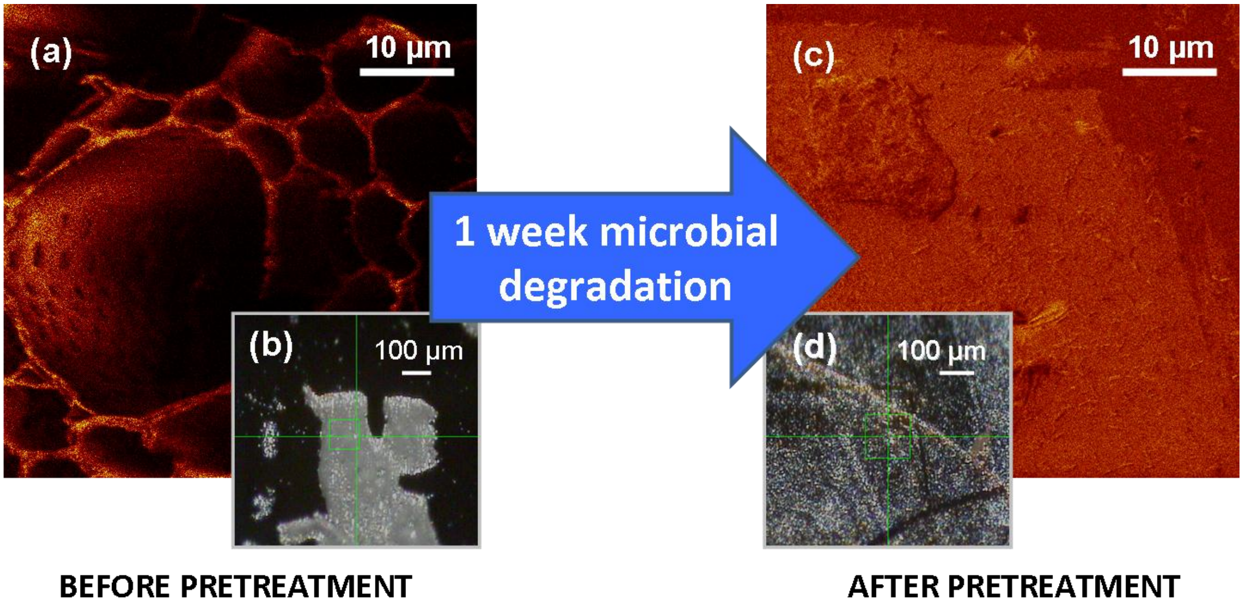

Figure 1.1: (a) Total positive secondary ion image of a section of *Miscanthus giganteus* and (b) zoomed-out optical image of the same section. (c) Total positive secondary ion image and (d) zoomed-out optical image of the biomass fragments that remain after one week of exposure to *Clostridium cellulolyticum.*

In the first step of converting plant biomass to ethanol, plant cellulose must be separated from the lignin and hemicelluloses. This step can be facilitated by physical, chemical, or biological pretreatments.[1] Figure 1.1 shows an example of a biological pretreatment of *Miscanthus giganteus* (a grass) by the microbe, *Clostridium cellulolyticum*. The images, taken during this work, illustrate the concept that while one week of exposure to the microbes results in a dramatic change in the plant tissue, one can perform chemical imaging of the sample in shorter time intervals to visualize the gradual chemical changes with molecular specificity.

During this first pretreatment step, lignin is a particularly problematic component in the plant tissue. It is a cross-linked polymer that closely interacts with cellulose and hemicellulose. It confers strength and rigidity to plants, but it also reduces the utility of biomass in paper pulping, livestock feeds, and biofuel production.[2] Efforts have been made to reduce plant lignin content, but such genetic modifications have sometimes been accompanied by severe reduction in plant growth. Such detrimental effects in plant growth can be clearly seen in total positive ion SIMS images taken during this work of thin sections of wildtype and lignin-deficient mutants of *Arabidopsis thaliana*, shown in Figure 1.2.

An alternative to reducing lignin content in plants is to develop efficient methods to degrade and separate the lignin from other plant components. To accomplish this task, it would be valuable to follow the chemistry as lignin is broken down during various pretreatment methods. Unfortunately, lignin is not homogeneously distributed in plants, and its chemical structure can vary spatially and temporally even within a given plant tissue.[3] Under these conditions, molecular information on small spatial length scales is also desirable to obtain a clear understanding of the chemical changes.

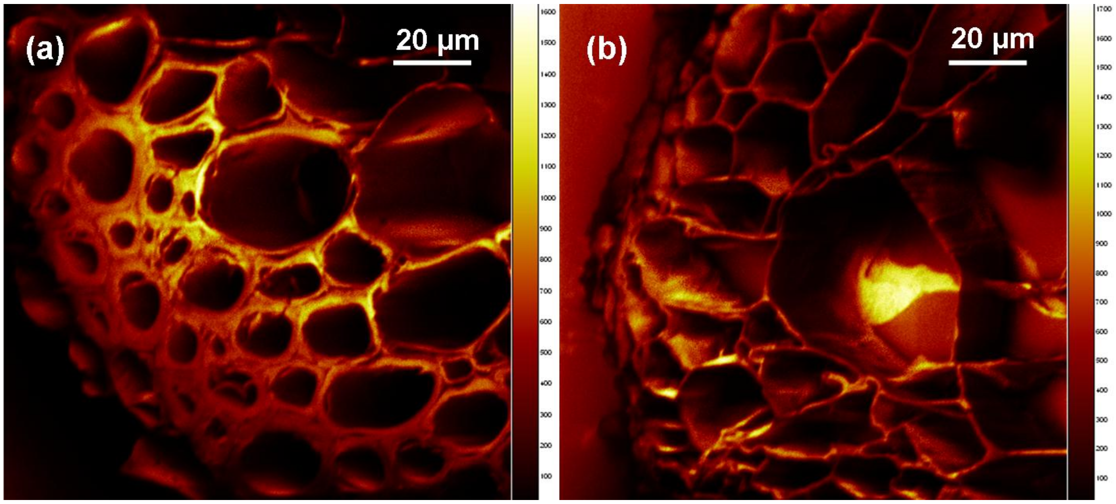

Figure 1.2: Total positive ion secondary ion images of a 125 µm x 125 µm field of view showing the structural differences between (a) wild-type *Arabidopsis thaliana* and (b) genetically modified lignin-deficient *Arabidopsis thaliana* mutant.

Molecular-specific imaging of plant biomass has been carried out using various methods. A comparative study of the lignin within wild-type and genetically modified lignin deficient Poplar wood have been carried out using Raman microscopy.[4] Very recently, imaging was performed with matrix-assisted laser desorption ionization with two stages of mass spectrometry (MALDI MS-MS) to study the distributions of cellulose and lignin in sections of poplar wood,[5] and it was shown that MS-MS methods can provide additional selectivity for imaging and distinguishing between compounds at the same mass-to-charge ratio. Secondary ion mass spectrometry (SIMS) has also been used to study the relative distributions of syringyl and guaiacyl lignin in poplar.[6] Despite this progress, further improvements are still necessary to perform chemical imaging of plant tissue with both sufficient molecular specificity and spatial resolution to facilitate understanding of chemical transformations within plant tissues.

In this dissertation, the development and application of two novel mass spectrometry techniques for imaging plant biomass undergoing chemical change are discussed. The development of these imaging techniques and the effect of the imaging probes on the detected molecules are discussed in detail in Chapters 2, 3, 4, and 6. The specific chemical signatures of two monomers of lignin (coniferyl and sinapyl alcohol) and their mechanistic origins are discussed in Chapter 5. The laser pyrolysis of isolated lignin polymers and model lignin compounds and the prospects for biomass imaging are discussed in Chapter 6.

1.3 Existing Methods for Imaging and Chemical Analysis

Many analytical techniques have been developed for studying the chemical composition of the natural world. These techniques often rely on extraction and separation methods, spectroscopy, and/or mass spectrometry. Methods like liquid chromatography-mass spectrometry (LC-MS) and gas chromatography- mass spectrometry (GC-MS) are generally used on sample extracts, where sample components are separated via chromatography and subsequently identified with mass spectrometry. Spectroscopic techniques like UV-Vis spectroscopy can be used to characterize samples by measuring their absorbance, while fluorescence characterizes samples by their radiative emission. Nuclear magnetic resonance (NMR) spectroscopy can selectively probe magnetic nuclei and distinguish atoms of the same type through differences induced by their local chemical environment.

These chemical analysis methods, while providing useful chemical information, do not provide a means to visualize their spatial context within the original systems. For this, imaging methods are necessary. Like chemical analysis methods, many methods exist for imaging samples with high spatial resolution, including atomic force microscopy (AFM) and electron microscopy. AFM is capable of high-spatial resolution images and probes the physical and mechanical properties of a sample.[7] Electron microscopy can be used to study systems with atomic resolution and can even be used to provide 3-dimensional structural information.[8] Ultimately, however, there is no molecule-specific information of organic components with these techniques.

Between these two extremes are methods that provide both chemical and spatial information, such as nuclear magnetic resonance (NMR) imaging, optical microscopy (e.g. Raman and X-ray imaging, and IR and fluorescence microscopy), and mass spectrometry imaging methods (e.g. MALDI, SIMS, and desorption electrospray ionization imaging). In the biological community, fluorescent probes like green fluorescent protein can be selectively attached to other proteins for subsequent imaging in an optical microscope. Infrared and Raman microscopy give information on chemical functional groups, while X-ray imaging techniques such as X-ray photoelectron spectroscopy (XPS) or extended X-ray absorption fine structure (EXAFS) spectroscopy are sensitive to elemental composition. NMR imaging can also be used to probe which chemical groups are present in the sample. MALDI imaging provides molecule-specific information for large biomolecules by mapping them spatially by their mass-to-charge ratio, while SIMS is used for high spatial resolution imaging of atomic species or small metabolites. Desorption electrospray ionization (DESI) imaging is used for higher-throughput imaging under ambient conditions, although with significantly reduced spatial resolution compared to SIMS.

For obtaining molecular information, mass spectrometry-based imaging techniques such as MALDI, SIMS and DESI have recently seen increased applications,[9] particularly in biological imaging.[10,11] SIMS is well-suited for the analysis of small molecules and high-spatial resolution imaging, and MALDI is best-suited for intact detection of large biomolecules such as proteins over larger length scales. Even these techniques, however, pose significant challenges: SIMS yields very complicated mass spectra due to molecular fragmentation of most chemical species; absolute quantification is difficult to obtain with MALDI and SIMS; DESI is limited to low-resolution imaging on length scales over 150 μm. Each of these techniques has its limitations, and none represents a universal imaging method with sufficient molecular specificity for all systems, molecular types or length scales.

The drawbacks of each of these imaging techniques severely limit the current chemical understanding of biomass undergoing chemical change. For this particular study, a spatial resolution better than 100 µm is desirable in order to visualize the chemical changes occurring in different areas of the plant. Furthermore, since matrix compounds can have structural similarities to lignin-like molecules (and they thereby contribute to mass spectral complexity), matrix-free imaging methods that can maintain high chemical information content (and molecular specificity) are preferable. The ability to obtain absolute concentrations of native molecules and their degradation products is also desirable. Since no existing imaging technique has effectively combined these qualities, a new imaging platform was developed at the Advanced Light Source at Lawrence Berkeley National Laboratory (LBNL).

1.4 Secondary Ion Mass Spectrometry (SIMS)

The imaging apparatus at LBNL is capable of performing analyses very similar to secondary ion mass spectrometry (SIMS). SIMS has recently gained ground in the area of molecular imaging. In SIMS, a high kinetic energy primary ion beam is focused onto the surface of interest. These high kinetic energy primary ions can be molecular (e.g. SF_5^+, coronene, phenylalanine), cluster (e.g. Bi_n^+, Au_n^+, C_{60}^+) or atomic (e.g. Ga^+, Ar^+) ions. In a time-of-flight (TOF) SIMS configuration (see Figure 1.3), compounds can be detected in parallel; thus one can obtain complete mass spectra for a given sample area in a relatively short time period. With a magnetic sector configuration, high mass resolution can be used to image isotope distributions of small mass fragments. Although a matrix can be used to enhance sputter and/or ionization yield, SIMS does not require the addition of matrix. As a result, samples can be observed with very little sample preparation that might otherwise disrupt their natural chemical distributions, and high spatial resolutions can be obtained, with a theoretical primary ion spot size lower limit of ~10 nm.[12]

These advantages have been exploited in the semiconductor industry, where SIMS has been used for depth profiling and mapping elemental species with high spatial resolution. Biological applications have increased over the years as well. Among its growing applications, SIMS has been used to study single cells,[13] mammalian tissue sections,[14] and microbial nitrogen fixation and symbiosis.[15]

As SIMS is pushed to higher spatial resolution, the amount of analyte per spatial pixel decreases. As a result, various methods have also been developed to enhance SIMS sensitivity. The development of cluster primary ion sources, silver cationization,[16] matrix addition,[17] and substrate modifications[18,19] have all been utilized in attempts to improve sensitivity for high-spatial resolution imaging.

Cluster and molecular primary ion sources have been widely adopted due to their higher sputter yields[20] and capability to induce less sample damage in the deeper layers of the probed material compared to atomic primary ion sources. Atomic ions induce individual collision cascades upon hitting the surface, while clusters induce a larger-scale process that results in nonlinear enhancements of the desorption yield with increasing cluster size. When the damage induced by the primary ion beam is removed at the same rate, the sample is left with no net accumulated damage and molecular depth profiling becomes possible. An extreme example of the use of clusters for ion sputtering is the recent development and commercialization of Ar_{2000} primary ion sources.[21]

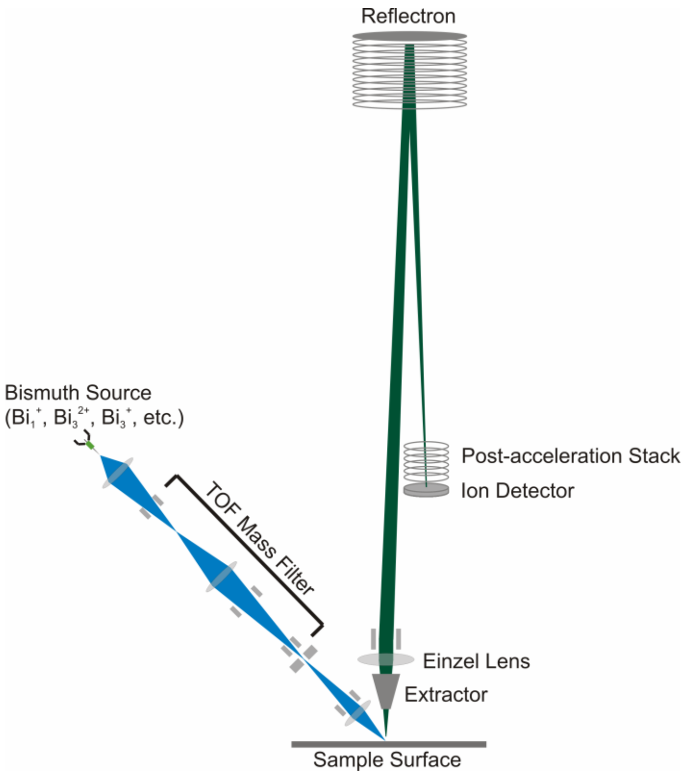

Figure 1.3: Schematic diagram of the time-of-flight secondary ion mass spectrometer.

In addition to overall sputter yield, the simplicity of the mass spectra obtained is also a major area of development since SIMS mass spectra are notoriously complicated from extensive molecular fragmentation. Recently, a new technique, termed gentle-SIMS (G-SIMS),[22] has been developed. In this technique, the fragmentation of a mass spectrum is associated with an effective plasma temperature, and this temperature varies with the energy and species of primary ion used for sputtering. The data can be extrapolated to conditions with low plasma temperatures, and the major peaks in the calculated G-SIMS spectrum are found to be characteristic of the material with little molecular rearrangement or fragmentation. Hybrid ion guns that emit multiple primary ion species are being developed for this purpose.[23]

Other techniques, such as nanostructure initiator mass spectrometry (NIMS) aim to both increase SIMS sensitivity and reduce molecular fragmentation. NIMS is a recently-developed imaging technique that can be used in combination with either a laser or ion probe.[19] Very briefly, a modified substrate with nanometer-scale pores is filled with an “initiator” substance which rapidly heats and ejects the overlying sample material. This method has been used to perform chemical imaging of a peptide array,[19] and it preserves the spatial distribution of chemical compounds within the sample due to the small size of the pores. The initiator decreases fragmentation and has also been demonstrated to increase sensitivity compared to normal SIMS.

Despite these inroads, SIMS does have disadvantages in that it is non-quantitative and suffers from “matrix effects”.[24] Because the sputtering and ionization event occur simultaneously, the local chemical environment within a surface can have dramatic effects on the combined sputter-ionization probability of a given chemical species. These imaging artifacts have been observed by many other groups as well as in experiments at the Chemical Dynamics Beamline.[25] Furthermore, high-kinetic energy primary ions are needed to obtain high spatial resolution images, inducing considerable sample damage and molecular fragmentation over more fragile, organic samples. These two factors make SIMS a challenging and non-quantitative chemical imaging technique for molecular identification in chemically heterogeneous systems such as plant biomass.

1.5 Synchrotron VUV-Secondary Neutral Mass Spectrometry (VUV-SNMS)

One method for dealing with the challenges of matrix effects in SIMS is to probe the neutral chemical species that are sputtered from the surface rather than the secondary ions. In this method, called secondary neutral mass spectrometry or SNMS, the ion-sputtered neutral species are postionized either by a laser[26] or electron source.[27] Such studies illustrate that the signal intensities of postionized neutrals do not fluctuate dramatically due to the local chemical environment. Furthermore, the ion-sputtered neutrals are found to greatly out-number the charged secondary ions that are normally formed by factors of 10^3 or even 10^6. Sampling postionized neutrals therefore yields mass spectra that are more reflective of the material leaving the sample, and it opens the possibility for enhanced sensitivity.

Despite the potential ability to eliminate matrix effects and enhance sensitivity by orders of magnitude, SNMS has not been applied widely to biological systems. Part of this has stemmed from the added difficulty of the experiments and the fragmentation observed within SNMS datasets. Due to a scarcity of laser sources in the energy range that is capable of performing single photon postionization of many organic molecules, many groups have relied on multi-photon ionization schemes (see Figure 1.4, red arrows),[28-30] which can deposit excessive energy into the already high internal energy ion-sputtered neutral molecules.

In 2004, Veryovkin and others developed a new method for SNMS, using a VUV free electron laser (FEL) light source.[31] This light source permitted tunable single photon ionization of the ion-sputtered neutral chemical species. While results over inorganic surfaces such as gold were promising, the technique was limited by the low 6 Hz repetition rate and limited wavelength tunability.

More recently, tunnel ionization has been used to postionize ion-sputtered neutral molecules.[32-34] With this technique, high-peak power laser fields are used to ionize ion-sputtered molecules. While this configuration can increase overall sensitivity of the parent ion compared to SIMS, fragmentation is still increased in many molecules analyzed.

In this dissertation, synchrotron VUV light is used as a postionization source. Synchrotron VUV is a ready source of wavelength-tunable radiation for performing single photon, near-threshold ionization of gas-phase molecules. Synchrotron radiation from the Advanced Light Source has a repetition rate of 500 MHz, making the radiation quasi-continuous. Early experiments performed on the Chemical Dynamics Beamline with an aerosol mass spectrometer suggested that the use of tunable synchrotron VUV can yield near fragment-free mass spectra for a wide variety of thermally-vaporized compounds, including beta-carotene (a long-chain hydrocarbon), phenylalanine-glycine-glycine (a tri-peptide), and the amino acid tryptophan.[35] Similar fragment-free mass spectra were obtained with VUV photoionization of collisionally-cooled DNA bases from a molecular beam.[36]

In VUV photoionization, a single photon takes a molecule directly from its neutral ground state to its molecular cation state (see Figure 1.4, blue arrow). When coupled to a gentle method for introducing molecules into the gas phase, tunable synchrotron VUV has been demonstrated to yield fragment-free mass spectra for fragile organic molecules.[35] Soft ionization methods such as this are valuable for the analysis of chemical mixtures by promoting parent ion detection and minimizing the complexity of the resulting mass spectrum. By coupling a local desorption technique with the well-defined process of VUV photoionization, a mass spectrometry-based chemical imaging technique with simplified mass spectra, high spatial resolution and improved quantification can be realized. While there are only a few light sources available in the VUV energy range,[37] synchrotron light sources can provide a unique source of collimated and wavelength-tunable VUV light that is well-suited for imaging applications.

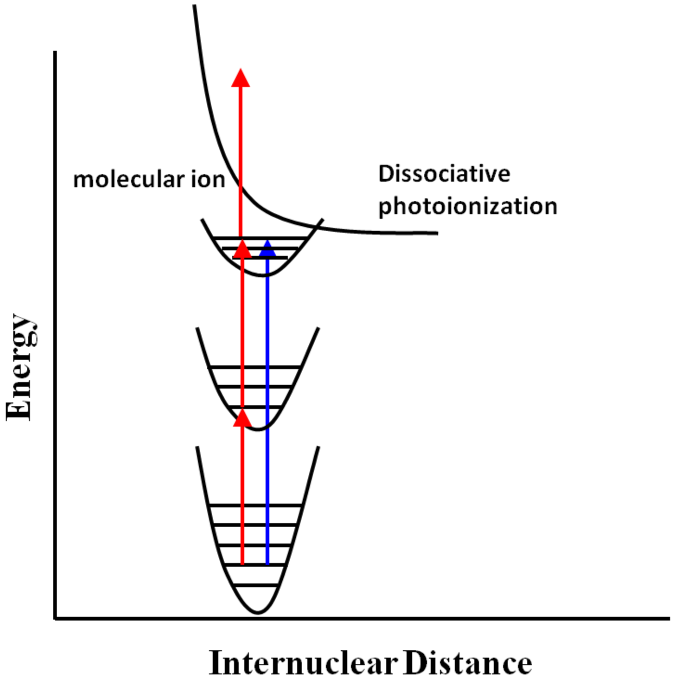

Figure 1.4: Schematic diagram illustrating the benefits of single photon ionization with vacuum-ultraviolet photons (blue arrow) compared to multi-photon ionization (red arrows), which can induce more molecular fragmentation.

Ion-sputtering with neutrals postionization using synchrotron-VUV radiation have been performed on inorganic materials (Chapter 3), model organic compounds (Chapter 4) and lignin-related compounds (Chapters 5 and 6). With the unique wavelength tunability of the synchrotron in the VUV spectral region, the fundamental molecular energetics involved during ion sputtering and ionization can be investigated with synchrotron VUV-SNMS. This coupling of SNMS with a synchrotron beamline has resulted in a new imaging technique that can provide noticeably simplified mass spectra over chemical mixtures such as plant biomass and a strengthened understanding of underlying molecular energetics upon ion sputtering.

1.6 Synchrotron VUV-Laser Desorption Postionization (VUV-LDPI)

Although synchrotron postionization methods can be successfully applied to detect ion-sputtered neutral molecules (see Chapters 3, 4 and 5), for very fragile molecules like large lignin polymers it is desirable to develop an imaging method that could preserve even more molecular information. For this, a softer desorption method is necessary that could release surface molecules with minimal input of internal energy and sample damage. A UV laser (Nd:YLF, 349 nm) probe is used for this purpose.

While the laser cannot be focused as tightly as the ion probe, laser desorption postionization has many advantages and can be used for complementary imaging over larger length scales. Like SIMS and VUV-SNMS, VUV-LDPI often does not require the application of matrix. In addition, with proper control over desorption conditions, it is possible to desorb higher molecular weight species from surfaces with less than half the internal energy that is observed in neutral molecules released via ion sputtering.[38] Mass spectra therefore contain much more chemical information that is reflective of the original sample under investigation. The application of VUV-LDPI to lignin is discussed in Chapter 6.

References

(1) Cheng, J. J.; Timilsina, G. R. *Renewable Energy*, *36*, 3541.

(2) Li, X.; Chapple, C. *Plant Physiology*, *154*, 449.

(3) Boerjan, W.; Ralph, J.; Baucher, M. *Annual Review of Plant Biology* **2003**, *54*, 519.

(4) Schmidt, M.; Schwartzberg, A. M.; Perera, P. N.; Weber-Bargioni, A.; Carroll, A.; Sarkar, P.; Bosneaga, E.; Urban, J. J.; Song, J.; Balakshin, M. Y.; Capanema, E. A.; Auer, M.; Adams, P. D.; Chiang, V. L.; Schuck, P. J. *Planta: An International Journal of Plant Biology* **2009**, *230*.

(5) Lunsford, K. A.; Peter, G. F.; Yost, R. A. *Analytical Chemistry*, null.

(6) Zhou, C.; Li, Q.; Chiang, V. L.; Lucia, L. A.; Griffis, D. P. *Analytical Chemistry*, null.

(7) Jalili, N.; Laxminarayana, K. *Mechatronics* **2004**, *14*, 907.

(8) Downing, K. H.; Sui, H.; Auer; Manfred. *Analytical Chemistry* **2007**, *79*, 7949.

(9) Amstalden van Hove, E. R.; Smith, D. F.; Heeren, R. M. A. *Journal of Chromatography A*, *1217*, 3946.

(10) Watrous, J. D.; Dorrestein, P. C. *Nat Rev Micro*, *advance online publication*.

(11) Vickerman, J. C. *Analyst*, *136*, 2199.

(12) Liebl, H. *Microchimica Acta* **1978**, *69*, 241.

(13) Fletcher, J. S.; Lockyer, N. P.; Vaidyanathan, S.; Vickerman, J. C. *Analytical Chemistry* **2007**, *79*, 2199.

(14) Sjövall, P.; Johansson, B.; Lausmaa, J. *Applied Surface Science* **2006**, *252*, 6966.

(15) Lechene, C. P.; Luyten, Y.; McMahon, G.; Distel, D. L. *Science* **2007**, *317*, 1563.

(16) Grade, H.; Winograd, N.; Cooks, R. G. *Journal of the American Chemical Society* **1977**, *99*, 7725.

(17) Liu, L. K.; Busch, K. L.; Cooks, R. G. *Analytical Chemistry* **1981**, *53*, 109.

(18) Nayak, R.; Knapp, D. R. *Analytical Chemistry*, *82*, 7772.

(19) Northen, T. R.; Yanes, O.; Northen, M. T.; Marrinucci, D.; Uritboonthai, W.; Apon, J.; Golledge, S. L.; Nordstrom, A.; Siuzdak, G. *Nature* **2007**, *449*, 1033.

(20) Nagy, G.; Walker, A. V. *International Journal of Mass Spectrometry* **2007**, *262*, 144.

(21) Matsuo, J.; Okubo, C.; Seki, T.; Aoki, T.; Toyoda, N.; Yamada, I. *Nuclear Instruments and Methods in Physics Research Section B: Beam Interactions with Materials and Atoms* **2004**, *219-220*, 463.

(22) Gilmore, I. S.; Seah, M. P. *Applied Surface Science* **2000**, *161*, 465.

(23) Green, F. M.; Kollmer, F.; Niehuis, E.; Gilmore, I. S.; Seah, M. P. *Rapid Communications in Mass Spectrometry* **2008**, *22*, 2602.

(24) Kollmer, F.; Bourdos, N.; Kamischke, R.; Benninghoven, A. *Applied Surface Science* **2003**, *203*, 238.

(25) Takahashi, L. K.; Zhou, J.; Wilson, K. R.; Leone, S. R.; Ahmed, M. *The Journal of Physical Chemistry A* **2009**, *113*, 4035.

(26) Arlinghaus, H. F. Laser Secondary Neutral Mass Spectrometry (Laser-SNMS). In *Surface and Thin Film Analysis*; Wiley-VCH Verlag GmbH & Co. KGaA; pp 179.

(27) Kopnarski, M.; Jenett, H. Electron-Impact (EI) Secondary Neutral Mass Spectrometry (SNMS). In *Surface and Thin Film Analysis*; Wiley-VCH Verlag GmbH & Co. KGaA; pp 161.

(28) Möllers, R.; Terhorst, M.; Niehuis, E.; Benninghoven, A. *Organic Mass Spectrometry* **1992**, *27*, 1393.

(29) Müller, U.; Schittenhelm, M.; Schmittgens, R.; Helm, H. *Surface and Interface Analysis* **1999**, *27*, 904.
(30) Terhorst, M.; Möllers, R.; Niehuis, E.; Benninghoven, A. *Surface and Interface Analysis* **1992**, *18*, 824.
(31) Veryovkin, I. V.; Calaway, W. F.; Moore, J. F.; Pellin, M. J.; Lewellen, J. W.; Li, Y.; Milton, S. V.; King, B. V.; Petravic, M. *Applied Surface Science* **2004**, *231-232*, 962.
(32) Willingham, D.; Brenes, D. A.; Winograd, N.; Wucher, A. *Surface and Interface Analysis*, *43*, 45.
(33) Willingham, D.; Brenes, D. A.; Wucher, A.; Winograd, N. *Journal of Physical Chemistry C*, *114*, 5391.
(34) Willingham, D.; Kucher, A.; Winograd, N. *Chemical Physics Letters* **2009**, *468*, 264.
(35) Wilson, K. R.; Jimenez-Cruz, M.; Nicolas, C.; Belau, L.; Leone, S. R.; Ahmed, M. *J. Phys. Chem. A* **2006**, *110*, 2106.
(36) Belau, L.; Wilson, K. R.; Leone, S. R.; Ahmed, M. *The Journal of Physical Chemistry A* **2007**, *111*, 7562.
(37) Akhmetov, A.; Moore, J. F.; Gasper, G. L.; Koin, P. J.; Hanley, L. *Journal of Mass Spectrometry*, *45*, 137.
(38) Kostko, O.; Takahashi, L. K.; Ahmed, M. *Chemistry – An Asian Journal* **2011**, *6*, 3066.

Chapter 2

Instrumental Configurations and Experimental Techniques

2.1 General Instrument Description: ToF.SIMS V

A commercial time-of-flight secondary ion mass spectrometer (ToF.SIMS V, IonTOF, Inc.) was installed at the vacuum ultraviolet (VUV) Chemical Dynamics Beamline, on a non-monochromatized terminal (Terminal 2), of the Advanced Light Source in December 2007. The original instrument configuration is schematically depicted in Figure 1.3. By coupling this commercial SIMS apparatus to the beamline, an ion sputtering and synchrotron VUV postionization imaging technique was established. The imaging capabilities were later extended to include laser desorption imaging with postionization.

2.1.1 Basic Configuration and Detection Scheme

The TOF.SIMS V is modified from its original design to facilitate postionization experiments and to accommodate later additions to experimental equipment. Additional flanges have been added to the main chamber, which have since been used to add a desorption laser and electron gun. The instrument is also configured such that the high voltage rack is separate from the main body of the instrument in order to fit within the tight spatial constraints of the beamline floor. Further modifications have been made to the internal components of the analyzer, including the enlargement of apertures before the Einzel lens and at the entrance of the reflector plates, and the complete removal of an aperture immediately before the post-acceleration stack.

The instrument consists of a 2-meter time-of-flight (ToF) mass spectrometer, held under ultra-high vacuum (10^{-9} to 10^{-10} mbar) conditions. The chosen ion sputtering probe is a bismuth liquid metal ion gun (LMIG), which can operate in several modes, depending on the analysis type. Samples are held on one of three sample holders, the choice of which is also dependent on the analysis desired. The holders are introduced into the main chamber from the loadlock chamber via a magnetic coupling, which slides the holder onto the sample stage.

The TOF.SIMS V is currently operated via the SurfaceLab 6.1 software package. The instrument operates on a master trigger generated by the instrument's main computer. In standard SIMS operation, the LMIG directs 25 keV primary ions (mass-selected for the primary ion of choice) to a surface and sputter-ionizes atomic and molecular species from the sample of interest. The sample is held at ground potential while the secondary ions are introduced into the analyzer by either a constant (DC) or pulsed extraction voltage applied to the cone-shaped extraction electrode. It is here that the secondary ions (either positively or negatively charged) are accelerated into the analyzer. The analysis region is shown in Figure 2.1.

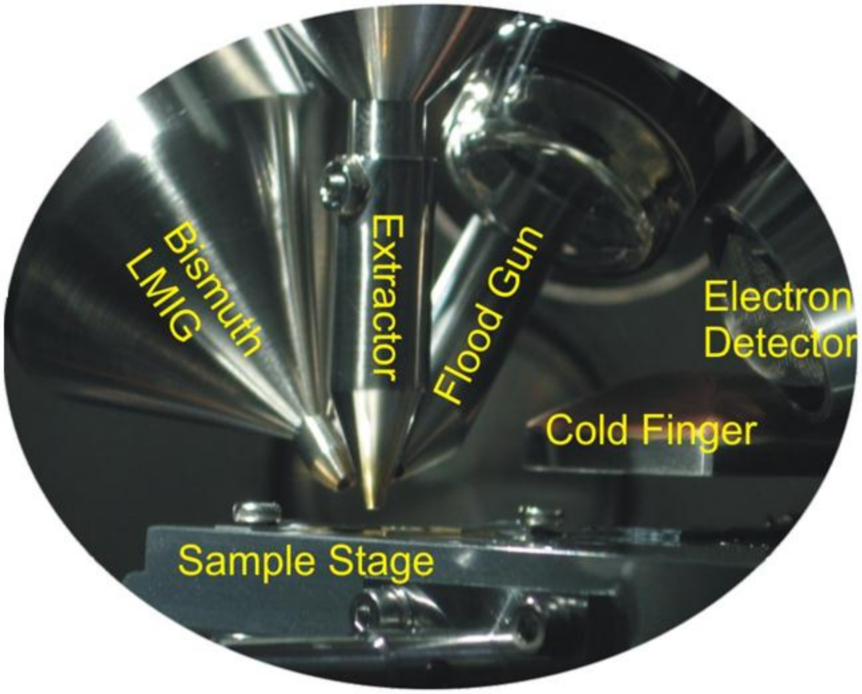

Figure 2.1: Labeled photograph of the analysis region, indicating the major components, including the sample stage, liquid metal ion gun probe and cone-shaped extractor electrode.

In a ToF mass spectrometer, all ions with the same charge state are extracted with the same kinetic energy. This constant kinetic energy means that atomic / molecular ions with different m/z will arrive at the detector at separate times. In a linear ToF, the expression relating the mass of an ion to its detection time is (assuming a single charge) given by:

$$t = L\sqrt{\frac{m}{2E}} + C \tag{2.1}$$

where t is the measured arrival time at the detector, L is the path length traveled, m is the mass of the molecule, E is the extractor voltage, and C is a constant time offset (all in standard units).

In the ToF.SIMS V instrument, there is a reflectron to perform additional time focusing of the ions onto the detector (Figure 2.2). The voltage of the variable drift path (VDP) plate can be adjusted to change the time focus of the ions on the detector. The original VDP plate has two separate holes for entering and exiting ions; however a modified plate with a single, larger hole is currently installed to reduce losses of postionized neutrals. After the reflectron, ions are post-accelerated toward a multi-channel plate (MCP) detector. The electrons generated by the MCP impact a scintillator, which converts the electrons to photons, which are then detected by a photomultiplier tube. Ions are detected in time bins of 100 ps and are recorded as 0 or 1 counts. Both negative and positive ions can be detected, but only one polarity can be sampled at a time.

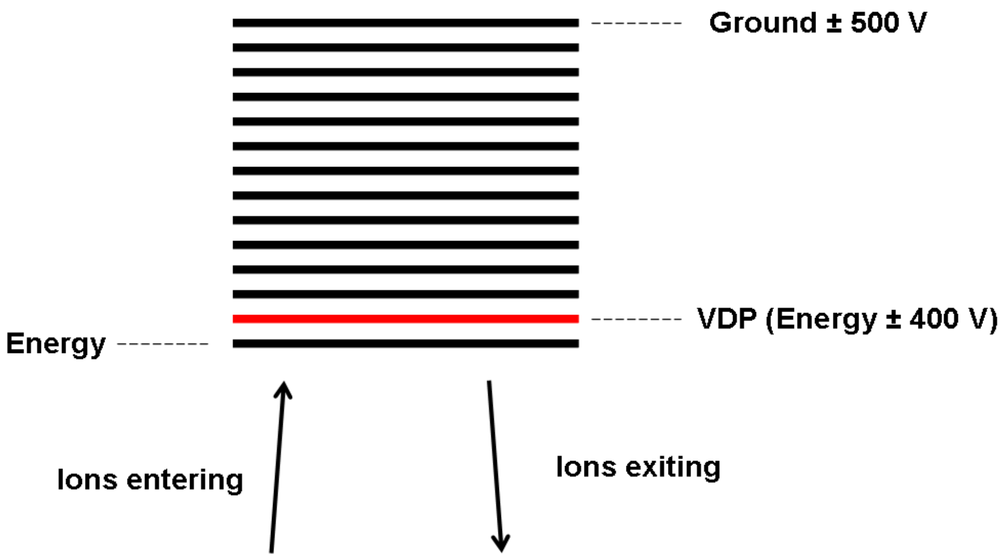

Figure 2.2: Schematic diagram of the reflectron stack, showing the placement of the variable drift path plate (red).

Under normal SIMS operation, ions fly through the time-of-flight tube with 2000 eV of kinetic energy, and the mass resolution is determined largely by the topography of the sample and the width of the primary ion pulses. The analyzer conditions can be adjusted to increase the mass resolution by lowering the kinetic energy of extracted ions (*e.g.* 1000 eV instead of 2000 eV). In this way, the time spread between masses is increased, thus improving the mass resolution. This change in the energy voltage in the ToF also requires adjustment of the lens voltage, reflectron voltage, and VDP voltage.

2.1.2 Bismuth Cluster Liquid Metal Ion Gun and Electron Flood Gun

The bismuth LMIG can emit mass-selected ions with 15 keV to 25 keV of kinetic energy. The mass selection is achieved by a small time-of-flight region within the ion column. The maximum pulse width that can be used for a given Bi_n^{m+} cluster is determined by the time separation between that cluster and the other cluster cation species that are closest in mass-to-charge ratio (m/z).

There are several choices for the primary ion species that can each be run within a range of kinetic energies. With the bismuth LMIG, one may choose primary ions such as Bi^+, Bi_3^{2+}, Bi_2^+, Bi_5^{2+}, Bi_3^+, Bi_7^{2+}, Bi_4^+ and Bi_5^+. There is a set of voltage settings for the ion gun that is specific to each cluster, each mode of operation and each kinetic energy. Most experiments in this dissertation are performed using Bi_3^+, which has a relatively high primary ion current and the benefits of a cluster primary ion (see Section 1.4).

For any given primary ion species, the LMIG can operate in several different modes such as burst-alignment (BA) mode, extreme imaging (*i.e.* collimated) mode, high-current bunched mode, and high-current unbunched mode. Each operating mode of the ion gun has a different spatial resolution, mass spectral resolution, and primary ion current. The general characteristics of each of the most commonly used modes are summarized in Table 2.1.

	DC current	Mass Resolution	Pulse Width	Spatial Resolution	Applications
High-current (un)bunched	14 nA	11,000	~1 ns (15-25 ns)	5 µm (2 µm)	Quick analyses and high mass-resolution
Burst Alignment	0.4 nA	Nominal mass	~100 ns	250 nm	Imaging
Extreme Imaging (i.e. collimated)	50 pA	Nominal mass	~150 ns	110 nm	Imaging

Table 2.1: Liquid metal ion gun modes of operation for 25 keV bismuth source.

The most standard modes of operation are the high-current modes. “High-current unbunched” mode is the starting point from which all other modes for the LMIG are optimized. It has high primary ion current, can be optimized to have a spot size of ~2 µm, and is useful for rapid acquisition of mass spectra. Primary ions are not bunched in time, resulting in relatively broad peak shapes compared to high-current bunched mode. “High-current bunched” mode, as the name implies, has characteristics of high primary ion current and ion pulses that are bunched in time, which results in higher mass resolution. The typical current for high-current bunched Bi_3^+ primary ions is ~0.4 pA at 10 kHz. This mode of operation can be optimized to have a minimum spot diameter of ~5 µm and a H^+ peak width of under 1 ns.

BA mode provides moderate primary ion current (~30x less than high-current bunched) with significantly improved spatial resolution on the order of ~250 nm; however the mass resolution that can be obtained is nominal mass only. Extreme imaging mode can be optimized to have ~100 nm spatial resolution, however, like BA mode, it is limited to nominal mass only. Extreme imaging mode has even lower primary ion current than BA mode (~10x less current than BA mode); thus in addition to probing a much smaller volume per image pixel, data acquisition takes much longer for reasonable signal-to-noise chemical images.

The LMIG can be rastered over a desired area of the sample with a specified raster pattern, pixel density and number of scans. For imaging areas larger than 500 µm x 500 µm, it is possible to perform stage rastering. Pixel density, raster pattern and number of scans are dependent on the spot size of the ion beam, the signal or image quality desired for a given mass, ion gun stability, as well as the damage threshold for the sample. To obtain higher signal-to-noise ratios in images, pixel binning can be applied during analysis at the cost of spatial resolution. To obtain the best spatial resolution image for a given LMIG spot size, over-rastering (overlapping pixels) is required.

Since the ion beam deposits positively charged ions onto the sample surface, less conductive samples (*e.g.* Teflon) can accumulate charge. This can cause decreased detection efficiency for the produced ions since the sample itself acts as a ground electrode in the overall detection scheme. Because negative ion mode pushes positively charged species back to the surface, charging is generally worse in negative ion mode than in positive ion mode. Charging can manifest as areas without signal in an image, rapid movement of ion intensity distributions during an analysis, or rapid signal decay. To compensate for accumulated positive charges, an electron flood gun can apply low kinetic energy (0 eV to 25 eV) electrons to the surface between primary ion pulses. The electron current and kinetic energy can be controlled through software; however even low-energy electrons can damage certain samples, and the electron beam spot size is > 1 mm, which can damage large areas of sample.

2.1.3 Sample Holders

There are three sample holders that can be used: the "top-loading", "bottom-loading" and "heating / cooling" (H/C) sample holders. With the top-loading sample holder, samples are clamped to the holder from the top surface. This is most useful for large samples or for any samples where postionization analysis is desired, as it permits maximum flexibility and allows the synchrotron light to pass as close to the sample surface as possible.

The "bottom-loading" sample holder contains slots over which a face-plate with smaller slots is placed. Small samples of about 1 cm^2 can be placed and bolted from the bottom. This holder is generally restricted to SIMS analysis since it has been found that the top-plate forces the VUV beam to be sufficiently far away from the sample surface to dramatically reduce the synchrotron postionization signal intensities for ion-sputtered neutrals.

The H/C sample stage is used exclusively when heating or cooling of a sample is necessary (see Figure 2.3). It can only be used with small samples ~ 1 cm^2 and is the most cumbersome to work with due to the fact that it must physically touch a cold-finger inside the

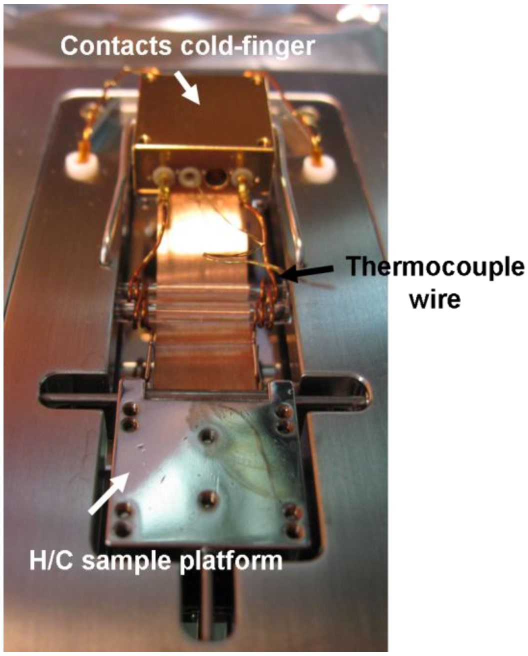

Figure 2.3: Heating/cooling stage. The brass-colored block contacts the liquid-nitrogen cooled cold-finger in the loadlock and/or main chambers. A thermocouple wire is placed under the sample to monitor the temperature.

main chamber when the sample is in the analysis region. Moving to a new position on the sample thus requires the sample to first be lowered, so that the coupling does not touch the cold-finger, before moving in the lateral (x and y) directions. A cold finger in the loadlock chamber allows the option of heating or cooling samples before its introduction to the main chamber, which is valuable for volatile compounds. Baking the H/C stage with the intended substrate before introducing the sample is useful for eliminating contaminants when the H/C stage is used for thermal desorption experiments.

2.2 The Synchrotron Beamline

2.2.1 Beamline Hardware and Vacuum-Ultraviolet Radiation

The VUV radiation used for the imaging experiments is located at Terminal 2 of the Chemical Dynamics Beamline (Beamline 9.0.2) at the Advanced Light Source (ALS). The ALS is a third-generation synchrotron light source and user facility. Electron bunches travel around in the synchrotron storage ring at near-relativistic speeds. The ring is composed of multiple straight sections, and the section for Beamline 9.0.2 is equipped with a 10-cm period undulator. The undulator is a series of magnets of alternating polarity that perturbs the path of the electrons, thus producing radiation. The wavelength of the radiation can be tuned by adjusting the gap between the magnets.

The spectrum of the undulator covers a wide range of energies. In order to improve the spectral resolution of the light, the horizontal beam defining aperture (HBDA) and vertical beam defining aperture (VBDA) slits are used to sample only part of the radiation cone. These two sets of slits can be optimized in both position and width to cut off the radiation beam such that the radiation bandwidth is reduced from its normal value of 0.35 eV (see Figure 2.4a, blue triangles) to 0.2 eV (see Figure 2.4a, black circles). The HBDA and VBDA positions and widths are optimized for spectral resolution and desired flux by using the monochromator on Terminal 3 of the beamline. In some experiments, the HBDA and VBDA may be narrowed to reduce the overall photon flux in the ionization region of the imaging apparatus and avoid detector saturation.

After passing the HBDA and VBDA, the synchrotron radiation passes through a rare gas higher-harmonic filter. Typically, the gas filter is filled with argon gas, which filters radiation above its ionization energy (IE) of 15.7 eV and allows lower energy light to pass through. Krypton (IE 14 eV) and helium (IE 24.6 eV) can also be used, depending on the wavelengths of light desired in an experiment. Within the gas filter, there is a linear translator with two horizontal slits (200 µm and 100 µm width) that can be used to narrow the photon beam. Use of the smaller slit reduces the photon flux at the imaging endstation only slightly, and it has been shown to improve the spatial profile of the synchrotron beam. The optimized beam profiles in the vertical and horizontal directions are shown in Figures 2.4 b and c.

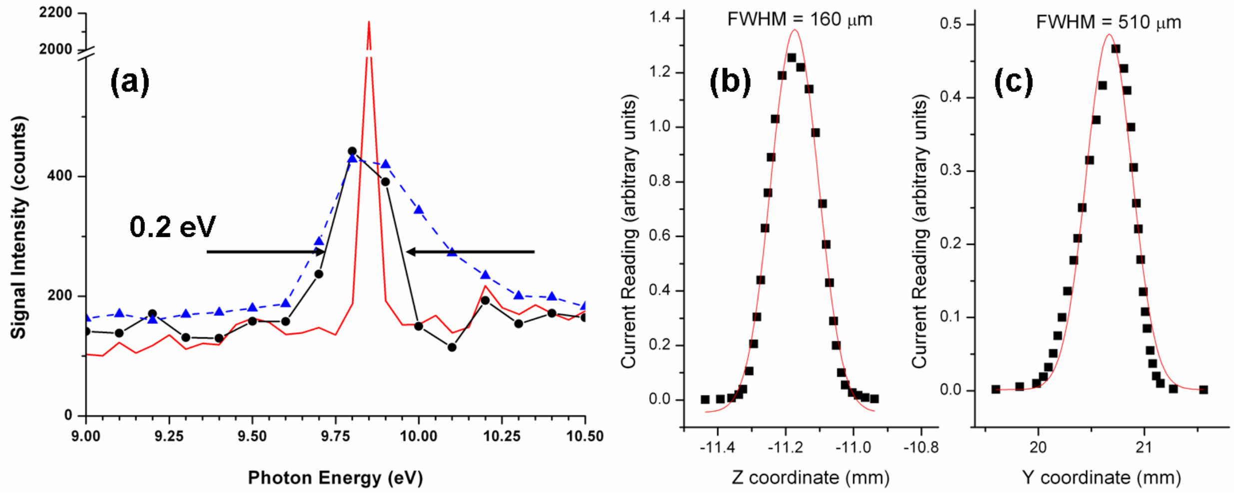

Figure 2.4: (a) The high-resolution spectrum of the silicon autoionizing resonance taken on Terminal 3 (red), the resonance of ion-sputtered Si taken on Terminal 2 before (blue triangles) and after (black circles) insertion of the gas filter slit and optimization of the horizontal and vertical beam defining apertures, showing improved spectral resolution of 0.2 eV. The optimal vertical (b) and horizontal (c) spatial profiles of the synchrotron beam after addition of the 100 µm slit.

After passing through the gas filter, the synchrotron radiation is reflected by a gold toroidal mirror (M4X) and directed to the imaging end station at Terminal 2. Along the path are two linear manipulators equipped with 1 mm-thick and 2-mm thick MgF_2 windows. MgF_2 effectively absorbs flux above ~10 eV and can significantly reduce the effects of residual higher harmonics; however the use of MgF_2 windows sacrifices photons. At 9.5 eV, signal counts from ion-sputtered As_2 were decreased by ~55% by the introduction of only 1 mm of MgF_2 to the beam path. In the ionization region, the photon beam (with 100 µm slit in the gas filter) measures ~200 µm (vertical) by ~500 µm (horizontal) and provides ~ 10^{15} photons per second under normal operation (500 mA, top-off mode, no MgF_2).

2.2.2 Imaging Branch-line

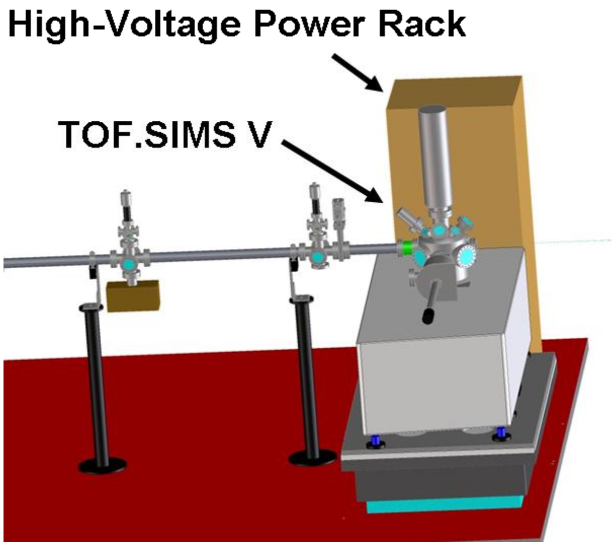

Figure 2.5: Schematic diagram of the imaging apparatus coupled to the 9.0.2.2 branchline.

Modifications have been made to the synchrotron beam line in order to accommodate the new imaging endstation. Because VUV radiation cannot propagate through air, an evacuated beam pipe connects the synchrotron directly to the TOF.SIMS V. The transmission of vibrations from the beamline to the high-spatial resolution imaging apparatus is minimized by coupling to the beam pipe through vibration-isolating bellows.

Vibration tests of the beamline floor reveal that floor vibrations from foot traffic and nearby doors can blur high-spatial resolution (~100 nm) images during data collection. A cooling pump near the shielding wall of the synchrotron ring is also found to be a major vibration source higher upstream in the beamline, although this source of vibration does not appear to affect instrument performance during postionization experiments.

To address sources of vibrations close to the instrument, the TOF.SIMS V is mounted on a platform (Figure 2.5). The concept for the vibration-isolation platform is based on a design from Dr. David Kilcoyne (Beamlines 5.3.2 and 10.0.1). A two-inch layer of Dow “Square Edge” polystyrene foam is used as a base, and it is compressed by a granite block. Atop the granite block is a ~1.46-inch layer of “Chockfast Red” grout, onto which a 1” thick aluminum plate is secured. The entire granite assembly is restricted from lateral motion in the event of an earthquake by the presence of four stainless steel bumpers, which are bolted to the experimental floor.

The instrument is supported on top of this assembly by three floating vibrationally isolating legs that use house air. The absolute height of the instrument can be adjusted by a regulator on the bottom back panel of the instrument. Other legs on the instrument that are not air damped do not touch the floor during normal operation. These legs are fastened to the foundation by bumpers, which catch the legs in the event of tipping or violent shaking due to an earthquake.

In order to facilitate alignment of the synchrotron beam to the small ionization region in the imaging instrument, control of the direction of the synchrotron beam must be achieved. Two linear stepper motors have been added to the platform supporting the vacuum housing of the last reflecting mirror (M4X; gold-plated toroidal mirror). The two motors control the yaw and the roll of the mirror, allowing adjustment of the lateral deflection and the vertical positioning of the synchrotron beam, respectively. With the current stepper motor configuration, changes in the M4X roll by +0.0001 mm correspond roughly to a change of ~7 µm in the downward direction in the ionization region of the instrument. Similarly, a change of +0.001 mm in the M4X yaw corresponds to a change of ~30 µm in the beam position in the lateral position to the left (in the same direction as the beam, not looking into the beam).

2.3 Vacuum-Ultraviolet Secondary Neutral Mass Spectrometry

In VUV-SNMS, ion-sputtered neutrals are released from a sample surface by primary ion bombardment, and they are photoionized by synchrotron radiation before detection by ToF mass spectrometry. The application of VUV-SNMS to the study of inorganic materials and organic molecular species is discussed in Chapters 3-6. In this section, the experimental details of VUV-SNMS experiments are discussed in more detail.

2.3.1 Data Collection Scheme: Metals and Semiconductor Materials

When neutrals are sputtered from a surface, they have a kinetic energy distribution. This distribution results in a spread in the time when the neutral species first interact with the synchrotron beam, which passes a finite distance above the surface. Since the ionization conditions are far from saturation and the photon beam has a finite vertical dimension, some neutrals may ionize from photons arising at the bottom of the synchrotron beam profile, while others may ionize closer to the top of the beam profile. This results in both a temporal and spatial spread of when and where post-ions (*i.e.* postionized neutrals) are formed.

The spatial spread of the postionized neutrals results in a spread in the kinetic energies of the post-ions as they fly through the ToF analyzer. This energy spread is a result of the current extraction configuration (see Figure 2.6). The sample is held at ground, while an extractor electrode directly above the sample surface is held at -2000 V, extracting positively charged post-ions into the analyzer region. Ions formed at the surface receive the full 2000 eV of kinetic energy from the extractor-surface potential difference, while neutrals that are postionized at positions further away from the surface receive a smaller kinetic energy kick.

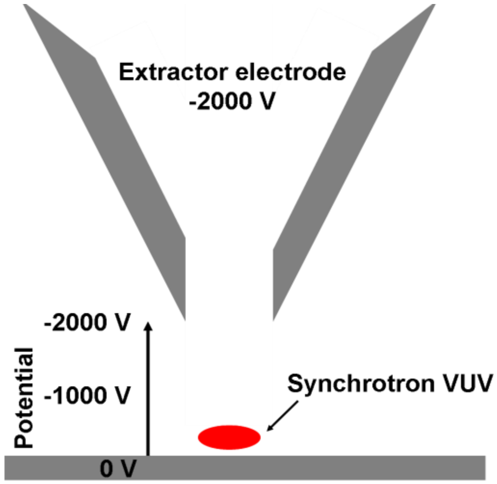

Figure 2.6: Schematic diagram illustrating how spatial spread can result in a distribution in kinetic energy through the ToF analyzer.

This kinetic energy spread is compensated by the additional time focusing of the reflectron stack; however there is no current compensation for the different time of formation for the cations formed from postionization. As a result, in such a continuous extraction (DC) scheme, in which the extractor voltage is constantly on, broad postionization mass peaks result. Over a flat InAs surface, the effective mass resolution at m/z 150 (As_2) is typically ~110 using 50 ns primary ion pulse widths. This peak broadness and the relatively low intensity of postionized neutral signal intensities compared to secondary ion signals requires the suppression of SIMS ions and the optimization of post-ions.

For metal and semiconductor surfaces, much of the SIMS background can be eliminated by sputter cleaning the surface with a direct current of primary ions. Here, oxide layers and other contaminants that might otherwise enhance secondary ion formation are removed. This significantly simplifies the mass spectra and can reduce the signal intensity of the main element even in single-component surfaces such as a silicon wafer. The spectral differences of a silicon wafer before and after sputter cleaning (2 cleaning scans) are shown in Figure 2.7.

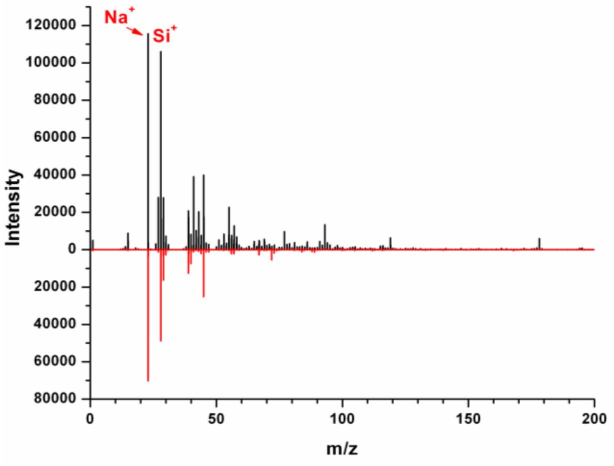

Figure 2.7: Mass spectra of a silicon wafer before (black) and after (red) sputter cleaning by a constant current of primary ions.

Even with sputter-cleaning, however, increased selectivity for post-ions is necessary. In early experiments, it was found that SIMS ions, being extracted immediately upon formation at the surface, have a much narrower kinetic energy spread. As a result, in positive ion mode, the reflectron voltage could be adjusted to -20 V (compared to the usual +20 V) to significantly suppress the detection of SIMS ions. This change in voltage permits the higher kinetic energy SIMS ions to penetrate deeper into the reflectron, until they collide with the top plate in the stack of electrodes. At the same time, since post-ions travel through the analyzer with lower kinetic energy, optimal spatial focusing of post-ions onto the detector requires a lower lens voltage (by a couple hundred volts). These optimization conditions are also discussed in Chapter 3.

While these modifications effectively suppress SIMS background and increase VUV-SNMS signal, SIMS counts still greatly outnumber VUV-SNMS counts for most samples; thus it is necessary to manually subtract the secondary ion signal contributions. Three data files are taken to obtain a single postionization mass spectrum: one with only the LMIG (so-called “g file”), one with the synchrotron only (“s file”), and one with both the synchrotron and the LMIG (“sg file”). By taking the difference (sg – g – s), the true postionization signal can be extracted. Since SIMS datasets are very sensitive to matrix effects (and therefore to the depletion of surface contaminants), there may be fluctuations in the SIMS contribution between the sg and g files. This effect can be further minimized by averaging several series of postionization datasets.

Due to the low signal counts arising from post-ions, the alignment of the synchrotron VUV with respect to the plume is critical. In general, signal intensities are highest with the synchrotron passing as close as possible to the sample (~30 µm to 75 µm between the sample surface to the center of the VUV beam). This constraint makes flat samples desirable since uneven surfaces result in large signal fluctuations and/or inadvertent VUV irradiation of the sample surface.

For some samples, ionization of thermally desorbing molecules can provide a significant source of background signal in the s file, even with sample cooling. In such cases, synchrotron background can be reduced by shortening the extraction pulse applied to the extractor cone electrode. Since the extraction pulse length cannot be tuned directly through the SurfaceLab 6.1 software, separate power supplies (Bertan Associates, Inc. Model 205B-05R), pulsing units (DEI Model PVX-4140) and delay generators (Stanford Research Systems, Inc. Model DG535) are also used to create modified ion extraction schemes for optimal detection of photoionized neutrals from laser and thermal desorption and ion sputtering. With these electronics, the extraction delay and duration can be controlled, and multi-pulse extraction schemes can also be used (see Section 2.3.2).

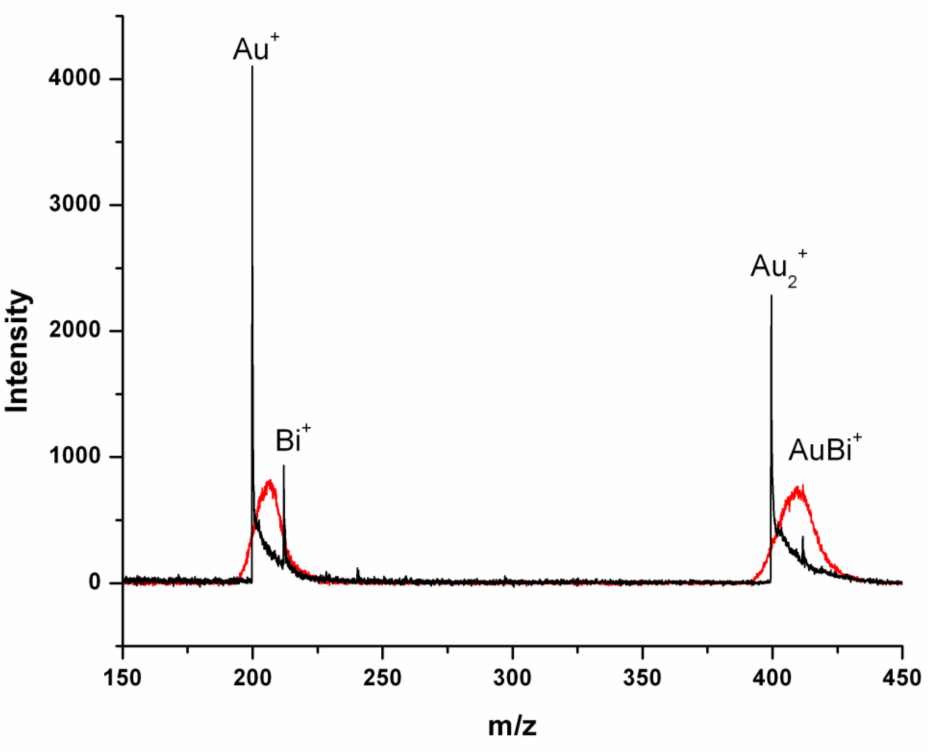

Figure 2.8: Two VUV-SNMS peaks of a gold sample with constant extraction (red). Improved mass resolution is obtained with a delayed extraction scheme (black).

Mass resolution of VUV-SNMS peaks can be improved significantly by delaying the extraction pulse. By delaying the extraction pulse for secondary neutrals by about < 1 µs after the ion gun pulse hits the surface, the neutrals are given time to ionize and accumulate in the extraction region. The accumulated post-ions are then all extracted at the same time (this reduces the time spread arising from the photoions having different times of birth), and the reflectron can compensate for the remaining spread in kinetic energy through the analyzer (*i.e.* spatial spread). Figure 2.8 shows the effect of delaying the extraction pulse for a gold surface. As can be seen from the figure, the mass resolution is enhanced from ~100 to ~1000, making the peaks sharper and easier to identify over the SIMS background (background is not shown in the figure).

2.3.2 Data Collection Scheme: Organic Samples

For organic molecules, the above mentioned DC extraction schemes do not work reliably. Due to the electrically insulating nature of most organic molecules, the samples charge very rapidly upon primary ion bombardment. Also, due to the fragility of the organic molecules and their degradation upon continuous ion beam exposure, the practice of sputter cleaning cannot be used.

Charging is a major problem for the analysis of organic materials with VUV-SNMS; however the problem is least noticeable when using the DC extraction scheme. In the DC extraction scheme, electrons and negative ions formed by primary ion bombardment or by the synchrotron beam are constantly being pushed back to the surface by the constant potential on the extractor cone. The extraction pulse thus provides a constant source of negative charges that can compensate for the deposition of positive charges by the primary ions. For some samples, little to no charging is observed with a DC extraction scheme.

A VUV-SNMS mass spectrum of thymine using a DC extraction scheme is shown in Figure 2.9. The raw (unsubtracted) sg file is shown in red, and the raw g file is shown in black. There are no obvious signs of charging in the mass spectrum; however the use of DC extraction does not sufficiently suppress the secondary ion contribution, and the post-ions appear only as broad tail features on each of the SIMS peaks. In order to make the postionization signal more obvious, it would be desirable to further suppress the secondary ion contribution and to increase the mass resolution of the detected post-ions.

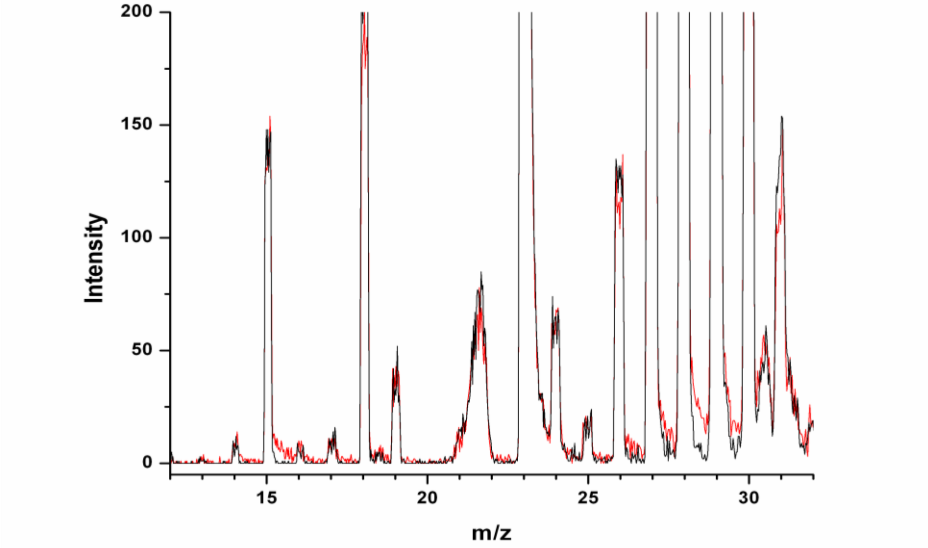

Figure 2.9: The raw mass spectra showing the low mass secondary ion contribution (black) from thymine. The spectrum arising from synchrotron and ion gun together is shown in red. The red tails near the baseline of the secondary ion signals are the broad postionization features obtained with constant extraction.

From experiments with metal and other inorganic samples, it is known that delaying the extraction pulse can significantly improve the mass resolution. While this addresses the problem of the low mass resolution of VUV-SNMS signals, using a delayed extraction pulsing scheme for organic samples exacerbates charging problems. Figure 2.10 shows a mild case of charging for thymine with a delayed extraction pulse. In panel 2.10a, the SIMS contribution (the g file, orange trace) is enhanced compared to the SIMS contribution to the sg file (black) at low masses. On the other hand, at higher masses (Figure 2.10b), the relative intensity of the g file is lower than the sg file, as would expected if there were neutral postionization contributions. Due to the peculiar behavior at lower masses, however, it is unclear whether this apparent postionization signal is due to charging or whether it represents true post-ion signal. In the subtracted spectrum (sg-g-s), shown in panel 2.10c, the mass-dependent effects of charging are clear from the apparently negative postionization signals from the scan-to-scan intensity variations of the secondary ion signals.

The exacerbation of charging with a delayed extraction scheme can be explained by the lack of immediate charge-compensation. Secondary ions are formed very close to the surface, and since they have charge, they immediately feel the effects of any stray electric fields. With continuous extraction, the excess positive charge on the sample created by the primary ions is immediately compensated by electrons and negatively charged species being pushed back toward the surface; however with delayed extraction, the charge compensation is not applied for at least several hundred nanoseconds. During this time, secondary ions are deflected from their normal path and their detection efficiency fluctuates. The mass dependence of this effect may arise due to the fact that heavier cations travel slower and are less sensitive to the stray electric fields.

As was mentioned in Section 2.1.2, sample charging can manifest in several ways during SIMS analysis such as low-signal intensity areas within an image, rapid movement of ion intensity distributions during an analysis, or rapid signal decay. In VUV-SNMS analysis, sample charging has an even greater effect since it affects several different populations of charge: secondary ions (positive and negative charges), photoionized neutrals (sputtered or neutrals from background gas), as well as electrons produced from both the sputtering and ionization events.

In VUV-SNMS, one naturally expects a postionization signal that is greater than or equal to zero at any given m/z. When charging occurs, however, this simple subtraction breaks down. When the g file is being collected, sample charging may be more severe than when the sg file is being collected since the sg file has additional charge-neutralizing electrons being generated via the ionization of ion-sputtered neutrals or background gas. This could make the SIMS contribution of the sg file higher than in the g file. On the other hand, it is possible that the synchrotron is slightly grazing the surface and generating even more charge build-up at the sample surface, which would make the secondary ion contribution to the g file appear to have higher signal intensities than in the sg file. Thus, in VUV-SNMS analysis, sometimes the apparent postionization signals resulting from the subtraction (sg-g-s) are grossly exaggerated or show negative intensity, as in Figure 2.10.

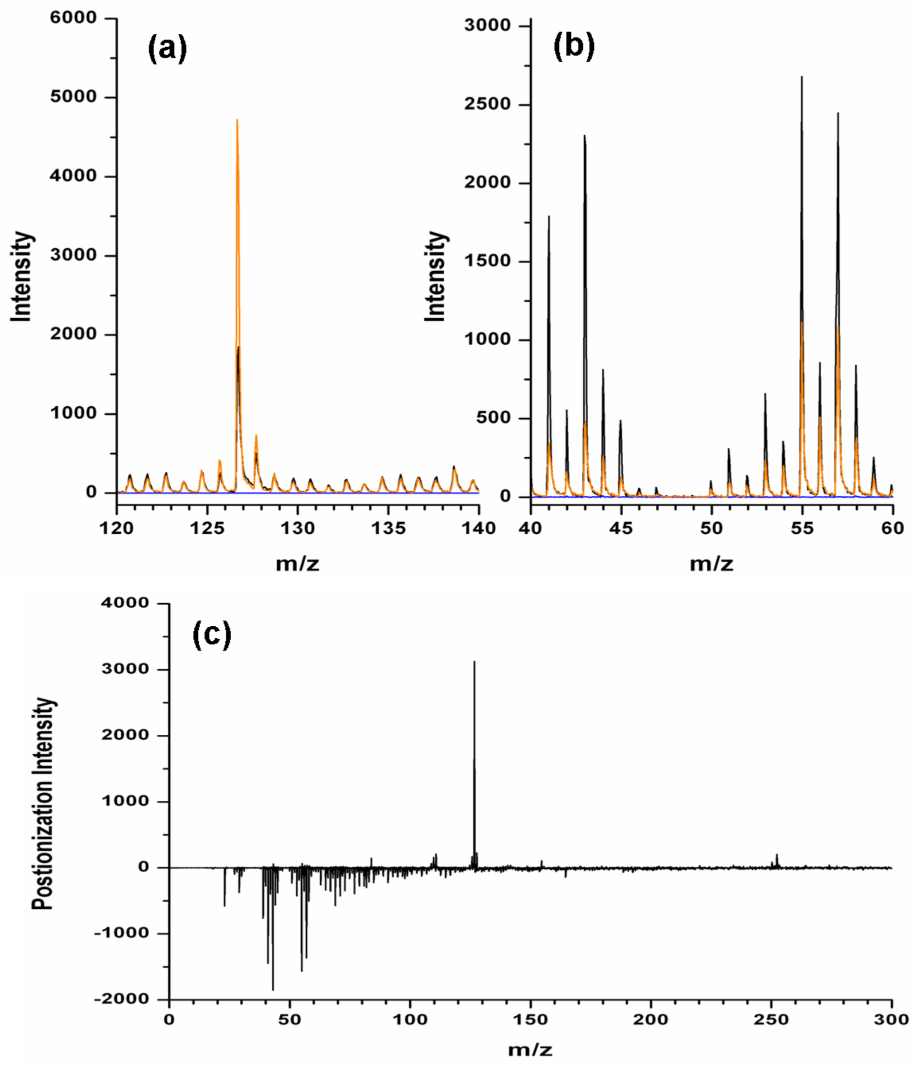

Figure 2.10: (a) Low mass range of VUV-SNMS raw data files, showing enhanced SIMS signals on the thymine sample. The g data file is shown in orange, the sg data file is shown in black, and the contribution of the s data file is negligible (blue baseline). (b) Higher mass range signals show decreased SIMS signals. (c) The subtracted mass spectrum (sg-s-g), which shows apparently negative postionization contribution at low masses.

In order to deal with this problem, a new pulsing scheme was developed, which would maintain the charge compensating characteristics of DC extraction while also offering the higher mass resolution of delayed extraction. In this hybrid, double pulsing extraction scheme, shown in Figure 2.11, the primary ions hit the surface during the first extraction pulse, which is applied from $t = t_0$ to a. During this time, the negative secondary ions and electrons are pushed back toward the surface to perform charge compensation, while the positive ions are partially extracted toward the extractor cone. Immediately after the last of the primary ions have hit the surface, the extraction voltage is returned to zero, during which time ion-sputtered neutrals interact with the VUV beam, become ionized and accumulate in the ionization region. At t = b, the second extraction pulse is applied. From t = b to t = c, any residual secondary cations and the photoionized neutrals are extracted and detected by the detector.

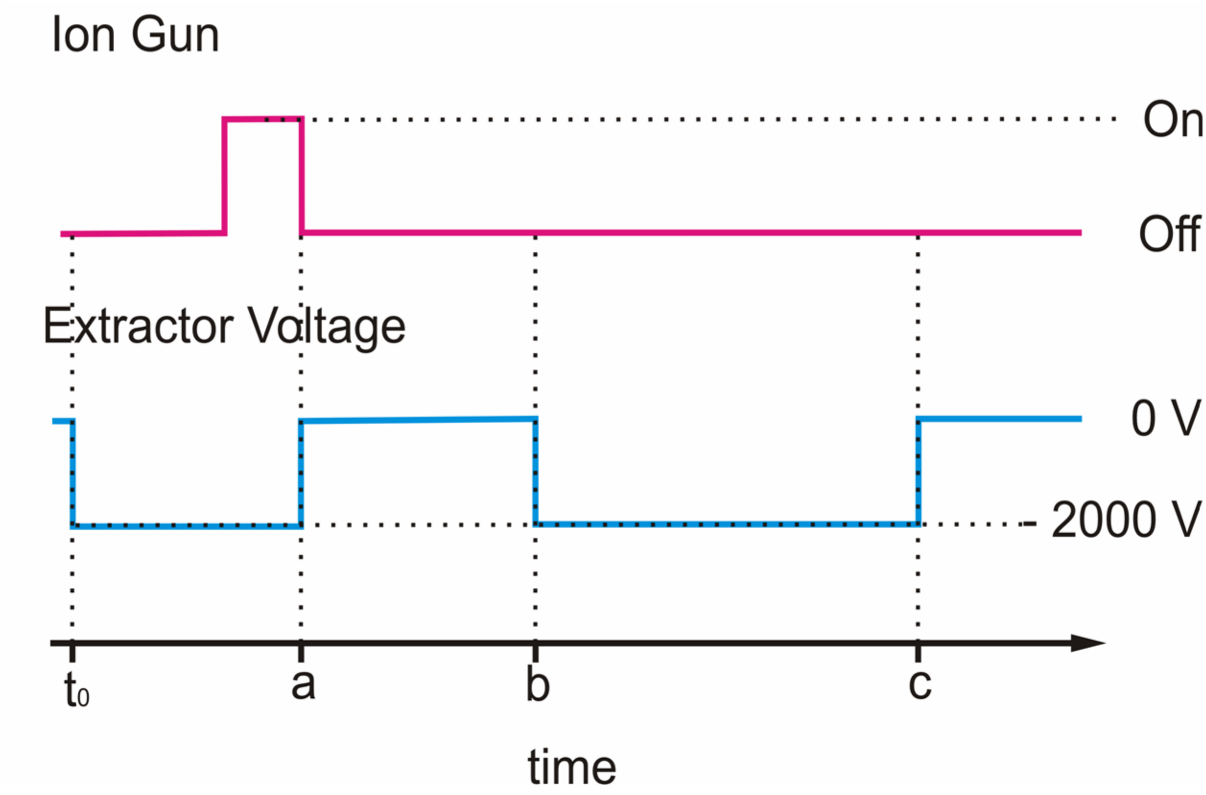

Figure 2.11: Timing scheme for extraction of postionized organic neutrals. At t_0, the first -2000 V extraction voltage (blue, bottom) is applied to the extractor cone. During this time, the primary ion pulse (pink, top) hits the surface. After the last of the primary ions have hit the sample surface by t = a, the extraction pulse is turned off (voltage = 0 V). The extraction pulse is turned on again from t = b to t = c.

The double pulsing scheme effectively reduces the charging effects such that VUV-SNMS signals are clearly discernable in many cases; However, some residual charging effects remain, as is evident by the persistence of negative signal fluctuations in the VUV-SNMS mass spectra of many organic molecules, including those shown in Chapters 4 and 5. Also, SIMS suppression is not 100% effective, so collection of three files (sg, s, and g) are still required to perform a subtraction. Improved SIMS suppression may be accomplished either by changing the relative magnitude of the two extractor pulses so that secondary ions can be more effectively filtered out by the reflectron, or, alternatively, the direction of the first extraction pulse can be changed so that the secondary ions are deflected in a different path.

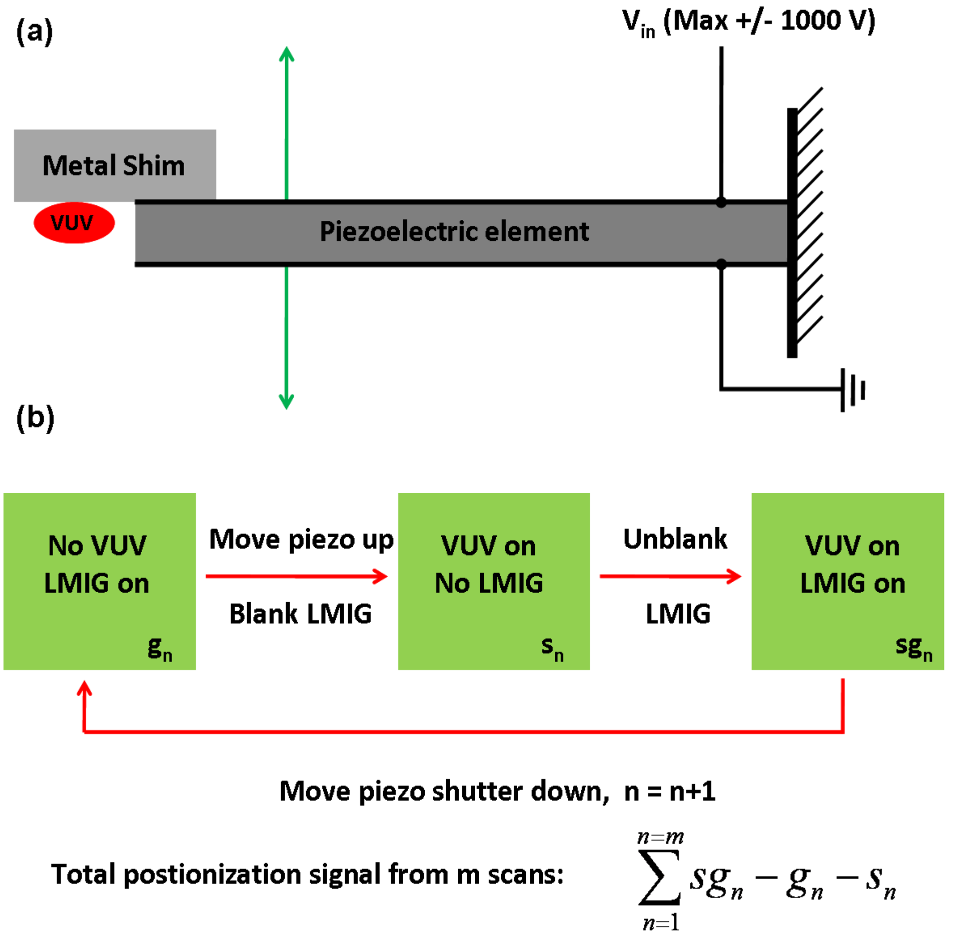

Figure 2.12: (a) A schematic diagram of the piezo chopper and (b) the data collection scheme.

While the double pulsing scheme works reasonably well, further reduction of charging effects can be achieved by interlacing the collection of the s, g and sg data files. In this way, the charging effects can be almost completely averaged away. This averaging method can be done manually, which can be tedious, or by the use of a piezo light chopper to modulate the synchrotron beam. In this configuration, a piezo element with a metal strip for a beam block is modulated up and down just upstream of the imaging endstation. The chopper is used to collect sg, s and g datasets one scan at a time. In this configuration, the synchrotron light can be quickly blocked and unblocked for relatively quick collection of sg, g, s files. Unfortunately, while this method does effectively average out charging effects, the data analysis is more cumbersome. Since charging is always an issue during VUV-SNMS analysis of organic samples, however, an improved software interface may be pursued to develop a practical interlaced data collection method.

2.3.3 Sample Preparation

The best samples for VUV-SNMS are electrically conductive and flat (very little sample topography). For investigations of organic molecules, however, most samples can be considered neither flat nor conductive. To account for this, organic samples should be kept as thin and flat as possible. For maintaining sample flatness, silicon wafers work as relatively inexpensive sample substrates. A thin layer of organic molecules can then be deposited onto the silicon wafers.

When making a thin layer of organics for VUV-SNMS analysis, experimental evidence suggests that samples with uniform and complete surface coverage of the substrate do not work well. This can be explained by the fact that excess charge, once formed on the sample surface, must travel long lateral distances before they can be conducted away by the underlying conductive substrate. Rather than strive for homogeneous films, it is useful to prepare samples where the sample of interest is composed of particles that are separated by some amount of bare substrate. This ensures that excess electrical charges can be quickly conducted away. One particularly successful method for non-soluble chemicals is to disperse the compound into a solvent and to deposit only the finest particles onto the substrate. This method can be facilitated by sonication or manual grinding with a mortar and pestle.

Depending on the sample at hand, various sample preparation methods can be used. Pure aerosol particles can be generated and deposited onto a silicon wafer to create relatively flat samples. In this method, several mg of compound is put into a glass tube, which is heated while an inert gas such as nitrogen or argon is flowed through. The silicon substrate is held stationary at the outlet of this gas. The exact temperature and gas flow rate required for optimal aerosol deposition depends highly on the chemical species being deposited.

For samples that do not adhere to the silicon substrate, embedding the material in an indium matrix can offer a solution. Conductive double-sided carbon adhesive sheets, used traditionally in the SEM community, can also work for certain applications.

2.4 Vacuum-Ultraviolet Laser Desorption Postionization

2.4.1 Experimental Design and Data Collection

To complement the high spatial resolution capabilities of VUV-SNMS, a laser postionization imaging method has been developed. To accomplish this, a UV Nd:YLF desorption laser (349 nm, Spectra Physics Explorer) has been coupled to the ToF.SIMS V instrument (Figure 2.13).

To compensate for the divergence of the laser desorption probe, a configuration was adopted wherein the laser output is first dispersed with a diverging lens before refocusing. All optical components in this configuration are outside of the vacuum chamber. Since the distance from the outer part of the flange to the central sample analysis region is ~220.4 mm, the last focusing lens has a long focal length and yields a spot size of ~30 μm at the sample surface. With this spot size, chemical imaging is possible by rastering the sample stage, and chemical analysis is facilitated by sampling fresh areas of sample via sample scanning. Due to the

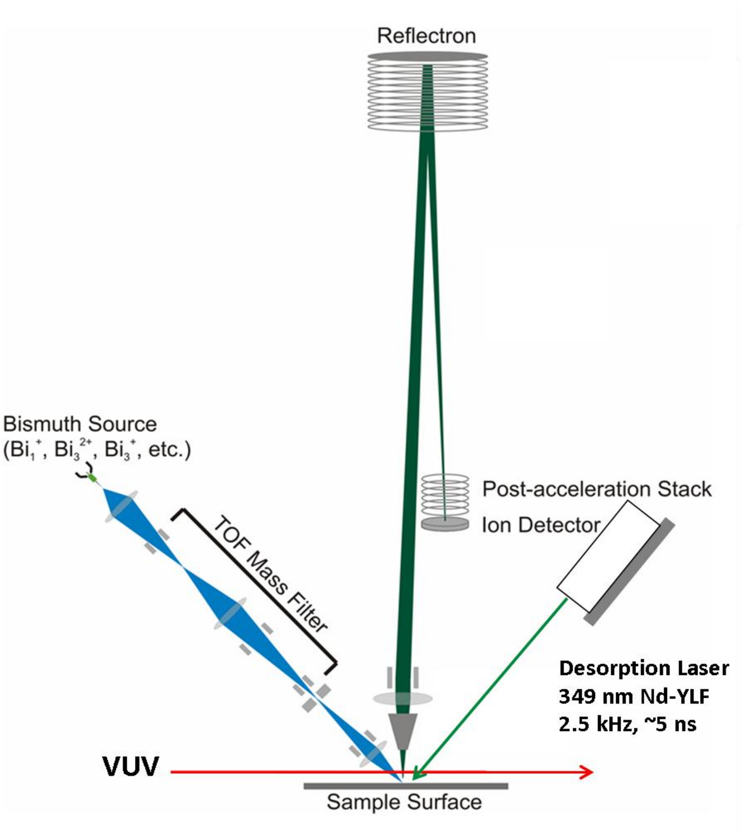

Figure 2.13: Schematic diagram of the experimental setup capable of VUV-secondary ion mass spectrometry, VUV-secondary neutral mass spectrometry and VUV-laser desorption postionization analysis.

small laser spot size, the laser power required to obtain ablative conditions is much lower than the first configuration. For most samples examined, attenuation of the laser output with a neutral density filter (ND in Figure 2.14) is necessary to minimize sample damage, even with the laser operating at the lowest power setting.

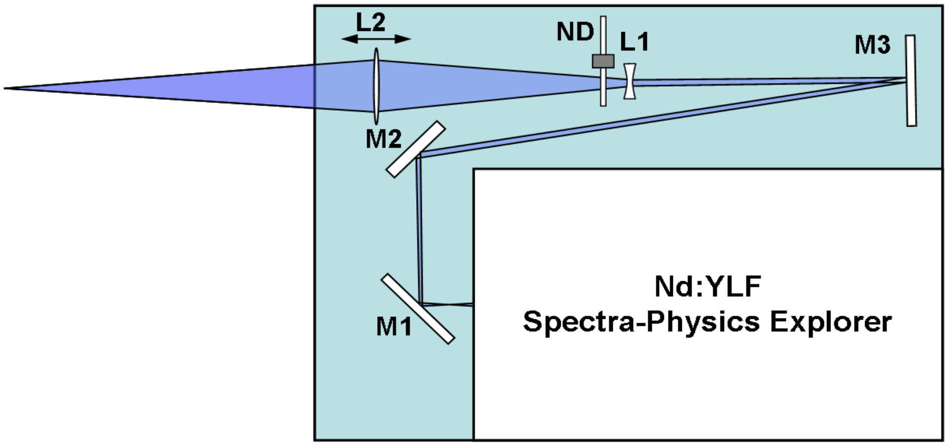

Figure 2.14: Schematic of the laser configuration yielding a 30 µm spot size at the sample. Three planar mirrors (M1, M2, and M3) are used to increase the path length of the laser. The first lens (L1) diverges the beam, and a neutral density filter (ND) is used to attenuate the laser power. The last lens (L2) focuses the laser beam onto the sample.

To minimize sample damage, it is possible to either raster the sample in discrete steps or to scan the sample in the lateral directions at a constant speed. With the former data acquisition method, it is possible to collect mass spectral images. The latter is most appropriate for performing chemical analysis of samples of limited quantities.

The laser desorption probe has several advantages over the ion desorption probe. For one, the laser deposits much less energy into the neutral molecules leaving the surface;[1] thus the molecular fragmentation induced during the photoionization step is reduced significantly. The desorption mechanism can be controlled by adjusting the laser peak power, from more ablative conditions[1] to more gentle, thermally desorbing conditions (see Chapter 6). Both conditions can result in simpler mass spectra compared to VUV-SNMS and in the detection of higher molecular weight components (see Chapter 6).

Due to the drastic improvement in the quality of mass spectra and the capability for chemical imaging with the laser probe, it is desirable to reduce the minimum spot size even further. Future plans for improving the spatial resolution of the laser probe will permit VUV-LDPI to be applied to a broader range of samples for chemical imaging and will require the final focusing lens to be placed closer to the sample surface, in the vacuum chamber.

2.4.2 Sample Preparation for VUV-LDPI

Since VUV-LDPI, like VUV-SNMS, relies on the synchrotron light to ionize desorbed molecules relatively close to the surface, sample flatness is very valuable; however, since the number of molecules leaving the surface upon laser desorption is considerably higher, the VUV light does not have to pass as close over the sample as in VUV-SNMS. This relaxes the constraint on how flat a sample must be. Furthermore, due to the fact that no charged species are being deposited onto the surface (*i.e.* no primary ion beams), organic species can be deposited in thicker layers than is possible for VUV-SNMS analysis.

Another characteristic that is desirable for VUV-LDPI samples is homogeneity. Spot to spot variations in sample thickness can lead to variations in the prompt ion background and can also significantly change the desorption mechanism. As a result, for chemical analysis, it is desirable to have topographically flat samples with relatively uniform thickness. For simple chemical samples, uniformity across a surface can be facilitated by ensuring that the underlying silicon substrates are clean and dust free. Dust can be effectively removed by cleaning polished silicon wafers with lens paper. Insoluble analyte materials (*e.g.* melanin or lignin) may be broken into smaller pieces by sonication or mechanical grinding. For compounds that do not adhere to silicon, it may be possible to mount them onto sticky carbon SEM tabs or double-sided silver tape. In all cases, the use of high-purity solvents is preferred.

2.5 Multimodal Imaging and Analysis

Postionization methods such as VUV-SNMS and VUV-LDPI generally result in direct ionization and the formation of M^+ cations. While VUV-LDPI and VUV-SNMS appear to be much better at preserving chemical information than SIMS for certain systems including lignin, the postionization methods do not yet represent a universal imaging method. Chemical species that are unstable as M^+ ions may be stable as protonated species or salt adducts, which are commonly observed in SIMS and MALDI. This can explain why SIMS works better than postionization methods for certain molecules, such as diether archaeal lipids,[2] as is illustrated by Figure 2.15. In a SIMS analysis of archaeal lipids, taken in the course of this work, the parent molecule of archaeal diether lipids is observed as protonated or sodiated (and sometimes potassiated or lithiated) adducts, whereas the parent ion is completely absent in the corresponding VUV-LDPI mass spectra. Thus, postionization techniques and techniques with coupled desorption and ionization are inherently complementary techniques.

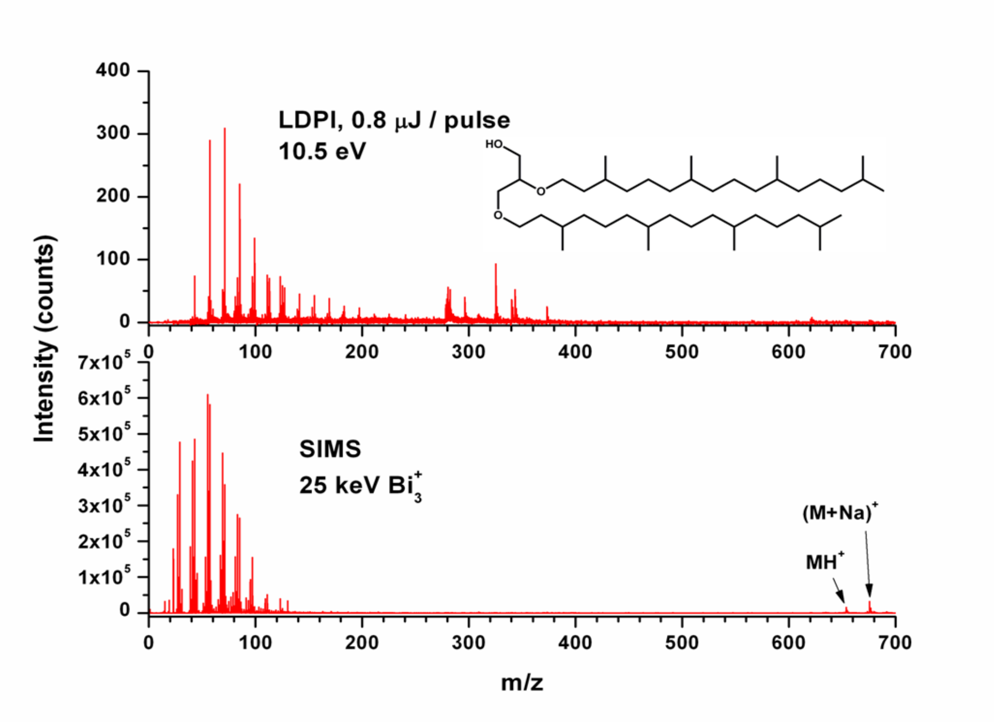

Figure 2.15: VUV-LDPI (top) and SIMS (bottom) mass spectra of archaeol (1,2-di-O-phytanyl-*sn*-glycerol; the parent molecular structure, M, is shown in black). Despite low mass fragmentation in both cases, the protonated parent (MH^+) and sodiated parent $(M+Na)^+$ are visible using positive SIMS, but M^+ is absent in the VUV-LDPI mass spectrum.

While they are powerful tools in themselves, SIMS, VUV-SNMS and VUV-LDPI are best used in combination with other imaging and/or analytical techniques. Non-destructive methods such as IR microscopy and fluorescence microscopy are very useful for quickly identifying areas of potential interest within a given sample. Fiducial markers within the sample can then be used to image the same sample area in the imaging apparatus via SIMS, VUV-SNMS or VUV-LDPI. This concept is illustrated in Figure 2.16, where an optical microscope allowed for rapid identification of an area of interest over a bacterium within an SM1 archaeal biofilm.[3-6] This area was subsequently imaged using SIMS in this work.

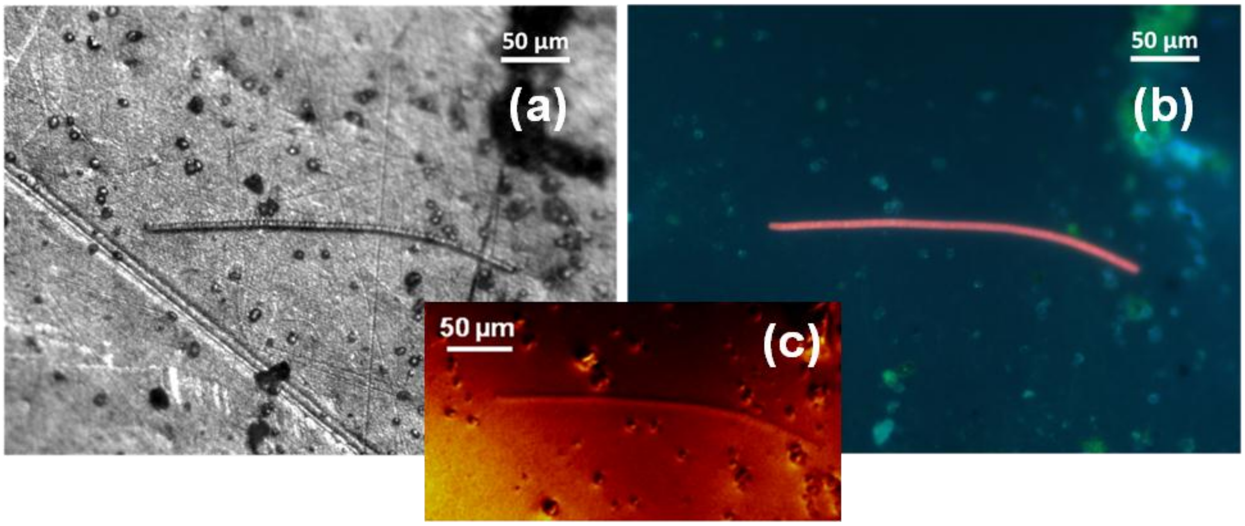

Figure 2.16: (a) Brightfield image, (b) autofluorescence image, and (c) total positive ion SIMS image (c) of a bacterium within the SM1 archaeal biofilm. The bacterium appears as a red line in (b). The complementary optical images and in-sample fiducial markings facilitated the location of this area of interest in the chemical imaging apparatus.

Even with a simplified mass spectrum and information of a molecule's appearance energy, it is difficult to unambiguously assign a mass feature from an unknown. To facilitate mass spectral assignments, it would be useful to implement MS/MS capabilities in the VUV-SNMS/LDPI instrument. Since this capability is not currently available on the imaging apparatus, complementary mass spectral analysis on other instruments such as liquid chromatography (LC)/MS/MS or electrospray (ESI)-MS/MS can provide valuable data to confirm mass spectral assignments. The utility of developing MS/MS capabilities on the imaging mass spectrometer are discussed further in Chapter 6.

References

(1) Kostko, O.; Takahashi, L. K.; Ahmed, M. *Chemistry – An Asian Journal* **2011**, *6*, 3066.

(2) Thiel, V.; Heim, C.; Arp, G.; Hahmann, U.; Sjövall, P.; Lausmaa, J. *Geobiology* **2007**, *5*, 413.

(3) Henneberger, R.; Moissl, C.; Amann, T.; Rudolph, C.; Huber, R. *Appl. Environ. Microbiol.* **2006**, *72*, 192.

(4) Moissl, C.; Rudolph, C.; Huber, R. *Appl. Environ. Microbiol.* **2002**, *68*, 933.

(5) Rudolph, C.; Moissl, C.; Henneberger, R.; Huber, R. *FEMS Microbiology Ecology* **2004**, *50*, 1.

(6) Rudolph, C.; Wanner, G.; Huber, R. *Appl. Environ. Microbiol.* **2001**, *67*, 2336.

Chapter 3

SIMS and VUV-SNMS of Metals and Semiconductors and Their Internal Energies

Adapted with permission from Journal of Physical Chemistry A, 2009, 113 (16) pp 4035-4044.

A new mass spectrometry surface imaging method is presented in which ion-sputtered neutrals are postionized by wavelength-tunable vacuum-ultraviolet (VUV) light from a synchrotron source. Mass spectra and signal counts of the photoionized neutrals from GaAs (100) and Au are compared to those of the secondary ions. While clusters larger than dimers are more efficiently detected as secondary ions, certain species, such as As_2, Au and Au_2, are more efficiently detected through the neutral channel. Continuously tuning the photon wavelength allows photoionization efficiency (PIE) curves to be obtained for sputtered As_m (m=1,2) and Au_n (n=1-4). From the observed ionization thresholds, sputtered neutral As and Au show no clear evidence of electronic excitation, while neutral clusters have photoionization onsets shifted to lower energies by ~0.3 eV. These shifts are attributed to unresolved vibrational and rotational excitations. High-spatial resolution chemical imaging with synchrotron VUV postionization is demonstrated at two different photon energies using a copper TEM grid embedded in indium. The resulting images are used to illustrate the use of tunable VUV light for verifying mass peak assignments by exploiting the unique wavelength-dependent PIE of each sputtered neutral species. This capability is valuable for identifying compounds when imaging chemically complex systems with mass spectrometry-based techniques.

3.1 Introduction

There is enormous interest in understanding how the surfaces of nanoparticles – both inorganic and biological – influence their chemistry. The composition of nanometer-sized aerosol surfaces play critical roles in both the radiative balance and chemistry of the troposphere.[1] Surfaces are also critical determinants in the structure and dynamics at boundaries of different cellular structures.[2] Developing new microscopies to detect and identify molecules with high spatial resolution will clearly allow the study of more complex nano-scale chemistry. Here a technique to perform chemical imaging on surfaces using a novel mass spectrometry method is presented, wherein ion-sputtered neutrals are photoionized with high fluxes of tunable-wavelength synchrotron VUV light. Traditional electron and optical based imaging techniques generally lack sufficient chemical specificity at the molecular level for understanding the complex chemical systems prevalent in nature. Mass spectrometric imaging using an ion nanoprobe offers a solution to this long-standing problem in the imaging community, allowing the localization of specific chemical species on length scales of 100 nm or less. Until now, either the secondary ions (secondary ion mass spectrometry or SIMS), or laser postionized ion-sputtered neutral species (secondary neutral mass spectrometry or SNMS) have been detected, the latter often involving harsh multiphoton ionization conditions. Here the gentle, single photon ionization imaging of ion-nanoprobe-sputtered neutrals by VUV light is described.

Ion sputtering has found extensive application in the physical modification of material surfaces,[3] and it is the key process behind SIMS and SNMS. As such, ion sputtering has been the subject of many experiments and extensive molecular dynamics simulations,[4] but much of the detailed physics of the sputtering process is still not well understood. Upon surface bombardment with keV atomic or cluster ion projectiles, a series of rapid collision cascades[5] is generated within the solid, resulting in the localized ejection of surface species in neutral, positive and negative charge states. In this complex process, the translational energy from the incident primary ions can be transferred to the ejected atoms and molecules in the form of kinetic, vibrational, rotational, or electronic energy.

To image with SIMS and SNMS, an ion source is rastered across the sample, and the mass spectrum collected from each spatial pixel is used to reconstruct a complete chemical image of the analyzed surface. In SIMS, mass spectra of the sputtered secondary *ions* are analyzed, and in SNMS, the sputtered *neutrals* are postionized before extraction into a mass spectrometer. Both imaging techniques have long been utilized in the semiconductor industry, where the localized chemical distributions of various dopants can be mapped as a function of lateral position and depth within semiconducting samples.[6] More recently, SIMS has also found applications in imaging organic and biological samples. Among these advancements, Kraft *et al.* used SIMS to image lipid domains within prepared lipid membranes down to ~100 nm,[7] Colliver *et al.* used SIMS imaging to study the organism paramecium,[8] and Lechene *et al.* successfully used SIMS with multi-isotope imaging to map the fate of fixed nitrogen in host cells.[9] Furthermore, Fletcher *et al.* performed depth profiling experiments to generate three-dimensional chemical images of whole frog eggs[10] and Ostowski *et al.* imaged the heterogeneous distribution of lipids in cell membranes of mating Tetrahymena (a protozoan).[11]

Despite these advancements, certain aspects of SIMS imaging remain problematic. One issue is that secondary ion signal intensities can vary dramatically across a single sample due to the sensitivity of ion sputter yields to the local chemical environment ("matrix effects").[12] Yields are higher and less subject to local chemical variations across a sample for secondary neutrals than secondary ions, so SNMS has been pursued in several groups. SNMS imaging with laser postionization has been performed in the past with spatial resolutions on the order of 100 nm.[13,14] Because few tunable lasers exist in the region above 7 eV where the ionization energies of most organic molecules occur, postionization experiments often employ nanosecond, picosecond and femtosecond lasers in multiphoton ionization schemes to probe both inorganic and organic samples.[15-17] Extra internal energy deposited into sputtered molecules during such multiple photon ionization processes, however, often results in molecular fragmentation.[18] The complications introduced by fragmentation are amplified when analyzing heterogeneous samples such as biological cells, where thousands of chemical compounds are present. It is therefore necessary to study the energetics of sputtered neutral species and to devise methods to aid in the identification of mass spectral features.

One method of minimizing fragmentation is to softly ionize sputtered neutral species using threshold VUV single photon ionization.[19,20] Recently, tunable synchrotron VUV light was utilized to photoionize laser desorbed organic molecules at different photon energies and study molecular fragmentation pathways.[21] Peterson *et al.* found that SNMS with different postionizing VUV laser wavelengths could be used to selectively analyze classes of chemical components (organic and inorganic) within atmospheric aerosol particles.[22] Veryovkin *et al.* used VUV light from the Advanced Photon Source free electron laser to postionize inorganic species sputtered by noble gas primary ions,[23] but the experiments suffered from a very low repetition rate of 6 Hz and limited wavelength tunability.

In this chapter, tunable synchrotron VUV photoionization of ion-sputtered neutrals is presented as a method for chemically selective imaging of multi-component samples. The features and performance of this method are compared to normal SIMS imaging. With the wavelength tunability of the synchrotron light, threshold ionization is made possible, which can minimize molecular fragmentation compared to typical multi-photon ionization schemes used in previous postionization studies. Unlike many laser postionzation techniques, data acquisition rates are not limited by the duty cycle of a laser, since the synchrotron's light beam is quasi-continuous. This fact allows for routine operation at 10 kHz, which is limited only by the repetition rate of the ion gun and the flight times of the postionized neutrals. Furthermore, since each chemical species has a characteristic photoionization efficiency wavelength dependence, tuning the synchrotron photon energy can provide additional information that can be used to identify chemical compounds with less ambiguity. This enhanced selectivity and the reduced imaging artifacts arising from SIMS "matrix effects" are essential for extracting useful information from heterogeneous chemical systems.

3.2 Experimental Methods

A modified commercial secondary ion mass spectrometer (TOF.SIMS 5, ION-TOF Inc.), operating under ultrahigh vacuum conditions (10^{-9} mbar, 1 mbar = 0.1 kPa), is coupled to a VUV light source on the Chemical Dynamics Beamline at the Advanced Light Source, Lawrence Berkeley National Laboratory (Figure 3.1). The setup utilizes a bismuth liquid metal ion gun (LMIG), mounted at 45 degrees with respect to the sample surface normal, to deliver pulses of bismuth cluster primary ions (Bi^+, Bi_3^+, or Bi_3^{2+}) at a repetition rate of around 10 kHz. All analyses are performed using beams of a single type of bismuth cluster ion at any given time, which is selected via a time-of-flight filter within the ion gun.

Samples are held at ground potential, 1.5 mm away from the analyzer extraction cone. About 1 µs before each primary ion pulse impinges on the sample surface, the extraction cone is pulsed from 0 V to -2000 V and is held at -2000 V for 10 µs (see Figure 3.1, top left for timing scheme). The positively charged secondary ions and postionized neutrals are extracted into a reflectron-type time-of-flight (ToF) mass spectrometer with a two-meter long path length and are detected and recorded through TOF.SIMS 5 computer software.

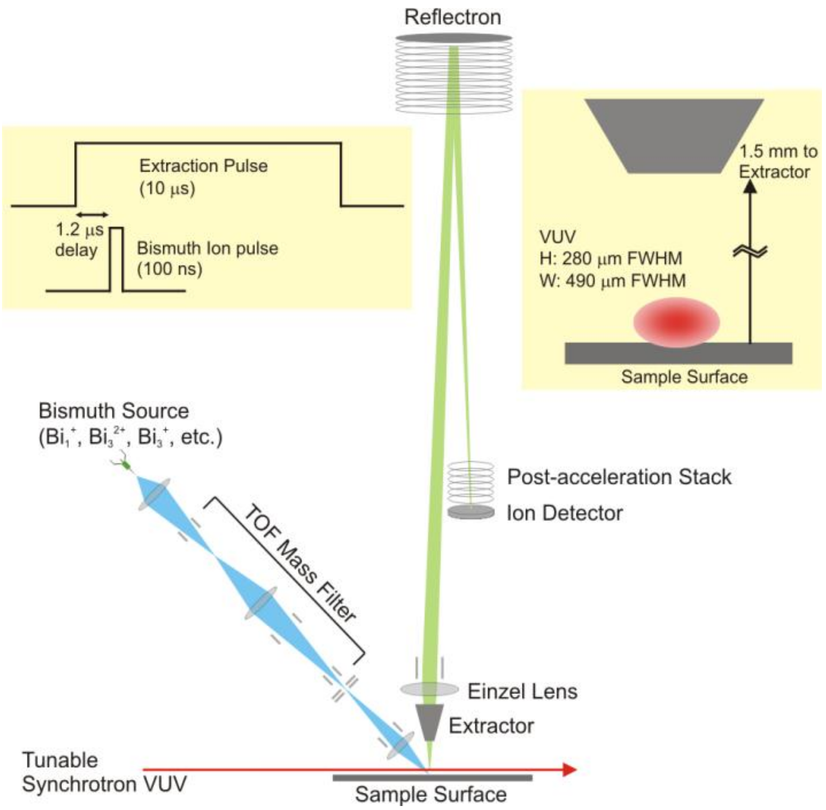

Figure 3.1: Schematic of the TOF.SIMS V setup coupled to the synchrotron VUV beamline. The bismuth primary ion beam is represented in blue, the VUV beam is indicated in red, and the path of the extracted postionized neutrals is shown in green. An outline of the extraction pulse timing with respect to the LMIG pulse (upper left) and an expanded view of the light with respect to the sample stage (upper right) are also shown.

The optimal analyzer conditions for the detection of secondary ions and postionized neutrals are different due to the different extraction voltages that the two ion populations experience in the extraction scheme described above. Secondary ions are extracted immediately upon their formation at the sample surface and are therefore accelerated through the full -2000 V between the sample surface and the extractor cone. Postionized neutrals, on the other hand, accelerate through a range of extraction voltages depending on the height above the surface at which they are ionized. This spread in extraction potential results in a broader range of paths through the analyzer for the postionized neutrals than for the secondary ions, which prompted the removal and enlargement of several apertures along the flight path of the original TOF.SIMS 5 instrument. Since the postionized neutrals experience lowered extraction potentials due to their formation a finite distance away from the sample surface, they possess correspondingly lowered kinetic energies as they travel through the TOF analyzer. This results in lower optimal voltages for the Einzel lens for post-ion detection (4600 V compared to 4840 V for optimized SIMS; see Figure 3.1 for an overview of analyzer components). The voltage applied to the last reflector plate within the analyzer is also lower for optimized postionization conditions (-20 V compared to +20 V for optimized SIMS). Optimized postionization settings are used for all datasets utilized in the presented postionization spectra and PIE curves. Optimized SIMS settings are only used for datasets used to make direct comparisons between postionization and SIMS.

The mass spectra and PIE curves in this chapter are measured with the LMIG in the highest-current mode at 25 keV (doubly charged species are emitted at 50 keV), using a pulsed ion beam of Bi^+, Bi_3^+ or Bi_3^{2+} (100 ns pulse length, corresponding to approximately 9.1 pA, 2.5 pA, and 2.2 pA current, respectively, at 10 kHz) with a ~5 μm diameter spot size. The images presented in this chapter are acquired using two high-spatial resolution settings of the LMIG, with spot sizes of ~100 nm (1000 ns pulse widths) and ~250 nm (800 ns pulse widths). Long LMIG pulse widths are used for imaging to minimize data collection time, although the use of shorter pulse widths is possible.

The beamline, described in detail elsewhere,[24] uses an undulator to generate wavelength-tunable, quasi-continuous (500 MHz) VUV light in the region from 7.5 eV to 25 eV. The spectral resolution of the light used in this work is determined to be ~0.35 eV by measuring the spectral FWHM of the autoionizing resonance of ion-sputtered silicon atoms. The light from the undulator is reflected by three mirrors before passing through the TOF.SIMS 5. The first two mirrors focus the VUV light to the center of a differentially pumped gas filter to remove higher energy harmonic radiation. Argon is used in the gas filter for the present experiments, filtering out photons with energies above the Ar ionization threshold of 15.76 eV. After the gas filter, the light is again reflected and focused by a gold coated toroidal mirror, which delivers 10^{15}-10^{16} photons/s (at 400 mA synchrotron current) with a spot size of approximately 280 μm (vertical) x 490 μm (horizontal) to the terminal where the TOF.SIMS 5 instrument is situated. This last mirror is controlled by two motorized stages, allowing the light position to be finely adjusted in the ion extraction area.

Photon flux curves as a function of energy are determined using a NIST-calibrated photodiode (SXUV-100, International Radiation Detectors) and a picoammeter (486 picoammeter, Keithley) attached to the light exit port. All energy spectra are normalized to the measured flux curve. Corrections are also made to the photon energy scans presented in this chapter to account for the exponential decay of the overall photon flux, which decays with the lifetime of the electrons in the synchrotron storage ring, although the overall effect is minimal for the short time scans reported here. Corrections are not applied for height changes induced in the analyzed sample area by ion-sputtering.

Au (Alfa Aesar, 0.1 mm thick, 99.95%) and standard GaAs (100) samples are clamped onto the edge of an aluminum top-mount sample holder closest to the incoming photon beam, allowing the synchrotron light to pass as close to the sample as possible. A VUV-induced current can always be measured from the sample stage, indicating that a part of the near-Gaussian “tail” of the photon beam spatial profile impinges on the sample. This grazing light configuration is used for optimal overlap of the photon beam with the sputtered neutral plume. For both samples, 500 μm x 500 μm regions are scanned six times with a DC beam of bismuth ions (current ~15 nA, all cluster-ion species of bismuth) prior to analysis to ensure surface cleanliness and spectral reproducibility, although only the central 100 μm x 100 μm area is analyzed for the spectra and PIE curves presented here. This smaller area is analyzed with 500 scans using a 16 x 16 pixel raster for each dataset. Sample analysis is conducted at room temperature (~300 K). Three datasets are taken for each postionization data point, each measured under the optimal analyzer conditions for postionization: one measuring the signal directly from the ion gun (SIMS background signal), one measuring the synchrotron-ionized background signal, and one measuring the signal arising from the LMIG and the synchrotron together. SIMS background and synchrotron background scans are subtracted from the signal arising from the LMIG and synchrotron together to yield the postionization spectra.

To demonstrate high-spatial resolution imaging with VUV postionization, a copper TEM grid embedded in indium is imaged. The sample is prepared on a stainless steel substrate, onto which a piece of flattened indium wire is placed. The copper grid is put on top of the flattened indium and is subsequently flattened between another stainless steel substrate with pliers. The top stainless steel piece is then removed to reveal the copper grid pushed into the indium metal. As with the GaAs and Au samples, the grid sample is mounted on the edge of the rectangular top-mount sample holder closest to the incoming light and is subjected to six DC scans from the LMIG prior to analysis.

3.3 Results and Discussion

3.3.1 TOF Analyzer Transmission

The analyzer transmission efficiency is estimated by leaking 1.0 x 10^{-8} mbar of Xe into the main chamber with a base pressure of 4.1 x 10^{-9} mbar. The gas is ionized with 14 eV photons. At 14 eV photon energy, the expected number of Xe counts per second, S, is given by:

$$S \approx \sigma F N \alpha \tag{3.1}$$

where σ is the photoionization cross section of Xe at 14 eV, F is the photon flux at 14 eV, N is the number of Xe atoms in the ionization volume (assumed to be constant) and α is the fraction of total ions formed that are extracted by the analyzer pulse. At 14 eV, Xe has an ionization cross section of 50 Mb (1 Mb = 1 x 10^{-18} cm^2)[25] and the average photon flux is measured to be 1.8 x 10^{18} photons/($cm^2 \cdot s$). Spectra are taken using 10 µs analyzer extraction pulses at 10 kHz, although ionization of Xe occurs continuously. Assuming that the equivalent of 10 µs of ionized Xe resides in the extracted volume at the time of the extraction pulse, α is 0.2 (all ions formed in 10 µs before the pulse + all ions formed during the 10 µs extraction pulse are extracted). If the sampled ionization volume is approximated by the dimensions of the light beam cross section and the 1 mm diameter opening of the analyzer extractor cone, then at the given pressure, about 1.97 x 10^4 Xe atoms are present in the sampled ionization volume, yielding S = 3.59 x 10^5 counts per second. Experimental measurements result in 3.00 x 10^4 counts per second for all isotopes of Xe, corresponding to a detection efficiency of ~8%.

With the calculated transmission efficiency through the analyzer, measured signal intensities, LMIG current, photon flux and ionization cross sections, approximate neutral sputter yields can be deduced. For the discussion here, Zn is considered because its absolute photoionization cross section is known.[26] If 8% transmission efficiency is assumed for neutrals desorbed from a Zn sample, then at a photon energy of 11.9 eV the number of Zn atoms that are sputtered per second, $\tilde{N}$, can be calculated using a formula very similar to Eq. 3.1:

$$\tilde{N} = \frac{Z}{0.08\tilde{\sigma}\tilde{F}\tilde{\tau}}, \tag{3.2}$$

where 0.08 is the detection efficiency, $\tilde{\sigma}$ is the photoionization cross section of Zn at 11.9 eV, $\tilde{F}$ is the photon flux at 11.9 eV, Z is the number of Zn postionization counts observed per second, and $\tilde{\tau}$ is the average time that each of the neutrals spend in the VUV beam path. At 11.9 eV, Zn has an approximate cross section of 150 Mb,[26] and the average photon flux is measured to be approximately 1.77 x 10^{18} photons/(cm^2*s). With the vertical extent of the light beam measured to be 280 µm and assuming an typical kinetic energy of 1 eV[27] for the sputtered Zn, $\tilde{\tau}$ is 0.16 µs. Experimental measurements obtain 1.21 x 10^4 Zn postionization counts per second for all isotopes of Zn upon bombardment with Bi^+ primary ions. Inputting these values into Equation 2 yields 3.6 x 10^9 sputtered neutral Zn atoms per second, which, with 9.1 pA of Bi^+ beam current, corresponds to an approximate neutral sputter yield of 62.7 Zn atoms per incident Bi^+ primary ion. This value is in good agreement with the prediction of 83.8 sputtered Zn per Bi^+ obtained using the semi-empirical Yamamura formula[28,29] for Bi^+ primary ions at 45 degree incidence. A similar analysis of Zn postionization signal resulting from Bi_3^+ bombardment gives a 8.5 times yield enhancement per incident ion compared to Bi^+. Although the change in the sputter yield in going from atomic to cluster primary ions depends on the specific projectile-sample combination,[30] the enhanced sputter yield with the use of cluster projectile ions is also generally observed for other systems.[30,31]

3.3.2 Synchrotron VUV Postionization and SIMS

Several sample substrates (Ag, Cu, Si, In, Ge, Pt and Zn) are analyzed with the present experimental arrangement, but only the results obtained for GaAs and Au are presented in detail here. GaAs and Au are chosen because both yield VUV postionization spectra with relatively high signal intensities for dimers and larger clusters. The observation of clusters is desirable because clusters, unlike atoms, can possess vibrational and rotational excitations. Furthermore, GaAs and Au are discussed because they yield neutral clusters (namely As_2, Au_2, and Au_4) that exhibit ionization thresholds well within our available photon range. This allows adequate baseline counts to be collected so that ionization thresholds can be obtained from the PIE curves (discussed later).

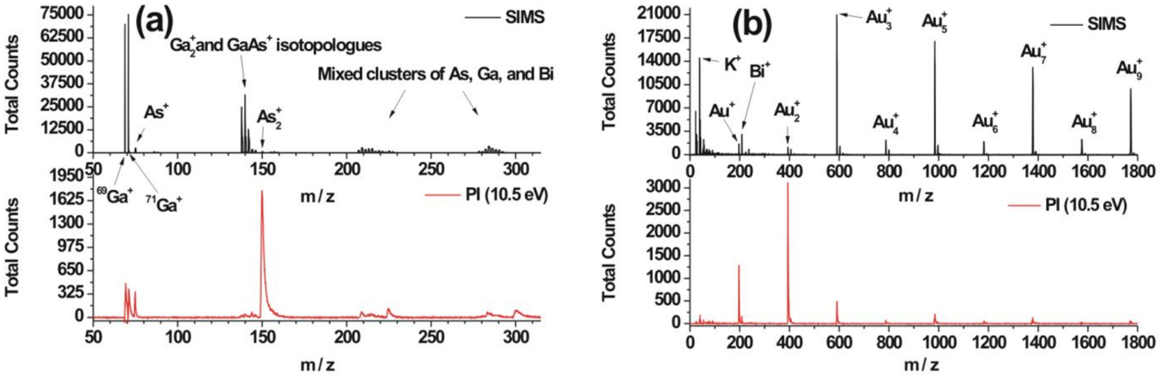

Figure 3.2: SIMS and postionization (PI) spectrum obtained over (a) GaAs and (b) Au using a Bi_3^+ primary ion beam. The postionization spectra for both surfaces are collected using 10.5 eV photons, the photon energy with maximal signal intensity for As_2 and Au_2. SIMS and postionization spectra presented here are taken under their respective optimal analyzer settings.

SIMS and neutral postionization mass spectra using 100 ns Bi_3^+ primary ion beams and 10.5 eV photons are collected from GaAs and Au and are compared in Figure 3.2. 10.5 eV is chosen since it yields the highest Au_2 and As_2 postionization signals and because previous laser postionization studies over GaAs have been done at 10.5 eV.[19] For a meaningful comparison of the spectra in Figure 3.2, the SIMS and postionization spectra are collected under the optimum analyzer conditions for each. The corresponding signal counts for the datasets used in Figure 3.2 are summarized in Table 3.1. From the table, it is seen that each postionization peak has different SIMS and synchrotron background levels. For the particular case of Au_2 and 10.5 eV ionizing photons, the postionization signal intensity dominates the background signals from both sources and is reproducible to within 1%.

Atom or Cluster	Optimized for SIMS	Optimized for Postionization			
	SIMS	Synchrotron Background	SIMS Background	Synchrotron + LMIG	Postionization[a]
^{69}Ga	1.27×10^5	360	6.52×10^4	7.24×10^4	6.84×10^3
As	2.35×10^4	260	39	4.63×10^3	4.33×10^3
As_2	5.62×10^3	610	79	5.09×10^4	5.02×10^4
Au	8.09×10^3	160	570	1.14×10^4	1.06×10^4
Au_2	5.66×10^3	75	170	3.47×10^4	3.45×10^4
Au_3	8.36×10^4	19	3.58×10^3	7.62×10^3	4.03×10^3
Au_4	1.09×10^4	14	42	629	570

Table 3.1: Counts for optimized SIMS compared to the counts for the synchrotron background, SIMS background, synchrotron + LMIG signals, and postionization signals for select atoms and clusters at 10.5 eV (corresponding mass spectra are shown in Figure 3.2). Signals are collected over a 100 µm x 100 µm area with a 16 x 16 pixel raster over 500 scans (~13 - 19 seconds; longer times used for the large Au clusters).

[a] Postionization signal counts are the final result after subtraction of “SIMS Background” (SIMS under optimal postionization analyzer conditions) and “Synchrotron Background” from the signals resulting from the “Synchrotron + LMIG” together.

From the comparison of SIMS and postionization spectra in Figure 3.2, it is clear that SIMS has higher signal intensities for larger clusters, although the signal intensities of SIMS and postionization for Au and As are comparable. The integrated postionization signal intensity for Au_2 and As_2 at 10.5 eV, however, are factors of 6 and 9 higher than their respective SIMS peaks. The prominence of these neutral dimers compared to either neutral Ga or As is likely due to a combination of a large sputter yield and ionization probability and illustrates the complementary nature of the SIMS and VUV postionization techniques. It should be noted that the observed relative intensities of the postionized neutral clusters in Figure 3.2 do not reflect the absolute population distribution within the neutral plume. Unlike most laser postionization experiments, the relative intensities observed with the current experiments are strong functions of the species-specific ionization cross sections because the synchrotron does not saturate the photoionization process.

In the SIMS spectra for the Au surface (Figure 3.2b, top), there is a cluster of peaks at low m/z resulting from surface contaminants. Most notable is the large peak from potassium at m/z ~39. Although potassium is presumably a small component on the Au surface, the K^+ peak intensity is comparable to those of the strongest gold cluster peaks due to the ease with which it forms secondary ions. These low m/z trace contaminants are not present in the postionization spectra. In fact, the small peaks at low m/z in the postionization spectra (Figure 3.2b, bottom) are purely a result of incomplete background subtraction resulting from the scan-to-scan variation of the SIMS intensity. This conclusion is supported by the narrow widths of the low m/z peaks (postionization peak widths are discussed below).

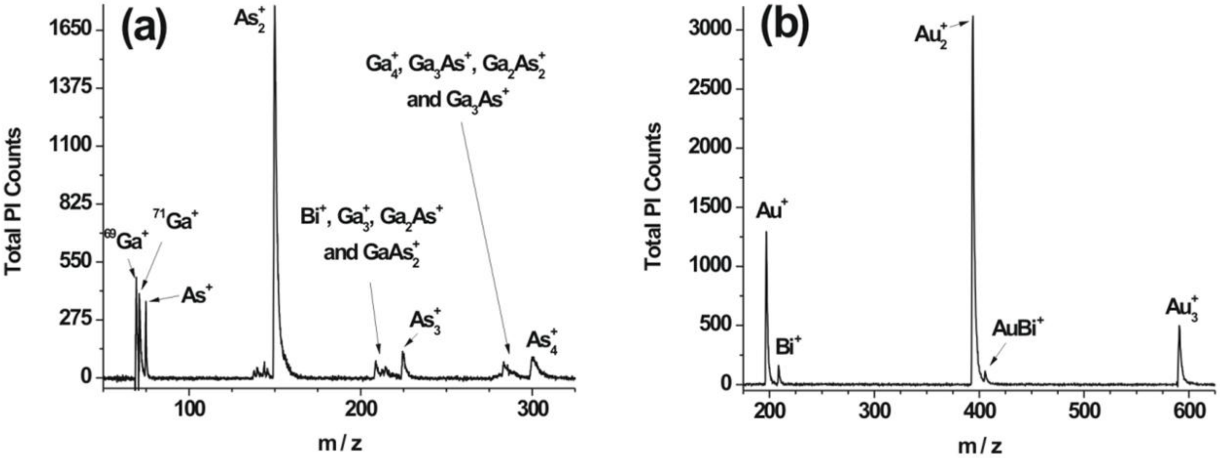

Figure 3.3: Expanded view of the postionization spectra shown in Figure 3.2 over (a) GaAs (100) and (b) Au obtained with 10.5 eV photons and 100 ns pulses of Bi_3^+ primary ions.

Figure 3.3 shows an expanded view of the postionization spectra of Figure 3.2. The postionization peaks exhibit a sharp Gaussian-like leading edge and a broader, Lorentzian-like tail toward later times. As_2, (m/z = 149.84) has a postionization peak with $m/\Delta m \approx 100$, which under the conditions used in this experiment is comparable to the $m/\Delta m \approx 200$ for the corresponding optimized SIMS As_2 peak. SIMS peak widths scale with LMIG pulse length, so SIMS mass resolution can be improved by shortening the LMIG pulse length. The postionization peakwidths, on the other hand, do not scale closely with LMIG pulse width for short pulses below 100 ns, so mass resolution cannot be improved using the same method. This behavior may be attributed to the quasi-continuous photoionization and the finite vertical dimension of the photon beam. Because of these two factors, neutrals are ionized (and extracted) at different times and can experience a range of extraction voltages. While the reflectron compensates somewhat for the second effect, it cannot compensate for the spread in the "time-of-birth" of the post-ions. Despite this, it is possible to narrow postionization peaks by a factor of ~3 by delaying the analyzer extraction pulse with respect to the primary ion pulse (data not shown). For the data presented in this chapter, however, long LMIG pulse lengths of 100 ns are used so that SIMS and postionization peaks have comparable width, making postionization signals easier to identify.

So far, SIMS and SNMS are shown to be complementary techniques that can yield different information for the analyzed surface. While SIMS is typically more sensitive than synchrotron VUV postionization for the larger clusters, synchrotron VUV postionization yields comparable signals for smaller species like Au, Au_2, As, and As_2 and is not subject to the non-representative high peak intensities of low m/z trace contaminants. Observed postionization peaks are generally broader than SIMS peaks, but can be narrowed by delaying the application of the extraction voltage. Not yet discussed are the additional advantages of synchrotron VUV postionization compared to SIMS and conventional laser postionization due to the unique wavelength tunability of the synchrotron. One such advantage is the capability to study the energetics of sputtered neutrals, as is discussed in the following section.

3.3.3 Photoionization Efficiency Curves

To investigate the internal energies of sputtered neutral species, PIE curves are obtained for sputtered neutrals from GaAs (100) and Au by varying the photon energy in 0.15 eV steps. Wucher *et al.*[32] previously collected PIE curves using single photon laser ionization to illustrate the high internal temperatures of ion-sputtered indium clusters compared to cold clusters from a supersonic nozzle expansion. In the present experiment, sets of three PIE scans for each substrate are taken over the same area in succession with each of the primary ion beams (Bi^+, Bi_3^+ and Bi_3^{2+}) to determine whether neutrals sputtered by different primary ions have significantly different internal energies. For scans from GaAs, the photon energy range from 7.5 eV to 14 eV is scanned; for scans from gold, the photon energy is varied from 7.5 eV to 12 eV.

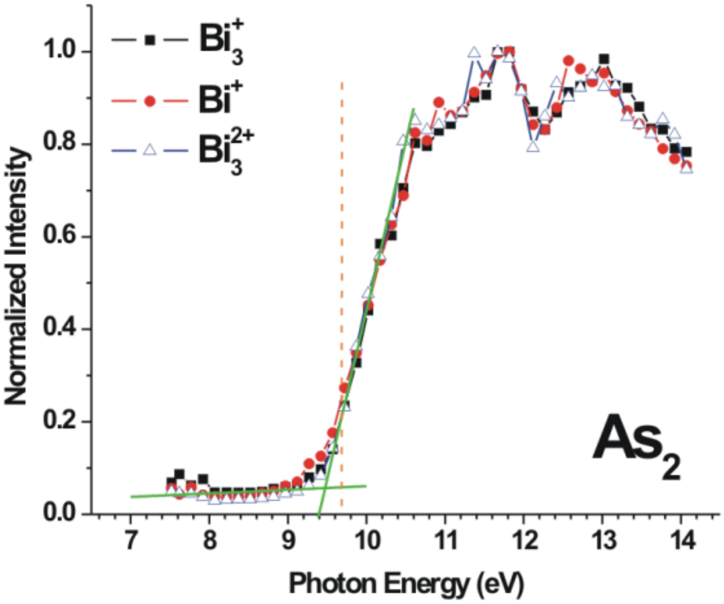

Figure 3.4: Photoionization efficiency curves for As_2 resulting from the three primary ion beams indicated in the graph legend. The literature experimental adiabatic ionization energy from Table 3.2 is indicated by the vertical orange dashed line, and the extrapolation lines used to determine the ionization threshold energy are indicated in green.

PIE curves can provide information about the internal excitation of the sputtered neutral species from the surface. According to the Franck-Condon principle, the most probable electronic and vibrational transition will be that with the least geometry change (vertical transitions). If the neutrals contain internal energy, then there is a distribution of initial state energies and geometries which may increase the energy range of the allowed vertical transitions. Thus, internal energy may broaden and change the shape of the PIE curve ionization onset[33] in addition to lowering the energy needed for ionization to occur. Figure 3.4 compares the As_2 PIE curves resulting from Bi_3^+, Bi^+ and Bi_3^{2+} primary ion bombardment. As_2 has the highest maximum postionization intensity and signal-to-noise of all species analyzed from GaAs, possibly due to the particular stability of the neutral As_2 molecule, which is characteristic of group 5A diatomics. No distinctive differences are visible among the three PIE curves obtained for As_2 with the different primary ion beams, nor are any significant differences seen for other sputtered species from the GaAs and Au surfaces; hence the set of three PIE scans is only shown for As_2.

As_m	This work	Literature ionization energy
m = 1	9.62±0.18	9.79[a]
m = 2	9.42±0.18	9.69[b,c]

Table 3.2: As_m (m = 1, 2) observed ionization thresholds compared to previous experimental ionization energies. All energies are in eV.

[a]Evaluated arc spectrum from Ref.[34]; [b]Photoionization from Ref. [35]; [c]Adiabatic ionization energy

The ionization onset slope and low-photon energy baseline of the As_2 PIE curves are linearly extrapolated (Figure 3.4, green lines), and the energy at the intersection of the lines is taken to be the threshold ionization energy. Small features in the low energy regions (at and below approximately 7.9 eV) of the PIEs likely arise from the residual harmonic radiation of the undulator passing through the argon gas filter. These data points are therefore excluded from the fits for the extrapolation lines used for the baselines of the PIE curves. This linear extrapolation method yields the same As_2 ionization threshold energy (9.42 ±0.18 eV) for each of the three primary ion beams. This value is compared to literature experimental and theoretical ionization energies in Table 3.2, where it can be seen that the observed ionization threshold lies 0.27 eV lower than the adiabatic ionization evaluated by Yoo *et al.*[35] This 0.27 eV difference is suggestive of vibrational excitation of the sputtered As_2. Since the lowest-lying As_2 electronically excited state lies nearly 1.8 eV above the ground electronic state[36] and this is not observed in the PIE curve, we conclude that electronic excitation for sputtered neutral As_2 is likely insignificant.

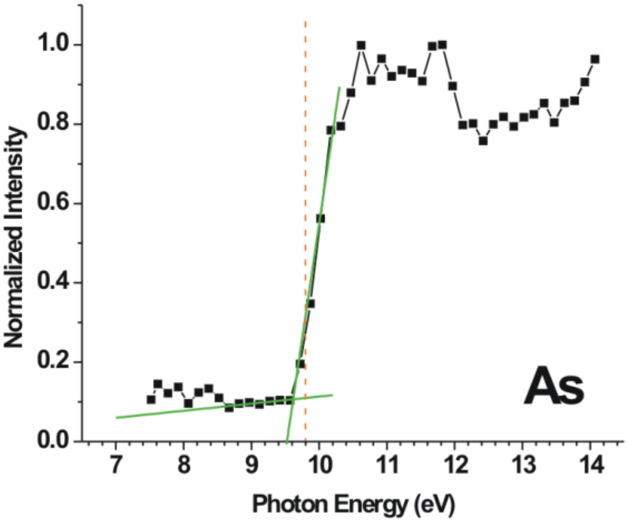

Figure 3.5: PIE curve for As from Bi_3^+ primary ion bombardment. The vertical orange dashed lines represent literature experimental adiabatic ionization energies taken from Table 3.2, and the green lines represent the extrapolation lines used to determine the ionization threshold.

Similar analysis of the PIE onset for As (Figure 3.5) yields an ionization onset of 9.62 ± 0.18 eV for all three incident primary ion beams. This value agrees with literature values for the As ionization energy[34] within experimental uncertainty. Since As atoms cannot undergo vibrational or rotational excitation, the only excitation possible is electronic; however, the lowest As excited electronic state lies 1.3 eV above the ground electronic state.[37] Since no features are observed in the PIE 1.3 eV below the ionization threshold, electronic excitation appears not to play a role in the sputtered neutral As.

As was noted in the previous section, all postionization mass peaks that are observed in this experiment, including that for As_2, have a characteristic shape and finite width, with a sharp Gaussian-like rising edge and a Lorentzian-like tail toward later arrival times (see Figure 3.3a, 3.3b). Due to the particularly strong signal levels for As_2, PIE curves can be reconstructed for both the rising edge and trailing tail portions of the As_2 mass peak resulting from Bi_3^+ bombardment; however, only minor differences (within the experimental resolution) are observed for the obtained ionization threshold values. Similar observations are made when a delay (up to 0.6 μs) is applied between the LMIG pulse and the analyzer extraction voltage. In these delayed extraction experiments, no differences in the resulting PIE curve shape or onset values are observed. These observations indicate that there are minimal differences in the internal excitation of sputtered neutrals leaving the surface with different velocities or at different times for these systems.

Extensive gold cluster ion formation is seen upon ion bombardment (Figure 3.2b, top), and neutral clusters are also produced, as they have been observed on other metal substrates.[38] PIE curves are obtained for gold clusters with up to four Au atoms.

The PIE for Au exhibits a sharp rise (Figure 3.6a). Linear extrapolation of the sharp rise to the baseline yields a threshold ionization energy of 9.22 ± 0.18 eV, which is in good agreement with literature values for the ionization energy (see Table 3.3). Au can only possess electronic excitations, but the lowest electronically excited state lies over 1.1 eV above the ground state.[39] The lack of features in the Au PIE 1.1 eV below the ionization threshold suggests the absence of electronic excitation.

Au_n	This work	Literature experimental	Literature theoretical
n=1	9.22±0.18	9.23[a,b]; 9.26[c]	9.78[d]
n=2	8.82±0.18	9.50[a,e]; 9.16[c,f]	9.84[d,e]; 9.81[d,f]
n=3	~7.5	7.50[a,e]; 7.27[c,f]	Linear geometry: 9.05[d,e]; 7.30[d,f] Triangular Geometry: 7.32[d,e]; 7.30[d,f]; 7.21[g,e]
n=4	7.82±0.18	8.60[a,e]	8.37[d,e], 8.34[d,f], 8.24[h,f]

Table 3.3: Au_n (n = 1, 2, 3, 4) observed ionization thresholds compared to corresponding previous experimental and theoretical values for the ionization energies. All energies are in eV.

[a]Electron impact from Ref. [40]; [b]Evaluated arc spectrum from Ref. [41]; [c]Charge-transfer bracketing and FTICR-MS from Ref. [42]; [d]Ref. [43]; [e]Vertical ionization energy; [f]Adiabatic ionization energy; [g]Ref. [44]; [h]Ref. [45]

Au_2 has the highest maximum postionization intensity of all clusters sputtered from the Au surface. Analysis of the Au_2 PIE curve (Figure 3.6b) yields an ionization threshold of 8.82 ± 0.18 eV. This value for the dimer ionization threshold is 0.34 eV lower than the adiabatic ionization energy measured by charge-transfer bracketing and FTICR-MS,[42] indicating that neutral Au_2 leaves the surface with significant amounts of internal energy. In general, these excitations may be rotational, vibrational, or electronic in nature; however the first excited electronic state for Au_2 lies 1.9 eV above the ground state.[46] Since there are no observable features in the PIE curve 1.9 eV below the ionization threshold, electronic excitation in ion-sputtered neutral Au_2 appears to be negligible.

The Au_3 PIE (Figure 3.6c) has a more gradual slope at the ionization threshold compared to the onsets for the monomer, dimer and tetramer. This slow rise may be due to the contributions from two low-lying geometries of the neutral trimer (linear and triangular) that have been calculated to lie within 0.02 eV[44] to 0.04 eV[43] of each other. With this small energy difference, it seems likely that both isomer structures would be populated within the sputtered neutral plume. The linear and triangular structures both have calculated adiabatic ionization energies of 7.3 eV; however, their vertical ionization energies are 9.05 eV and 7.32 eV, respectively.[43] This indicates that the linear isomer will have a gradual PIE onset due to poor Franck-Condon overlap, in addition to broadening from thermal vibrations in the neutral cluster.

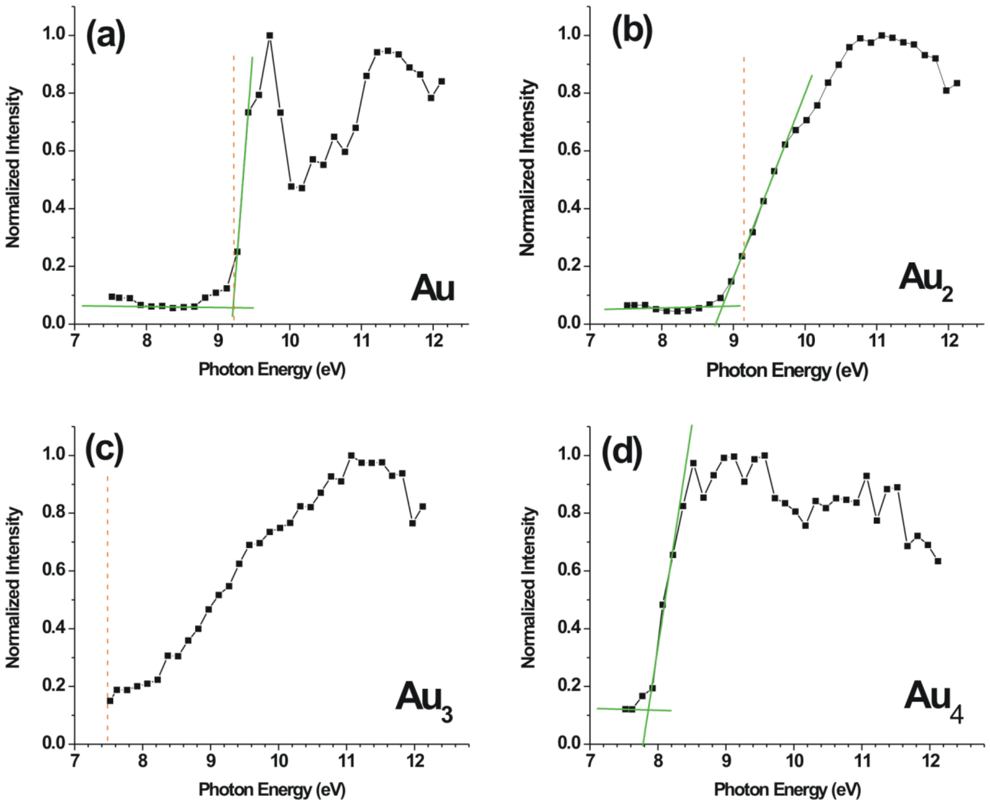

Figure 3.6: PIE curves for (a) Au, (b) Au$_2$, (c) Au$_3$, and (d) Au$_4$ from Bi$_3^+$ primary ion bombardment. The green lines are the extrapolation lines used to evaluate the ionization threshold values. The literature experimental adabative ionization energies taken from Table 3.3 are indicated by vertical orange dased lines, when available.

While this can explain the slow ionization onset, the proximity of the ionization threshold to the lowest accessible photon energy of 7.5 eV prevents the accurate determination of the baseline and thus does not allow us to constrain the ionization threshold above or below 7.5 eV.

Analogous analysis of the Au$_4$ PIE (Figure 3.6d) yields an ionization threshold of 7.82 ± 0.18 eV, which is 0.78 eV below literature values for the vertical ionization energy for Au$_4$.[40] Like the trimer, the tetramer has various energetically low-lying structural isomers that have been calculated including the planar rhombus and the planar “Y” shape that lie within 0.21 eV of each other.[43] In another study, Kim *et al.* calculates the linear structure for the neutral to be 0.39 eV higher in energy than a two-dimensional rhombus structure.[44] These differences are somewhat larger than the aforementioned energy differences calculated between the linear and triangular trimer isomers, implying that the different tetramer isomers are less likely populated. From the sharp rise of the Au$_4$ PIE, there appears to be a good Franck-Condon overlap of the neutral and cation tetramer geometries, which is supported by the similar values for the rhombic Au$_4$ vertical and adiabatic ionization energies calculated by Wang *et al.*[43]

The photoionization thresholds obtained in this experiment for neutral atoms sputtered from both GaAs and Au agree with literature experimental values, while the ionization thresholds observed for ion sputtered neutral clusters (see Tables 3.2 and 3.3) exhibit ~0.3 eV shifts to lower energies with respect to their literature adiabatic ionization energies. For Au_3 and Au_4, low-lying isomers and the degree of Franck-Condon overlap between the neutral and cation geometries may play a role in the ionization onset slope in the PIE curve, however, there are no clear signs of direct electronic excitation. It is likely that the observed shifts in ionization energy are due to the unresolved vibrational and rotational excitations within the neutral clusters. This view is supported by previous work where spectral fitting yielded vibrational temperatures of 2700 K and rotational temperatures of 6700 K for sputtered silver dimers.[47]

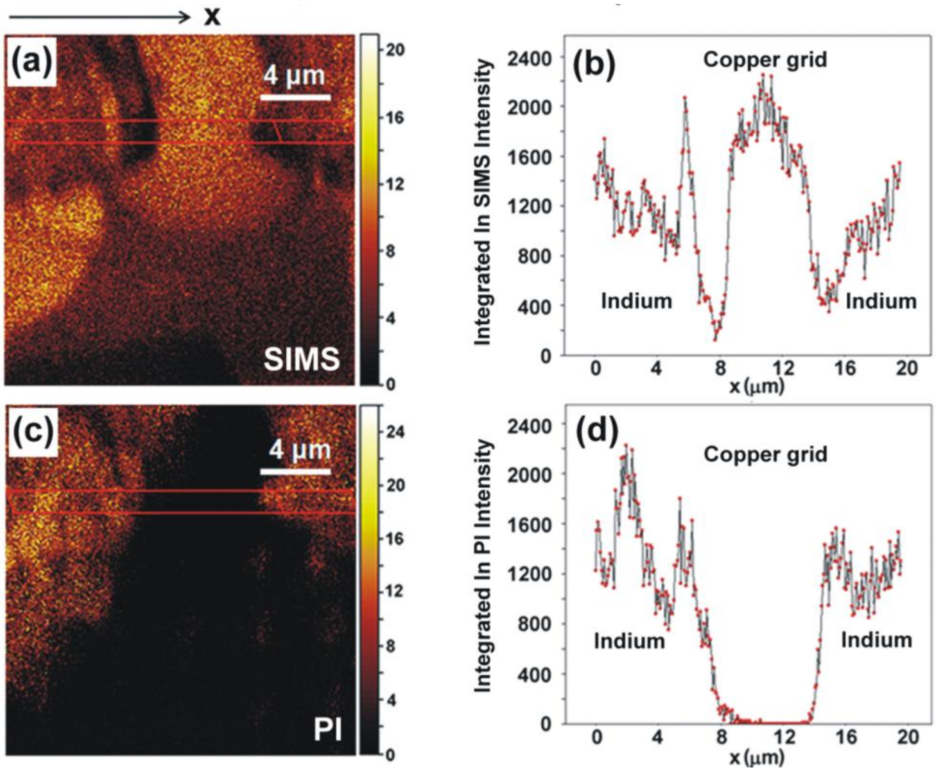

Figure 3.7: (a) SIMS indium image over a 20 µm x 20 µm area, at a corner of the square copper transmission electron microscopy (TEM) grid. (b) Integrated line scan of the red selection of (a) as a function of x. (c) Corresponding indium postionization (PI) image taken at 7.5 eV photon energy, and (d) the integrated line scan resulting from the same area selection in red for the postionization image. The color scale bars to the right of (a) and (c) indicate the indium counts per pixel. Images are collected using Bi_3^+ pulse lengths of 1000 ns and spot size of ~100 nm (256 x 256 raster, 130 scans, 850 seconds per data set).

Wavelength tunable synchrotron radiation provides a convenient means of generating PIE curves that can be used to study the internal excitations in ion-sputtered neutrals. Such quantitative understanding of the internal energies of ion-sputtered surface species is important for molecular imaging with techniques like SIMS and SNMS, in which minimization of fragmentation and sample damage is desirable; however, the wavelength tunability of the synchrotron can also be used to verify mass spectral assignments. The added selectivity of synchrotron VUV postionization and its application to chemical imaging is described in the following section.

3.3.4 Applications to Chemical Imaging

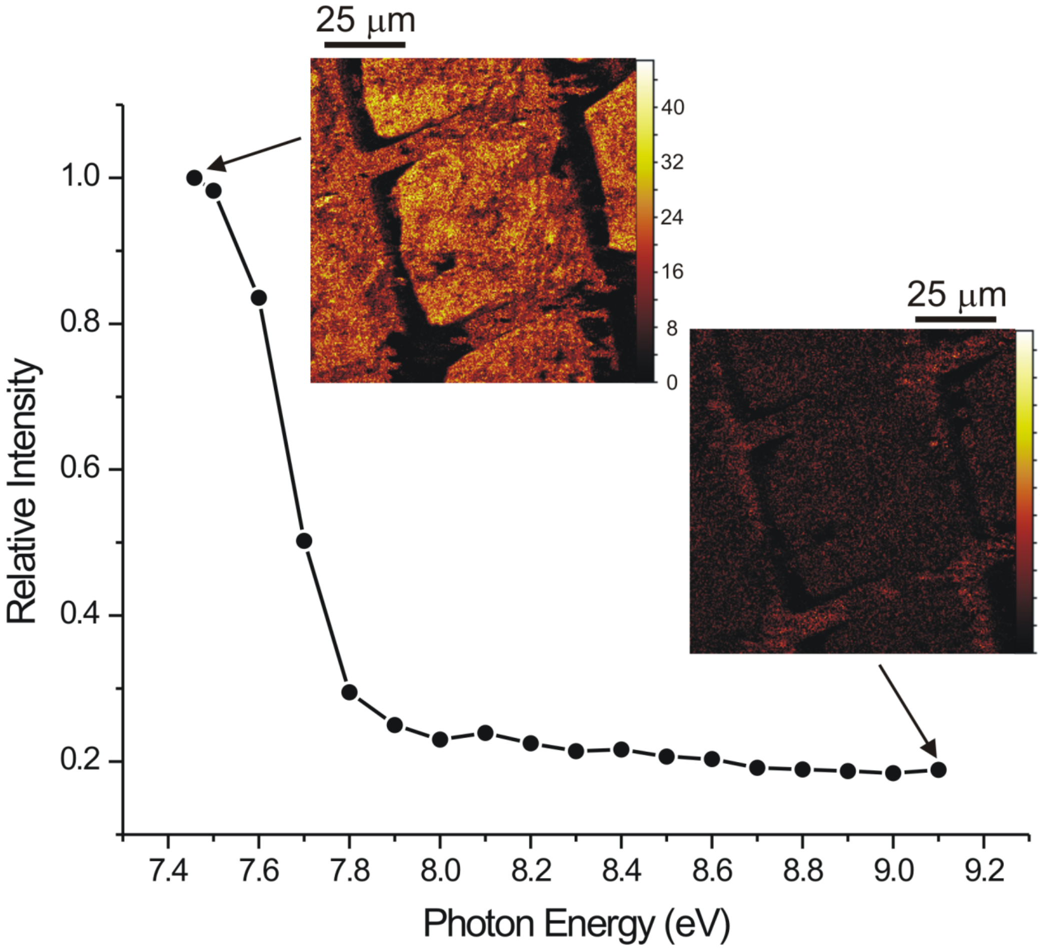

Figure 3.8: Postionization image of indium collected using 7.5 eV photons and 9.1 eV photons overlaid on their respective regions of the indium PIE curve (0.1 eV steps, 7.5 eV – 9.1 eV). Images are collected using a ~250 nm Bi_3^+ primary ion beam spot size with 800 ns pulse lengths and reflect a 100 µm x 100 µm area of the square copper TEM grid on indium (256 x 256 pixel raster, 21 scans, 550 seconds per data set).

Figure 3.7 shows the indium SIMS and postionization images of a 20 µm x 20 µm region of a copper grid pressed into a flattened indium wire (an expanded view of the grid is shown in Figure 3.8). The images in Figure 3.7 are accumulated over 130 scans with a 256 x 256 pixel raster over 852 seconds with ~100 nm Bi_3^+ primary ion spot size and 1000 ns pulse lengths. From the SIMS image of indium in Figure 3.7a, the corner of a grid square is visible, but the indium SIMS intensity distribution is misleading. A line scan of the area selected in red across the copper gridline (Figure 3.7b) shows that the SIMS indium signal is actually higher in the regions of the copper grid, where a minimum in intensity would be expected from abundance arguments. This observation is likely due to the enhancement of indium secondary ion formation atop the copper grid substrate (a matrix effect). In contrast, the imaged indium postionization intensity distribution (Figure 3.7c) collected using 7.5 eV photons over the same area reflects the expected composition of the surface. An indium postionization linescan of the same selected area, shown in Figure 3.7d, illustrates that the indium postionization signal intensity over the copper grid is lower than that over the pure indium metal. This observation reflects the much smaller effect that the local chemical environment has on the neutral desorption yields compared to the ionization-desorption yields of the secondary ions. Postionization images of copper and the indium-copper heterodimer (both collected using 9.1 eV photons, not shown) of the same sample area also reflect the expected signal intensity distributions, with copper localized primarily over the copper grid line (the dark region in the indium postionization image of Figure 3.7c), and indium-copper localized primarily on the apparent bright spots on the copper grid in Figure 3.7a, where the more pliable indium smeared onto the grid. Thus, due to greatly reduced imaging artifacts from matrix effects, imaging with postionization helps data interpretation even for simple chemical systems.

In addition to yielding images that more accurately reflect the chemical composition of the surface, single photon postionization with tunable synchrotron VUV radiation permits more conclusive identification of chemicals by revealing differences in photoionization cross sections as well as m/z. In this case of the copper grid on indium, the sample's mass spectrum is relatively simple, containing only two main constituents. Even so, copper and indium postionization signals behave differently at the two photon energies investigated (7.5 eV and 9.1 eV), in accord with their photoionization cross sections.

Indium has several autoionizing resonances near 7.5 eV,[48] and can therefore be imaged well using 7.5 eV photons. Figure 3.8 shows the 7.5 eV postionization image of indium on the left, overlaid with the indium PIE curve. In this expanded view, one may note that the indium postionization signal levels fluctuate over different regions of the copper grid due to the non-uniform smearing of indium over the grid lines; however the maximal indium postionization intensities appear over the indium metal. At 9.1 eV, the indium photoionization cross section is smaller, and this fact is reflected by lower indium postionization signal intensities across the image shown on the right of Figure 3.8. Here it should be noted that indium signals in the 9.1 eV image are quite low, and therefore the image shows evidence of incomplete subtraction of the SIMS background (i.e. the "matrix effect" that enhances the indium SIMS signal over the copper grid is clearly visible).

Copper postionization signals integrated over the entire imaged area (not shown) exhibit the opposite trend, increasing in intensity as the light is tuned from 7.5 eV to 9.1 eV; however the copper postionization images at the two different photon energies do not clearly reflect this overall intensity change due to the low signal intensity of the copper postionization (*i.e.* the fractional change in ionization probability is not large enough to be seen on a pixel-by-pixel level). Nevertheless, the wavelength dependence of individual postionization peak intensities provides another parameter with which to verify mass assignments, which is particularly valuable for imaging mass spectrometry when hundreds of compounds exist within a given sample.

3.4 Conclusion

A keV bismuth cluster ion source is used together with tunable synchrotron VUV light to obtain postionization mass spectra and PIE curves for sputtered neutrals from GaAs and Au surfaces from Bi^+, Bi_3^+ and Bi_3^{2+} primary ion bombardment. SIMS spectra are compared to the postionization mass spectra, revealing the complementary nature of the two techniques. While the larger cluster species are more efficiently detected through the positive secondary ions, smaller species such as Au, Au_2, and As are detected with nearly the same intensity as SIMS, and As_2 is about an order of magnitude stronger through the neutral channel. Scans of the VUV light wavelength allow PIE curves to be obtained. No notable changes in the ionization thresholds for the various sputtered neutrals are observed with the use of the different primary ion beams, although comparisons with previous experimental adiabatic ionization energies reveal that the ionization thresholds for neutral clusters are typically shifted by ~0.3 eV toward lower photon energies, likely due to vibrational and rotational excitations.

The utility of tunable VUV light for high spatial resolution chemical imaging is also demonstrated with the analysis of a copper TEM grid embedded in indium. With reduced signal dependences on the local chemical environment and the additional selectivity afforded by the different photoionization cross sections of the sputtered surface species, threshold single photon postionization with synchrotron VUV light promises to be a valuable technique for sub-micron imaging of chemically heterogeneous systems with mass spectrometry.

References

(1) Quinn, P. K.; Bates, T. S.; Coffman, D. J.; Covert, D. S. *Atmospheric Chemistry and Physics* **2008**, *8*, 1029.

(2) Castner, D. G.; Ratner, B. D. *Surf. Sci.* **2002**, *500*, 28.

(3) Brown, W. L.; Sosnowski, M. *Nucl. Instrum. Methods Phys. Res., Sect. B* **1995**, *102*, 305.

(4) Garrison, B. J.; Postawa, Z. *Mass Spectrom. Rev.* **2008**, *27*, 289.

(5) Thompson, M. W. *Vacuum* **2002**, *66*, 99.

(6) McPhail, D. *J. Mater. Sci.* **2006**, *41*, 873.

(7) Kraft, M. L.; Weber, P. K.; Longo, M. L.; Hutcheon, I. D.; Boxer, S. G. *Science* **2006**, *313*, 1948.

(8) Colliver, T. L.; Brummel, C. L.; Pacholski, M. L.; Swanek, F. D.; Ewing, A. G.; Winograd, N. *Anal. Chem.* **1997**, *69*, 2225.

(9) Lechene, C. P.; Luyten, Y.; McMahon, G.; Distel, D. L. *Science* **2007**, *317*, 1563.

(10) Fletcher, J. S.; Lockyer, N. P.; Vaidyanathan, S.; Vickerman, J. C. *Anal. Chem.* **2007**, *79*, 2199.

(11) Ostrowski, S. G.; Van Bell, C. T.; Winograd, N.; Ewing, A. G. *Science* **2004**, *305*, 71.

(12) Kollmer, F.; Bourdos, N.; Kamischke, R.; Benninghoven, A. *Appl. Surf. Sci.* **2003**, *203*, 238.

(13) Wood, M.; Zhou, Y.; Brummel, C. L.; Winograd, N. *Anal. Chem.* **1994**, *66*, 2425.

(14) Wittig, A.; Arlinghaus, H. F.; Kriegeskotte, C.; Moss, R. L.; Appelman, K.; Schmid, K. W.; Sauerwein, W. A. G. *Mol Cancer Ther* **2008**, *7*, 1763.

(15) Mollers, R.; Terhorst, M.; Niehuis, E.; Benninghoven, A. *Org. Mass Spectrom.* **1992**, *27*, 1393.

(16) Muller, U.; Schittenhelm, M.; Schmittgens, R.; Helm, H. *Surf. Interface Anal.* **1999**, *27*, 904.

(17) Terhorst, M.; Mollers, R.; Niehuis, E.; Benninghoven, A. *Surf. Interface Anal.* **1992**, *18*, 824.

(18) Willey, K. F.; Vorsa, V.; Braun, R. M.; Winograd, N. *Rapid Commun. Mass Spectrom.* **1998**, *12*, 1253.

(19) Becker, C. H. *Fresenius. J. Anal. Chem.* **1991**, *341*, 3.

(20) Wilson, K. R.; Jimenez-Cruz, M.; Nicolas, C.; Belau, L.; Leone, S. R.; Ahmed, M. *Journal of Physical Chemistry A* **2006**, *110*, 2106.

(21) Pan, Y.; Yin, H.; Zhang, T. C.; Guo, H. J.; Sheng, L. S.; Qi, F. *Rapid Commun. Mass Spectrom.* **2008**, *22*, 2515.

(22) Peterson, R. E.; Nair, A.; Dambach, S.; Arlinghaus, H. F.; Tyler, B. J. *Appl. Surf. Sci.* **2006**, *252*, 7006.

(23) Veryovkin, I. V.; Calaway, W. F.; Moore, J. F.; Pellin, M. J.; Lewellen, J. W.; Li, Y.; Milton, S. V.; King, B. V.; Petravic, M. *Appl. Surf. Sci.* **2004**, *231-232*, 962.

(24) Heimann, P. A.; Koike, M.; Hsu, C. W.; Blank, D.; Yang, X. M.; Suits, A. G.; Lee, Y. T.; Evans, M.; Ng, C. Y.; Flaim, C.; Padmore, H. A. *Rev. Sci. Instrum.* **1997**, *68*, 1945.

(25) Berkowitz, J. *Photoabsorption, Photoionization, and Photoelectron Spectroscopy*; Academic Press, Inc.: London, 1979.

(26) Marr, G. V.; Austin, J. M. *J. Phys. B: At. Mol. Opt. Phys.* **1969**, *2*, 107.

(27) Mazarov, P.; Samartsev, A. V.; Wucher, A. *Appl. Surf. Sci.* **2006**, *252*, 6452.

(28) Yamamura, Y.; Tawara, H. *Atomic Data and Nuclear Data Tables* **1996**, *62*, 149.

(29) Yamamura, Y., Itikawa, Y., and Itoh, N. “Angular dependence of sputtering yield of monoatomic solids,” Institute of Plasma Physics, Nagoya University, 1983.

(30) Wucher, A. *Appl. Surf. Sci.* **2006**, *252*, 6482.

(31) Nagy, G.; Walker, A. V. *Int. J. Mass Spectrom.* **2007**, *262*, 144.

(32) Wucher, A.; Staudt, C.; Neukermans, S.; Janssens, E.; Vanhoutte, F.; Vandeweert, E.; Silverans, R. E.; Lievens, P. *New J. Phys.* **2008**, *10*.

(33) Rothlisberger, U.; Schar, M.; Schumacher, E. *Z. Phys. D-Atoms Mol. Clusters* **1989**, *13*, 171.

(34) Bhatia, K. S.; Jones, W. E. *Can. J. Phys.* **1971**, *49*, 1773.

(35) Yoo, R. K.; Ruscic, B.; Berkowitz, J. *J. Chem. Phys.* **1992**, *96*, 6696.

(36) Balasubramanian, K. *Chem. Rev.* **1990**, *90*, 93.

(37) Moore, C. E. *Atomic Energy Levels*, Circ. no. 467 ed.; National Bureau of Standards 467: Washington, DC, 1952; Vol. 2.

(38) Staudt, C.; Heinrich, R.; Wucher, A. *Nucl. Instrum. Methods Phys. Res., Sect. B* **2000**, *164-165*, 677.

(39) Moore, C. E. Atomic Energy Levels; Circ. no. 467 ed.; Commerce, U. S. D. o., Ed.; National Bureau of Standards 467: Washington, DC, 1958; Vol. 3; pp 186.

(40) Jackschath, C.; Rabin, I.; Schulze, W. *Ber. Bunsen-Ges. Phys. Chem.* **1992**, *96*, 1200.

(41) Platt, J. R.; Sawyer, R. A. *Physical Review* **1941**, *60*, 866.

(42) Cheeseman, M. A.; Eyler, J. R. *J. Phys. Chem.* **1992**, *96*, 1082.

(43) Wang, J.; Wang, G.; Zhao, J. *Phys. Rev. B* **2002**, *66*, 035418.

(44) Lee, H. M.; Ge, M. F.; Sahu, B. R.; Tarakeshwar, P.; Kim, K. S. *J. Phys. Chem. B* **2003**, *107*, 9994.

(45) Ray, A. K. *Computational Materials Science* **2002**, *25*, 279.

(46) Das, K. K.; Balasubramanian, K. *J. Mol. Spectrosc.* **1990**, *140*, 280.

(47) Wucher, A. *Phys. Rev. B* **1994**, *49*, 2012.

(48) Karamatskos, N.; Muller, M.; Schmidt, M.; Zimmermann, P. *J. Phys. B: At. Mol. Opt. Phys.* **1984**, *17*, L341.

Chapter 4

SIMS and VUV-SNMS of Organic Molecules and Their Internal Energies

Adapted with permission from Analytical Chemistry, 2010, 82 (9) pp 3905-3913. Copyright 2010 American Chemical Society.

Vacuum ultraviolet photoionization coupled to secondary neutral mass spectrometry (VUV-SNMS) of deposited tryptophan and thymine films are performed at the Chemical Dynamics Beamline. The resulting mass spectra show that while the intensity of the VUV-SNMS signal is lower than the corresponding secondary ion mass spectroscopy (SIMS) signal, the mass spectra are significantly simplified in VUV-SNMS. A detailed examination of tryptophan and thymine neutral molecules sputtered by 25 keV Bi_3^+ indicates that the ion-sputtered parent molecules have ~2.5 eV of internal energy. While this internal energy shifts the appearance energy of the photofragment ions for both tryptophan and thymine, it does not change the characteristic photoionizaton efficiency (PIE) curves of thymine versus photon energy. Further analysis of the mass spectral signals indicate that approximately 80 neutral thymine molecules and 400 tryptophan molecules are sputtered per incident Bi_3^+ ion. The simplified mass spectra and significant characteristic ion contributions to the VUV-SNMS spectra indicate the potential power of the technique for organic molecule surface analysis.

4.1 Introduction

Imaging mass spectrometry, particularly secondary ion mass spectrometry (SIMS), has long been successfully utilized in materials science studies. Recently, however, there has been growing interest in applying this tool to problems of biological relevance.[1,2] For example, in 2006 lipid domains within prepared lipid membranes were imaged with a spatial resolution of ~100 nm using SIMS,[3] and in 2007 the fate of fixed nitrogen in host cells was mapped using multi-isotope imaging mass spectrometry.[4] A major advantage of imaging mass spectrometry for biological studies is that no sample labeling is required since the chemical species are identified by their masses. Furthermore, in the case of SIMS, the spatial resolution is not restricted by the optical diffraction limit since the desorption source is atomic or molecular ions, yielding images with resolution on the order of tens of nanometers. However, there are also complications arising from this methodology. In particular, SIMS is not a quantitative method because the formation of secondary ions depends strongly on the local environment, *i.e.* the matrix effect, and the sensitivity for different compounds can vary by orders of magnitude. These make interpreting the resulting images difficult, especially for chemically complex, real-life systems.

Secondary neutral mass spectrometry (SNMS) was developed to access the neutral portion of the ion-sputtered molecules. Compared to SIMS, where the desorption and ionization steps are both initiated by primary ions, SNMS utilizes electrons or photons to postionize the neutral molecules. Because the ionization step is decoupled from the desorption step, SNMS can yield quantitative images.[5] However, due to the high energy needed to ionize most molecules, SNMS experiments typically employ table top lasers via a multiphoton ionization scheme to probe both inorganic and organic samples.[6-9] The excess energy deposited into the molecules during such ionization processes often result in molecular fragmentation, complicating the mass spectrum and limiting the applicability of this technique.[10] This is further compounded by the fact that the neutral molecules already have a certain amount of internal energy imparted by the sputtering process. To address this issue of dissociative photoionization, it is valuable to determine the amount of internal energy that is present in the ion-sputtered molecules prior to photoionization.

Previous experimental studies have been performed on inorganic surfaces to analyze the energetics of the ion-sputtered atoms and molecules. In particular, in a resonant two-photon ionization experiment, it was determined that Ag_2 clusters sputtered by 5 keV Ar^+ had a vibrational temperature of 2000-3000 K and a rotational temperature of 5000-8000 K.[11] More recently, by comparing photoionization efficiency (PIE) curves of In_n clusters sputtered by 15 keV Xe^+ with those that are in a molecular beam, it was found that the ion-sputtered In_2 clusters have an internal temperature of 4000 K.[12] On the other hand, molecular dynamics simulations show that over organic surfaces some population of the ion-sputtered molecules may remain intact with relatively low internal energy.[13] Therefore, by establishing the extent of internal excitation within these intact ion-sputtered molecules, one can evaluate the applicability of the SNMS technique to various classes of organic compounds.

Recently, VUV-SNMS was implemented at the Chemical Dynamics Beamline at the Advanced Light Source, utilizing tunable vacuum ultraviolet (VUV) radiation from a synchrotron source to perform single photon ionization of the ion-sputtered neutral molecules.[14] Single photon ionization permits a controlled amount of internal energy to be deposited into the molecule,[15] and the wide tunability of a synchrotron photon source allows measurements of photoionization efficiency versus photon energy, which are characteristic of individual chemical species and sensitive to internal energies. Using this technique it is possible to determine the internal energies of the ion-sputtered molecules.[16] In this chapter, the application of VUV-SNMS to thymine and tryptophan, a DNA base and an amino acid, respectively, is used to obtain the typical desorption efficiencies and internal energies of the intact parent molecules.

4.2 Experimental Methods

A modified commercial secondary ion mass spectrometer (ToF.SIMS V, ION-TOF Inc.), operating under ultrahigh vacuum conditions (10^{-9} mbar, 1 mbar = 0.1 kPa), is coupled to the VUV light source on the Chemical Dynamics Beamline at the Advanced Light Source; the setup has been described in detail previously.[14] Briefly, pulses of Bi_3^+ primary ions impact the sample surface at 45°, generating secondary ions and neutrals. The secondary ions and photoionized neutrals are extracted into a reflectron time-of-flight (ToF) mass spectrometer with a two-meter long path length. The SIMS data are acquired with ToF conditions that are optimized for secondary ion detection, while the VUV-SNMS data are acquired with ToF settings optimized for photoion detection.[14] The samples of thymine and tryptophan used in this experiment are purchased from Sigma Aldrich (both ≥99% purity), deposited by suspending in methanol and spin coated onto silicon substrates. The samples are analyzed without sputter-cleaning to avoid unnecessary damage to the organic surfaces. Each analysis is performed in an area of 150 µm x 150 µm, with a 64 pixel x 64 pixel raster. The thymine data were acquired with a 260 µs cycle time, equivalent to a 3.8 kHz repetition rate, and the tryptophan data were acquired with a 280 µs cycle time.

The undulator-based beamline, described in detail elsewhere,[17] generates wavelength-tunable, quasi-continuous (500 MHz) VUV light. The synchrotron was recently upgraded to operate in top-off mode,[18] increasing the photon flux available to each beamline. The spectral resolution of the synchrotron output used in this work is determined to be 0.2 eV by measuring the full width at half maximum (FWHM) of the autoionizing resonance of ion-sputtered silicon atoms at 9.8 eV. Argon is used in the gas filter to remove higher harmonics from the undulator emission. Also situated in the gas filter is a small (100 µm) horizontal slit that narrows the vertical height of the VUV beam, delivering ~10^{15} photons/s to the apparatus with a spot size of approximately 200 µm (vertical) x 600 µm (horizontal). Photon flux curves as a function of energy are determined using a NIST-calibrated photodiode (SXUV-100, International Radiation Detectors) attached to the light exit port.

Due to the non-conductive nature of the organic surfaces studied here, a new ion extraction scheme is utilized to enhance the detection of photoionized secondary neutrals. Figure 4.1 depicts the main pulsed extraction schemes that are used. Typically, in the positive ion mode, a 10 µs long -2000 V pulse is applied to the extractor with 0 µs delay (Figure 4.1a). In this case, the extractor is at -2000 V when the bismuth ion pulse impacts the surface, resulting in an extraction scheme that is the same as DC extraction for the secondary ions and neutrals; the advantage is that the background signal arising from the VUV ionization of background gas is significantly reduced since the ions are not being continuously extracted into the ToF. Another possible extraction scheme is to delay the extraction pulse with respect to the bismuth pulse such that the extractor sits at ground potential when the bismuth ion pulse impacts the surface (Figure 4.1b). This pulsing scheme is advantageous because it improves the mass resolution of VUV-SNMS signal, since it allows for the accumulation of photoionized molecules in the extraction region before the voltage pulse is applied.

This improved mass resolution, as illustrated in Figure 4.2, is a necessary feature when analyzing organic samples. The major disadvantage of this scheme is that the secondary ions and the photoionized secondary neutrals have very similar flight paths through the ToF, making suppression of secondary ions difficult. Furthermore, the electrically insulating organic surface can cause the secondary ion signal to fluctuate from scan to scan, which significantly complicates the separation of VUV-SNMS signal from the secondary ion background. Therefore, a double extraction pulse scheme (Figure 4.1c) is used for the organic samples studied here. The first pulse is used to extract the prompt secondary ions; due to the short duration of

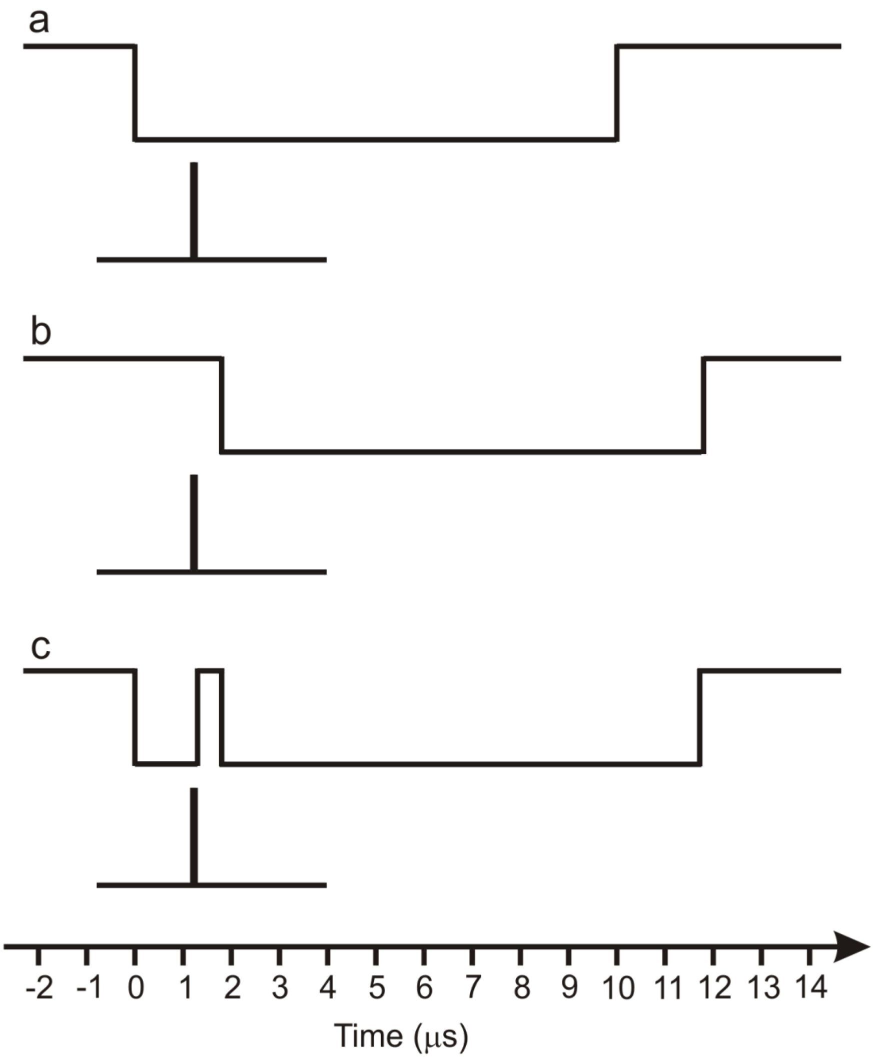

Figure 4.1: Depiction of the various pulsed extraction schemes that can be used in the VUV-SNMS experiment. The voltages of the pulses are not to scale. In (a) and (b) the 10 μs long -2 kV extraction pulse is illustrated above the 50 ns long +25 kV bismuth pulse. The double extraction pulse scheme is illustrated in (c).

this pulse, only a small mass range of secondary ions can reach the detector, reducing the secondary ion background. Because most of the secondary neutrals are not yet photoionized during this first pulse, they are unaffected in their initial trajectory. The second pulse acts as the normal delayed extraction pulse for the photoionized secondary neutrals. While some secondary ions still reach the detector with this extraction scheme, it is possible to adjust the timing such that the mass range of interest can be relatively free of background signal.

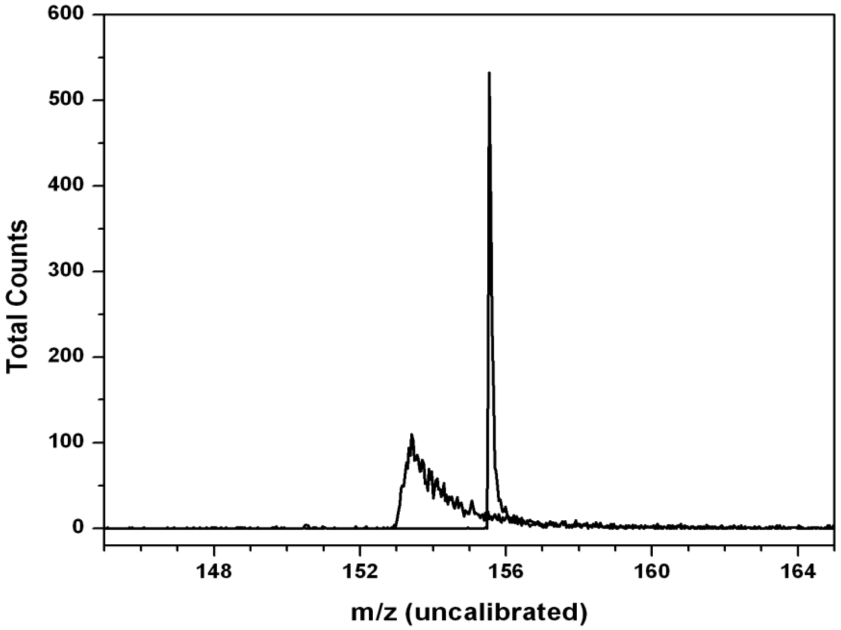

Figure 4.2: VUV-SNMS of As_2 acquired at 10.5 eV photon energy with 50 ns of Bi_3^+. The effect of varying the extraction pulse delay with respect to the bismuth pulse can be seen. The spectrum with lower mass resolution is acquired with 0 µs delay on the extraction pulse (as depicted in Figure 4.1a). The spectrum with higher mass resolution is acquired with 1.6 µs delay on the extraction pulse (as depicted in Figure 4.1b).

4.3 Computational Details

Geometry optimization and vibrational frequency calculations are carried out for tryptophan, thymine and their fragments at the B3LYP level with the 6-311+G(d,p) basis set using the Gaussian 03 program.[19] Relative energies and ionization energies are obtained by subtracting the computed energy of the final state from the initial state, including the zero-point energy corrections. For thymine, the Gaussian 03 output files are used in the FCFGAUS program of Ervin *et al.*[20] for the Franck-Condon simulation, in which the Duschinsky rotation matrix and the displacement vectors are calculated. The resulting simulated photoelectron spectrum is visualized with the PESCAL[21] program.

For the simulation of PIE curves of the diatomic metal clusters, a Mathcad program is used to solve the Schrodinger equation for the vibrational potential using the 1-dimensional DVR (discreet variable representation) method.[22] Morse potentials are calculated for the neutral and cation dimers using experimental values when available,[23,24] and theoretical values otherwise (Au_2 and As_2 cations are calculated at the CCSD(T) level with cc-pVTZ-pp[25] and cc-pVTZ basis sets, respectively, using the Gaussian 03 program[19]). A total of 300 particle-in-a-box basis sets are used for the simulation, and the resulting wave functions for the initial state (neutral dimer) and final state (cation dimer) are used to calculate the Franck-Condon factors. The simulated photoelectron spectrum is integrated to give the PIE curve. The results are convoluted with a Gaussian width of 2700 cm^{-1}, corresponding to the resolution of the VUV light used for the experimental PIE curves. The Boltzmann distribution for the vibrational population of the initial state is included to simulate the PIE curves for various vibrational temperatures.

4.4 Results and Discussion

4.4.1 Mass Spectra of Organic Molecules

VUV-SNMS signals are observed in our laboratory recently for numerous organic samples, e.g. polycyclic aromatic hydrocarbons (coronene, chrysene, etc.), amino acids (phenylalanine, asparagine, etc.), various DNA bases, and other biologically-relevant compounds such as coniferyl alcohol, a component of lignin. However, for the purpose of analyzing internal energies of ion-sputtered molecules, only two compounds, tryptophan and thymine, are discussed here. Shown in Figures 4.3 and 4.4 are the VUV-SNMS mass spectra of thymine and tryptophan acquired at various photon energies ranging from 8 eV to 10 eV, as well as the corresponding SIMS mass spectra; the SIMS and VUV-SNMS of each sample are acquired over the same area on the sample surface to minimize variations. The VUV-SNMS mass spectra of thymine show a dominant feature at m/z = 126, corresponding to the thymine parent, and its photon energy dependence agrees well with the ionization onset of thymine at 8.9 eV.[26] An additional feature at m/z = 55 is visible at 10 eV and 9.5 eV photon energy (Figures 4.3a and 4.3b, respectively), which corresponds to the $C_3H_5N^+$ fragment of thymine. The VUV-SNMS mass spectra of tryptophan, on the other hand, show only one predominant feature at the fragment mass of m/z = 130 for all photon energies. The SIMS mass spectra of thymine and tryptophan are generally more complicated, but for both species there is a relatively strong feature at the protonated parent mass.

Comparing the SIMS data to the VUV-SNMS data, one can see that each technique has an advantage over the other. SIMS shows a higher signal count with fewer bismuth ions used, albeit the protonated parent is favored over the parent in SIMS; VUV-SNMS has a simpler mass spectrum, with all dominant features easily assignable. The difference between the signal counts of the two methods is related to the difference in the ionization cross sections. In SIMS, the protonated parent is most likely formed through the collision of neutral molecules with cationic species that are generated by the very energetic desorption process. This “ionization” cross section is poorly quantified, and it can vary significantly depending on the local environment of the surface. On the other hand, in VUV-SNMS the photoions, e.g. for thymine, are formed from single photon ionization of the neutral thymine molecules. The photoionization cross section and branching fractions are well defined, making the signals depend, for the most part, only on the photon flux, the photon energy, and the desorption yield. Thus the comparatively lower signal count rate in VUV-SNMS is due to the cross section and the low peak power of the quasi-cw synchrotron source.

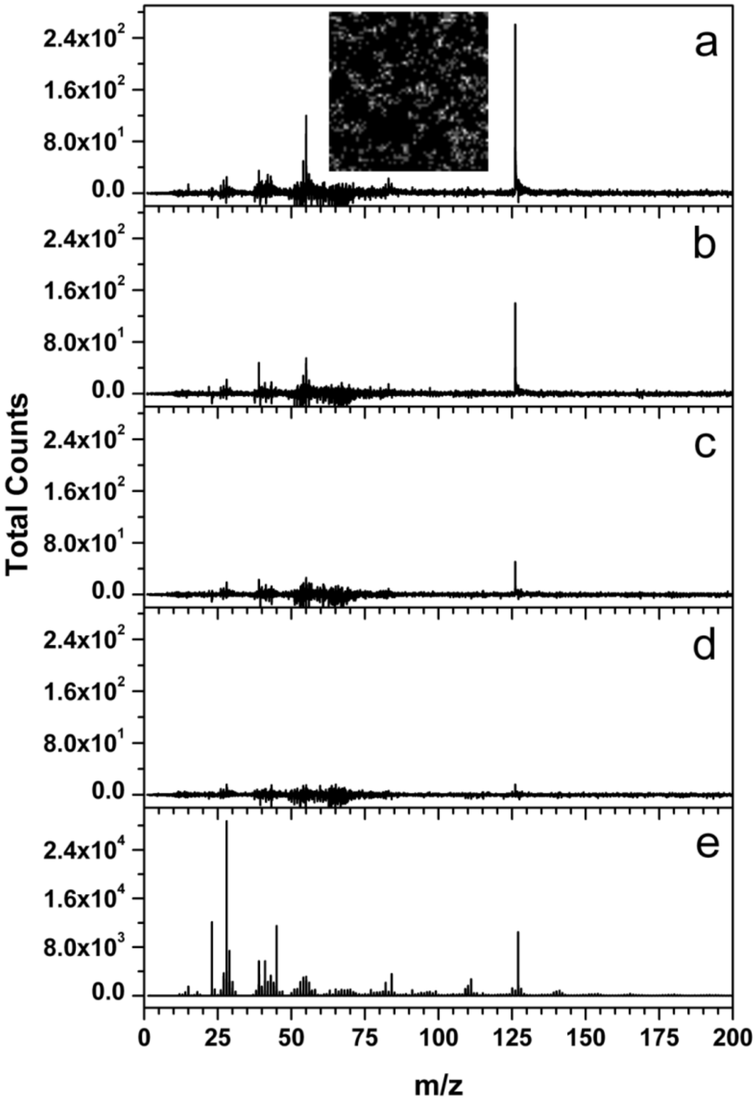

Figure 4.3 VUV-SNMS of thymine (50 ns of Bi_3^+, 25 scans) acquired at photon energies of 10 eV (a), 9.5 eV (b), 9 eV (c) and 8.2 eV (d). For comparison, the SIMS spectrum (12.5 ns of Bi_3^+, 25 scans) acquired over the same area is shown in panel (e). The VUV-SNMS spectra are acquired with ToF conditions optimized for photoion detection; the SIMS spectrum is acquired with ToF conditions optimized for secondary ion detection. In the VUV-SNMS spectra, the m/z = 126 feature corresponds to the thymine parent signal, while the m/z = 55 is the dominant cation fragment. The noise in the spectra around m/z = 50 is due to fluctuations in the SIMS background. In panel (a) also shown is an image of the m/z = 126 feature, showing the spatial distribution of thymine (150 x 150 µm^2, 64 pixel x 64 pixel raster). The SIMS mass spectrum shows a strong signal at m/z = 127, corresponding to protonated thymine.

In terms of the number of spectral features present, a dramatic difference can be seen between the VUV-SNMS and SIMS mass spectra of tryptophan. The SIMS mass spectrum (Figure 4.4d) exhibits many features, with a cluster of intense peaks every ~10 mass units, up to the protonated parent signal. The VUV-SNMS mass spectrum of tryptophan, on the other hand, is very simple. There is one dominant peak at m/z = 130, corresponding to the characteristic methylene indole cation fragment produced by dissociative photoionization. The difference in the mass spectra between VUV-SNMS and SIMS is well illustrated in this case. Many of the SIMS mass spectral artifacts, such as disproportionately strong Na^+ and K^+ signals and the ever-present hydrocarbon envelope at low masses, are not present in the VUV-SNMS mass spectrum.

This improvement over SIMS would be a great advantage when studying complex and chemically heterogeneous organic surfaces.

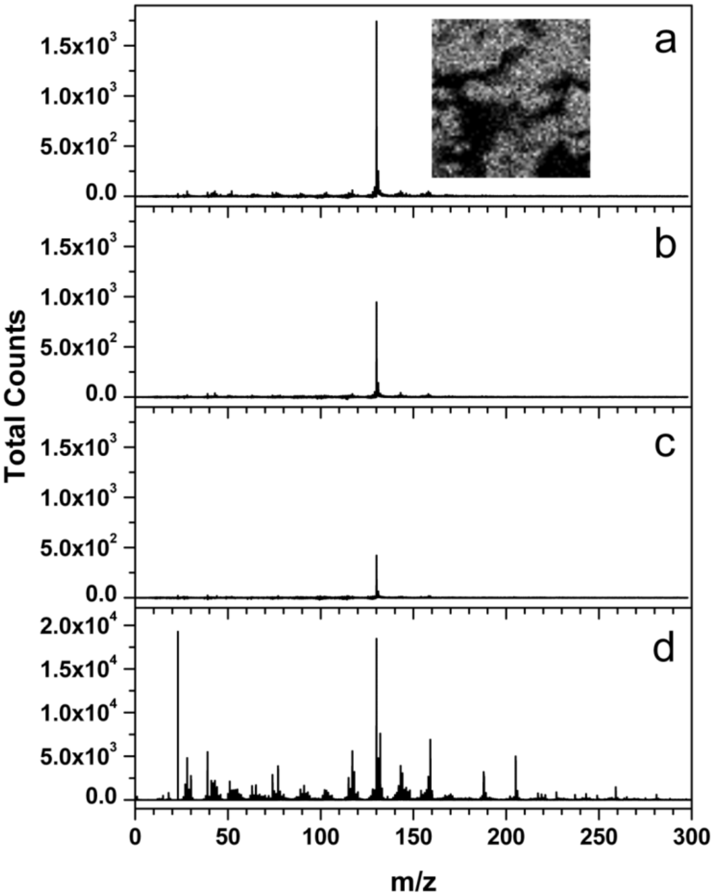

Figure 4.4 VUV-SNMS of tryptophan (50 ns of Bi_3^+, 15 scans) acquired at photon energies of 10 eV (a), 9 eV (b) and 8 eV (c). For comparison, the SIMS spectrum (12.5 ns of Bi_3^+, 15 scans) acquired over the same area is shown in panel (d). The VUV-SNMS spectra are acquired with ToF conditions optimized for photoion detection, while the SIMS spectrum is acquired with ToF conditions optimized for secondary ion detection. In the VUV-SNMS spectra, the dominant m/z = 130 feature corresponds to the methylene indole cation fragment. In panel (a) is also an image of the m/z = 130 feature, showing the spatial distribution of tryptophan (150 x 150 μm^2, 64 pixel x 64 pixel raster).

4.4.2 Desorption Yield

The neutral desorption yield can be estimated from the observed photoion intensity because VUV-SNMS utilizes well-defined ionization processes. Using the linear approximation of Beer's law, the number of neutral thymine molecules sputtered per second, N, is related to the number of thymine photoions observed per second, Z, by:[14]

$$\mathrm{N} \approx \frac{Z}{0.08\sigma F\tau} \quad . \tag{4.1}$$

The factor of 0.08 is the previously determined detection efficiency of the VUV-SNMS instrument measured with xenon.[14] The photoionization cross section of thymine,□ σ, is estimated to be ~20 Mb (1 Mb = 1 x 10^{-18} cm^2) at 10 eV photon energy, based on the experimental photoionization cross section of aromatic systems.[27] The average photon flux in the interaction region, F, is measured to be 1.2 x 10^{18} photons/($cm^2 \cdot s$) at 10 eV. The average time that each neutral thymine molecule spends in the VUV beam path, τ, is calculated assuming a typical kinetic energy of 1.5 eV[28] for the ion-sputtered thymine molecules, which yields a travel time of 0.2 µs through the measured 200 µm vertical FWHM of the VUV beam. The 10 eV VUV-SNMS mass spectrum shown in Figure 4.3a is acquired with 50 ns pulses of Bi_3^+ for 27 seconds at a 3.85 kHz repetition rate, resulting in 950 ion counts for thymine. From Equation 4.1, this would yield 9.2 x 10^7 neutral thymine molecules per second. The 50 ns pulses of Bi_3^+ running at 260 µs cycle time has a beam current of 0.38 pA, corresponding to 2.4 x 10^6 Bi_3^+ per second. Together, the estimated desorption yield is ~40 thymine molecules per Bi_3^+ ion for the dataset presented in Figure 4.3a. The VUV-SNMS image of thymine parent, also shown in Figure 4.3a, indicates that the organic surface is not uniform, despite the attempt to spin coat the sample uniformly; this is largely due to the fact that thymine does not dissolve well in methanol. As the image shows, thymine covers ~50% of the substrate surface. This means that only ~50% of the incident Bi_3^+ would result in useful yield. Taking this into account, the corrected estimated desorption yield of thymine is then ~80 neutral thymine molecules per incident Bi_3^+ ion.

A similar analysis can be applied to the tryptophan data acquired at 10 eV photon energy, shown in Figure 4.4a, where the m/z = 130 feature is a well-known cation fragment of tryptophan cation.[29] Using an estimated photoionization cross section of 60 Mb at 10 eV photon energy,[27] the observed 12000 counts of the m/z = 130 photoion in 17 seconds (280 µs cycle time or 3.57 kHz repetition rate) correspond to 6.1 x 10^8 tryptophan molecules per second, or ~280 tryptophan molecules sputtered per Bi_3^+ for the dataset presented in Figure 4.4a. The VUV-SNMS image of the m/z = 130 cation, also shown in Figure 4.4a, indicates that tryptophan has better substrate coverage than thymine, although it is still not uniform. Given the ~70% organic presence in the analyzed area, the corrected estimated desorption yield of tryptophan is ~400 neutral tryptophan molecules per incident Bi_3^+ ion.

There are several experimental parameters and associated uncertainties that should be taken into account when considering the derived desorption yields. In particular, there is no experimental absolute photoionization cross sections for thymine and tryptophan in the photon energy range studied here, hence the estimated values for the ionization cross sections may be inaccurate, although they should be correct within an order of magnitude. The substrate coverage variations of the organic samples do cause differences in the total signal detected from spot to spot. When taking this into account, the desorption yields from several different spatial areas of analysis present consistent values with ± 20% deviations. This fluctuation in signal also includes changes in the Bi_3^+ flux and other minor differences in the samples such as surface contaminants and thickness. Furthermore, there are also systematic errors in the estimated desorption yield. For instance, because the photoionized molecules are delay extracted, some of the ion-sputtered molecules that have higher kinetic energies would leave the extraction region before they can be pulsed into the ToF. This would favor the detection of lower kinetic energy molecules and would decrease the signal count. Also, in the case of thymine, any photo-induced fragmentation is not accounted for, which would again decrease the estimated desorption yield. This may account for the difference in the calculated desorption yield between thymine and tryptophan, as the former is derived from the detected parent signal alone and the latter is derived from the dominant photofragment.

The neutral desorption yield of thymine can also be compared to the protonated thymine signal observed in the SIMS mass spectrum. In Figure 4.3e, the SIMS spectrum, acquired with 12.5 ns pulses of Bi_3^+ at a repetition rate of 3.85 kHz in 27 seconds, has 23000 counts of protonated thymine. This is equivalent to 1.4×10^{-3} protonated thymine ions per incident Bi_3^+ ion. This value is at least 4 orders of magnitude less than the neutral thymine desorption yield calculated from VUV-SNMS over the same area, especially considering that the SIMS mass spectrum is acquired with non-delayed extraction and most likely has higher detection efficiency. This difference in yields highlights the advantage of accessing the neutral species in the desorption plume.

4.4.3 Internal Energies

Previous experiments[14] with VUV-SNMS over metal samples revealed that the PIE curves for both Au_2 and As_2 clusters display lower ionization onsets when compared to reference values. This shift is attributed to vibrational excitation in the neutral clusters imparted by the desorption process. Because there is only one vibrational mode in these dimers, a relatively simple simulation, as outlined in the computational details section, can be performed to extract the vibrational temperature of the neutral clusters. The simulated PIE curves for Au_2 and As_2 are compared to VUV-SNMS PIE curves previously obtained[14] with Bi_3^+ primary ions in Figure 4.5. The $0\text{-}0^+$ transitions in the simulated PIE curves are fixed to experimentally-determined ionization onsets,[30,31] leaving the intensity as the only adjustable parameter in the fit between VUV-SNMS PIE curves and simulated PIE curves. As Figure 4.5 shows, the simulations fit very well with the experimental data for both Au_2 and As_2 when vibrational temperatures of 5000 K and 4000 K, respectively, are used. Although the uncertainties in these values are high because there are only subtle differences in the simulated PIE curves in this temperature range, they nonetheless demonstrate the approximate amounts of internal energy imparted to the sputtered neutral metal clusters by the primary ion impact. These vibrational temperatures are also in good agreement with previous studies on other metal clusters.[11,12]

There is one major difference between organic molecules and the metal clusters that have been studied thus far, namely, the number of internal degrees of freedom available to the system. Organic molecules in the mass range of 100 to 200 daltons can have up to 100 or more vibrational modes, which at a temperature of 5000 K would correspond to tens of eV in internal energy. In comparison, Au_2 at the same temperature has only 0.4 eV of internal energy. Therefore, it is not straightforward to draw conclusions for organic systems based upon the results of the metal systems. In order to have a better grasp of the internal energy in ion-sputtered organic molecules, the VUV-SNMS results of tryptophan and thymine are examined.

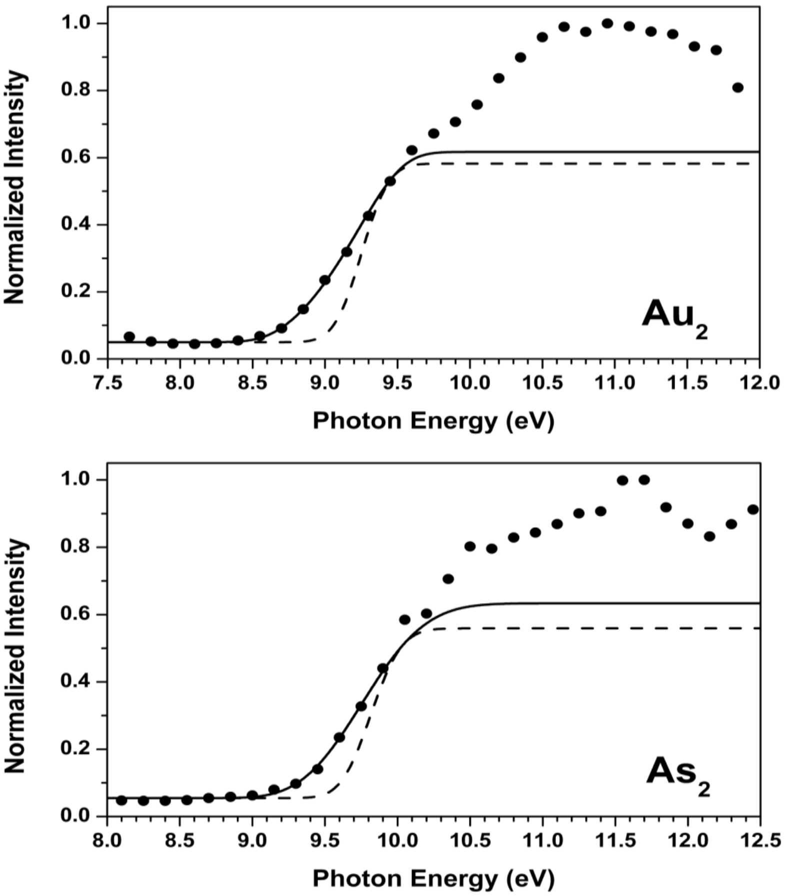

Figure 4.5 VUV-SNMS PIE curves of As_2 and Au_2 acquired with 100 ns of Bi_3^+ from ref [14] (•). The simulated PIE curves (for Au_2 T = 10 K (---) and T = 5000 K (—); for As_2 T = 10 K (---) and T = 4000 K (—)) are superimposed on the experimental curve. The method of simulation is discussed in the computational details section.

Shown in Figure 4.6 is the VUV-SNMS mass spectrum of tryptophan acquired with 8.25 eV photon energy. The insert gives a closer view of the spectral range around the parent mass at m/z = 204. The signal intensity for the parent mass is obviously much weaker than the intensity of the dominant fragment at m/z = 130. Nevertheless, the ratio between the two can be used to estimate the internal temperature of the ion-sputtered tryptophan. Wilson *et al.*[32] carried out an experiment at the Chemical Dynamics Beamline wherein they measured the temperature dependence of the parent-to-fragment ratio of tryptophan at 8.25 eV photon energy by desorbing the molecules from an aerosol particle by collisions with a heated target. Their results show that in the temperature range from 373 K to 573 K, the parent-to-fragment ratio of tryptophan has an exponential dependence on temperature. This well-defined dependence allows us to extrapolate the Wilson *et al.*[32] data to the ratio of 0.008 that is observed in the present VUV-SNMS mass spectrum. Shown in Figure 4.7 is the extrapolation plot, and from this the internal temperature of ion-sputtered tryptophan is estimated to be 850 K.

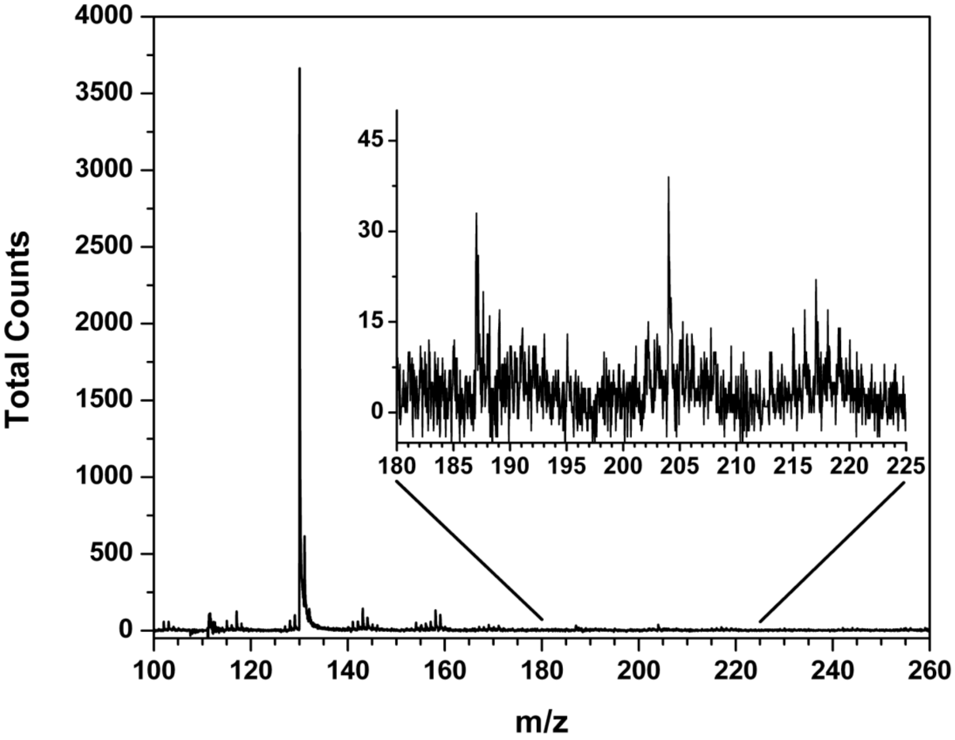

Figure 4.6 VUV-SNMS mass spectrum of tryptophan (50 ns of Bi_3^+, 100 scans) at 8.25 eV photon energy. The insert shows a magnified region around the parent mass at m/z = 204.

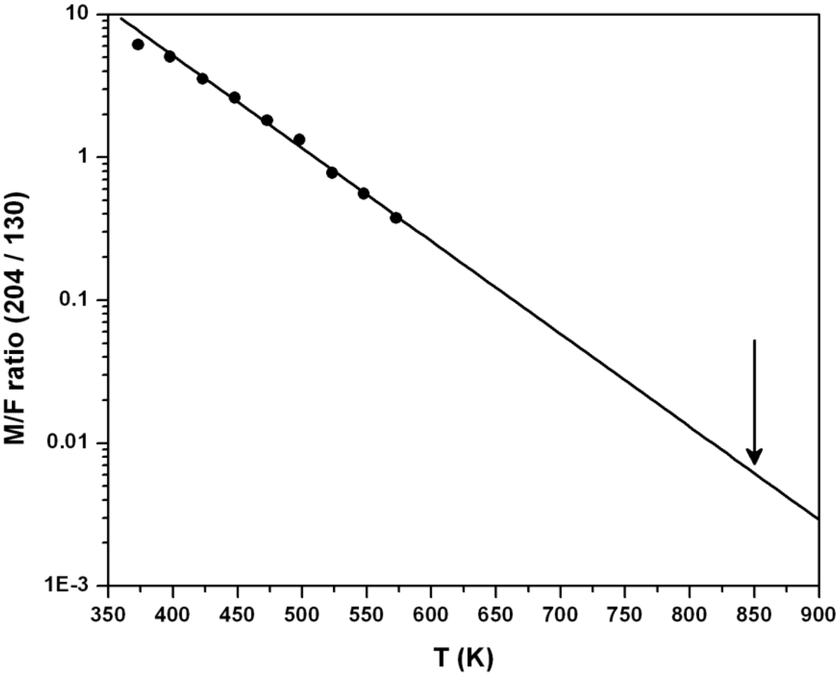

Figure 4.7: Extrapolation (solid line) of the temperature dependence of the parent-to-fragment ratio of tryptophan measured at 8.25 eV photon energy from reference [32]. The arrow indicates the ratio observed in the current VUV-SNMS studies.

To better understand the implications of this internal temperature, theoretical calculations as outlined in the computational details section are carried out for tryptophan and its fragments. Figure 4.8 illustrates the structures and relative energies of the tryptophan cation (m/z = 204) and the dominant fragments (m/z = 130 and m/z = 74). The fragmentation pathway that results in the formation of the m/z = 130 cation involves the cleavage of a C-C bond, indicated by the arrow in Figure 4.8, that connects the amino acid moiety to the indole rings.[29] Upon fragmentation, the charge remains on the methylene indole fragment, producing the observed m/z = 130 feature, while the neutral fragment, the deprotonated glycine with a mass of 74, is not detected. The calculated energy of the fragments is 1.15 eV higher than the calculated energy of the radical tryptophan cation, suggesting that at least 1.15 eV is needed to break the indicated bond when the tryptophan cation is in the ground state. Previous experiments by Wilson *et al.*[32] showed that the methylene indole fragment has an appearance energy of 8 eV at 373 K. The average vibrational energy of tryptophan at 373 K can be approximated by treating its vibrations as a collection of harmonic oscillators,[32] giving

$$E_{vib} = \sum_{i=1}^{s} \frac{h\nu_i}{h\nu_i / kT - 1}. \qquad (4.2)$$

Thus, the vibrational energy of tryptophan at 373 K is calculated to be 0.44 eV. Together with the 7.2 eV ionization energy of tryptophan,[33] the 8 eV appearance energy of the methylene indole fragment indicates that the fragmentation starts at 1.2 eV above the tryptophan cation ground state. This is in good agreement with the calculated 1.15 eV minimum energy needed for fragmentation.

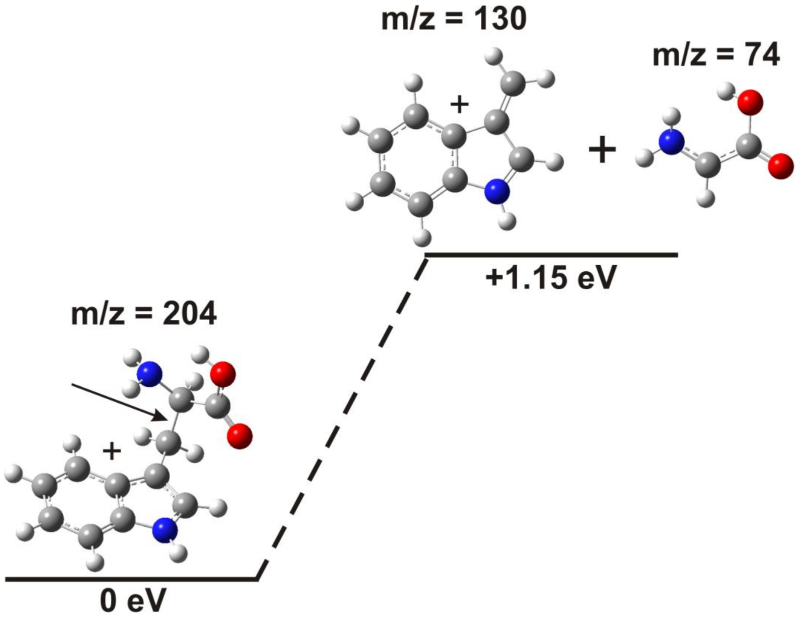

Figure 4.8 Relative energies, including zero-point energy corrections, of the tryptophan cation and the dominant fragments, calculated with B3LYP/6-311+G(d,p). The C-C bond that breaks upon fragmentation is indicated with the arrow.

As discussed above, the parent-to-fragment ratio of the VUV-SNMS data indicates that the ion-sputtered tryptophan molecules have a much higher average temperature of 850 K. From Equation 4.2, this temperature corresponds to 2.2 eV of internal vibrational energy. The 8.25 eV ionizing photon already puts the tryptophan cation 1 eV above its ground state; together with this 2.2 eV internal vibrational energy, the tryptophan cation has an excess of 3 eV in internal energy. Given that the dissociation limit is only 1.15 eV above the ground state, it is not surprising then that the VUV-SNMS mass spectrum of tryptophan is dominated by the methylene indole cation fragment.

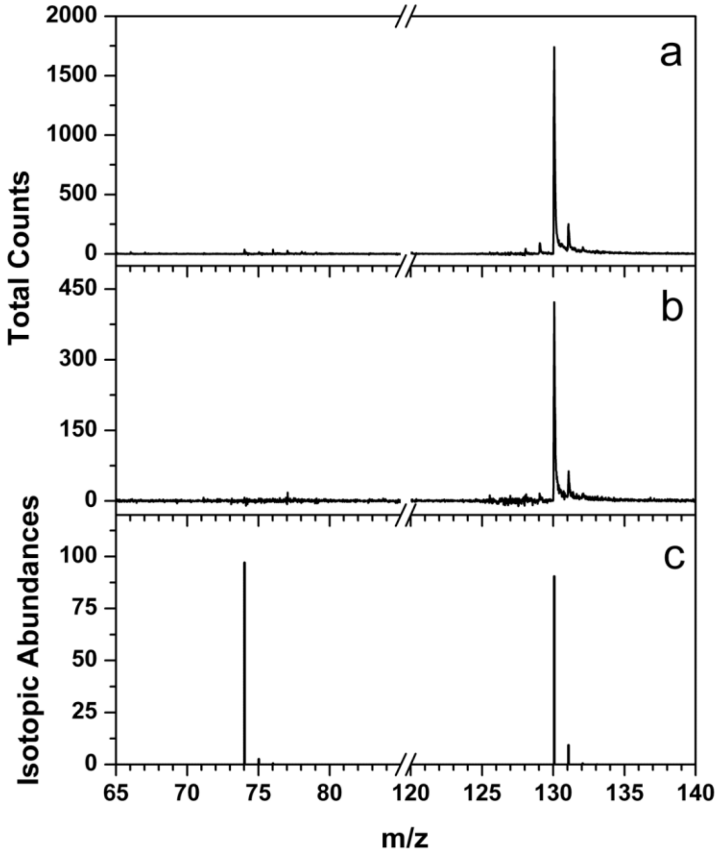

Figure 4.9 VUV-SNMS of tryptophan (50 ns of Bi_3^+, 15 scans), in the mass range of m/z = 64-82 and m/z = 122-138, acquired with photon energies of 10 eV (a) and 8 eV (b). A stick spectrum illustrating the isotopic abundances of the methylene indole and deprotonated glycine radicals are shown in panel (c) for comparison.

In order for the preceding discussion on the tryptophan energetics to be valid, the assumption that the m/z = 130 feature observed in the VUV-SNMS spectrum is the result of dissociative photoionization and not due to the photoionized neutral fragment must be validated. There are two major channels of formation for the neutral methylene indole radical—directly from the surface via the ion-sputtering process and fragmentation of metastable tryptophan molecules above the surface. In the first case, collisions involving the open-shell reactive methylene indole radicals near the surface should also lead to the formation of neutral methyl indole (m/z = 131). However, a comparison with the expected isotopic distribution of methylene indole, shown in Figure 4.9, indicates that the m/z = 131 feature is due to the heavier isotopes of

C_9H_8N and not from methyl indole (methyl indole has an ionization energy of 7.5 eV[34] and methylene indole has a calculated ionization energy of 6.2 eV). If the methylene indole radicals instead originate from fragmentation of metastable ion-sputtered tryptophan molecules, a mass spectral feature at m/z =74 should be observed as well, corresponding to the photoionized deprotonated glycine, for which the calculated ionization energy is 7.4 eV. Figures 4.9a and 4.9b show that, at both 10 eV and 8 eV photon energies, there is no major feature at m/z = 74 in the mass spectra. Therefore, the lack of any significant m/z = 74 and 131 features support the assumption that the m/z = 130 feature in the VUV-SNMS mass spectra is predominantly due to dissociative photoionization of intact neutral tryptophan molecule.

The VUV-SNMS results indicate that the intact neutral tryptophan molecules, sputtered by 25 keV Bi_3^+ primary ions, possess an internal temperature of ~850 K, which is equivalent to a vibrational energy of ~2.2 eV. Unfortunately, because the methylene indole fragment and the parent tryptophan signals differ in intensities by two orders of magnitude, the error bars on the derived 850 K internal temperature cannot be ascertained. Particularly, while the fragmentation pathway that yields the methylene indole cation can be established, it is not certain that there are no minor fragmentation pathways that would reduce the parent signal without affecting the m/z = 130 signal. Further uncertainties also arise from the poor signal-to-noise ratio of the weak tryptophan photoion signal as well as the large extrapolation of the Wilson *et al.*[32] data. Therefore, the VUV-SNMS data on thymine are examined to determine if the ion-sputtered thymine molecules also contain similar internal energies.

Dissociative photoionization of gas phase thymine has been previously studied using VUV photons.[35] It has been found that the dominant cation fragment at m/z = 55 is formed via a multi-step fragmentation pathway:[36]

$$C_5H_6N_2O_2^+ \xrightarrow{-HNCO} C_4H_5NO^+ \xrightarrow{-CO} C_3H_5N^+ \qquad (4.3)$$

Such a complex reaction pathway cannot be simply explained by comparing the energetics at the dissociation limit. Fortunately, there are experimental values to draw upon. Jochims *et al.*[35] found that the $C_4H_5NO^+$ cation at m/z = 83, although very weak, does have an appearance energy of 10.7 eV, which is 1.9 eV above their experimentally observed ionization onset of thymine at 8.8 eV. The dominant cation fragment, $C_3H_5N^+$ at m/z = 55, has an appearance energy of 11.7 eV, 2.9 eV above the thymine ionization energy. In Figure 4.3b, a peak can be seen emerging at m/z = 55 in the VUV-SNMS mass spectrum acquired with 9.5 eV photon energy. Given the ionization energy of thymine, this result would imply that the 25 keV Bi_3^+ ion-sputtered thymine has an internal energy of 2.4 ± 0.3 eV; the large error bar is because of the uncertainty in the onset of the fragment feature due to SIMS background in that spectral region. For thymine, this internal energy corresponds to a vibrational temperature of ~1300 K, derived using Equation 4.2, which is significantly higher than the tryptophan vibrational temperature. This indicates that the ion-sputtered tryptophan and thymine share a similar internal energy of ~2.5 eV, rather than a similar internal temperature. These values are quite different than the internal energies and temperatures that have been obtained for the metals systems as discussed earlier, and given that thymine and tryptophan have different functional groups, number of atoms and number of vibrations, the fact that these two molecules share a similar internal energy may be a reflection on the nature of the ion-sputtering process on organic surfaces.

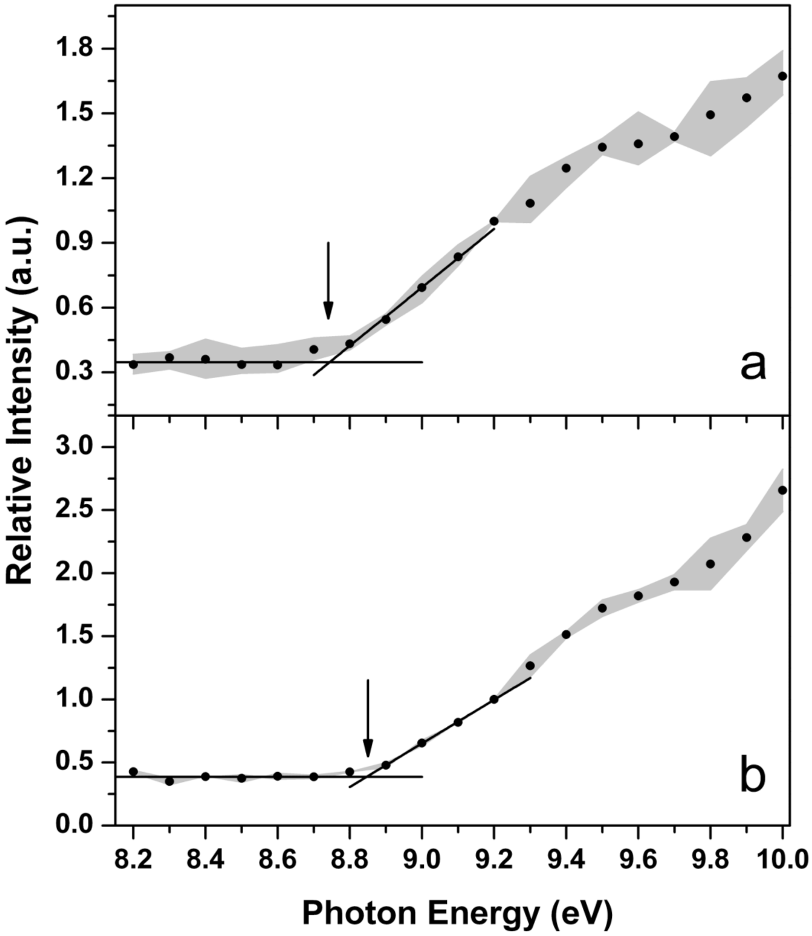

Figure 4.10 Averaged PIE curves of thymine acquired via (a) VUV-SNMS and (b) thermal desorption, a total of four scans and two scans are used for the average, respectively. For each average, the individual PIE curves are normalized to each other at 9.2 eV, and total maximum changes between individual scans are shown via the grey shading. The experimental onsets, 8.74 eV for VUV-SNMS and 8.85 eV for thermal desorption, are indicated by the arrows. The same sample is used for both experiments.

Figure 4.3 shows that the dominant feature in the VUV-SNMS of thymine is the parent signal, from which, PIE curves for the ion-sputtered thymine molecules can be obtained. The average of four VUV-SNMS PIE curves of thymine, normalized to each other at 9.2 eV, is shown in Figure 4.10a, where the grey shading indicates fluctuations in the four individual scans. For comparison purposes, shown in Figure 4.10b is the average of two PIE curves also acquired with the ToF.SIMS V instrument, utilizing the heating/cooling stage to thermally vaporize thymine samples for VUV photoionization. The difference between Figures 4.10a and 4.10b lies only in the method of desorption, 25 keV Bi_3^+ ions vs. 40 °C thermal desorption. While the VUV-SNMS PIE curves are noisier than the thermal desorption PIE curves, it is nonetheless evident that there is no significant shift in the ionization onset between Figures 4.10a and 4.10b. The ion-sputtered thymine molecules have an internal energy of ~2.5 eV, corresponding to ~1300 K in vibrational temperature, while the thermal desorption is performed at 40 °C. The difference in the ionization onset between the two averaged PIE curves is only 0.1 eV, which is within the energy resolution of the VUV light.

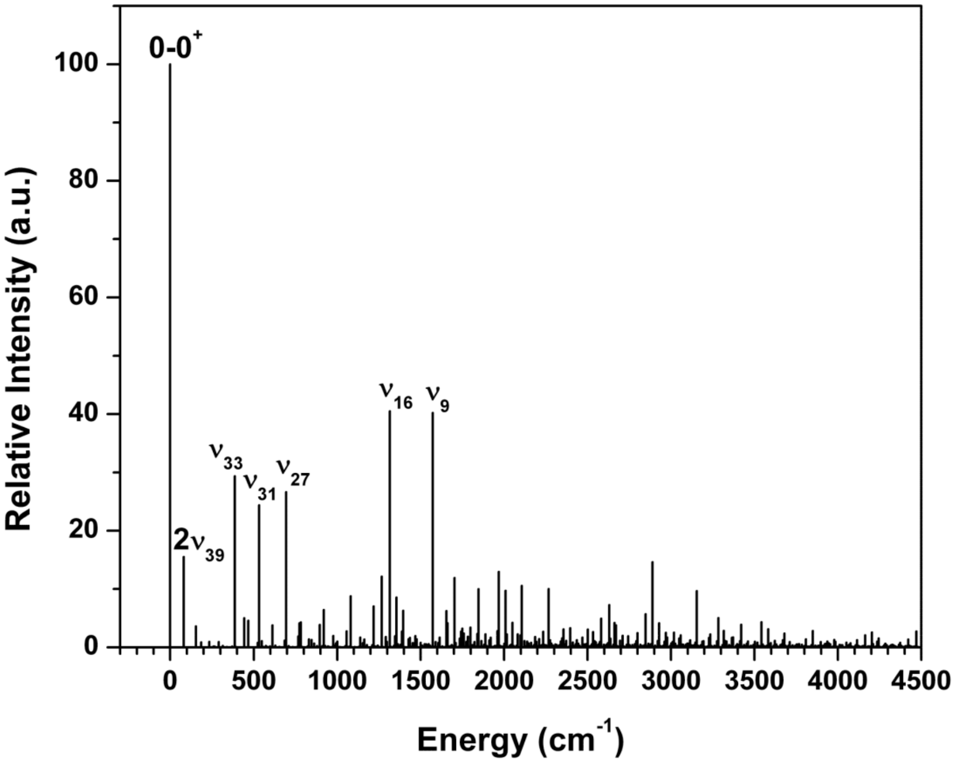

Figure 4.11 Simulated photoelectron spectrum (see computational details section) of thymine. The 0-0^+ transition is set at 0 cm^{-1}, and some major transitions are indicated (the vibrations are numbered in accordance to their frequencies in the cation). The calculated Franck-Condon overlap shows that the origin is the dominant transition in the photoionization of thymine between the two ground electronic states.

This similarity can be understood from the computed photoelectron spectrum of thymine at 0 K, shown in Figure 4.11. The Franck-Condon simulation indicates that neutral thymine does not have a large geometry change upon ionization, resulting in the 0-0^+ origin transition being the dominant feature in the simulated photoelectron spectrum. Therefore, even if there is extensive vibrational excitation, the dominant transitions upon ionization would be the sequence bands. Any changes in the ionization onset would mostly be due to differences in the vibrational frequencies and anharmonicity effects, which would not result in drastic shifts in the onset. Although it would be possible to carry out a simulation of the experimental PIE curves of thymine, the numerous vibrational modes present make such a simulation beyond the scope of the present study.

Recently, Garrison *et al.*[13] performed molecular dynamics simulations of 20 keV C_{60}^+ bombardment of an octane surface. They found that the sputtered molecules vary in internal energy by their distance away from the primary ion impact site, and the molecules with higher internal energies appear to leave the surface first with higher kinetic energy. In terms of our experiment, the double pulse extraction scheme may cause the results to be biased toward the lower internal energy population. Nonetheless, the results from the current study provide a good guide for future endeavors in SNMS studies. For example, the observed ~2.5 eV internal energy explains why SNMS methods have worked well for polyaromatic hydrocarbons where the pi-conjugated bonding system stabilizes the molecules from fragmentation. It also explains why, for molecules whose fragmentation pathways involve single bond breakage, which is the case for many amino acids, it is often the characteristic fragments that are observed in the resulting mass spectrum. For the larger long chain hydrocarbons, where both SIMS and SNMS experiments have not fared well, this internal energy is something that has to be minimized in some way before meaningful results can be obtained. With this ability to examine systematically the internal energy of the ion-sputtered molecules, VUV-SNMS can aid in the further refinement of desorption techniques while at the same time provide complementary and quantitative information and is a valuable new tool in imaging mass spectrometry.

4.5 Conclusions

VUV-SNMS studies over organic surfaces have been carried out at the Chemical Dynamics Beamline. The resulting mass spectra show that while the intensity level of the VUV-SNMS signal is lower than the corresponding SIMS signal, the mass spectra are significantly simpler. The relatively low VUV-SNMS signal is a direct result of the limited flux of the quasi-cw (500 MHz) synchrotron source, coupled with the fact that majority of the photons are not used as the instrument operates at 1-10 kHz repetition rate; this highlights the need for a higher peak power next generation light source.[37,38] Analysis shows that the organic samples have a neutral desorption yield of ~80 thymine molecules sputtered per incident Bi_3^+ and ~400 tryptophan molecules sputtered per incident Bi_3^+. A detailed examination of the observed energetics of tryptophan and thymine indicates that the ion-sputtered neutral molecules have ~2.5 eV internal energy. While this internal energy can shift the appearance energy of the fragments from dissociative photoionization, it may not necessarily change the characteristic PIE curves of the molecules, depending on the Franck-Condon window for photoionization. This means that for certain chemical species, excessive internal energy in the neutral molecules may result in dissociative photoionization at the minimal photon energy needed for ionization. Nonetheless, by controlling the amount of energy imparted to the ion-sputtered molecules in the ionization step, it should be possible to minimize fragmentation even though completely elimination of fragmentation may not be possible in certain cases. This would lead to much simpler mass spectra that are easier to assign, which is the first step towards successful wide application of imaging mass spectroscopy on heterogeneous organic systems such urban aerosols and lignocellulosic systems.

References

(1) Heeren, R. M. A.; Smith, D. F.; Stauber, J.; Kukrer-Kaletas, B.; MacAleese, L. *J. Am. Soc. Mass Spectrom.* **2009**, *20*, 1006.

(2) Vickerman, J. C. *Surf. Sci.* **2009**, *603*, 1926.

(3) Kraft, M. L.; Weber, P. K.; Longo, M. L.; Hutcheon, I. D.; Boxer, S. G. *Science* **2006**, *313*, 1948.

(4) Lechene, C. P.; Luyten, Y.; McMahon, G.; Distel, D. L. *Science* **2007**, *317*, 1563.

(5) Kollmer, F.; Bourdos, N.; Kamischke, R.; Benninghoven, A. *Appl. Surf. Sci.* **2003**, *203*, 238.

(6) Mollers, R.; Terhorst, M.; Niehuis, E.; Benninghoven, A. *Org. Mass Spectrom.* **1992**, *27*, 1393.

(7) Muller, U.; Schittenhelm, M.; Schmittgens, R.; Helm, H. *Surf. Interface Anal.* **1999**, *27*, 904.

(8) Terhorst, M.; Mollers, R.; Niehuis, E.; Benninghoven, A. *Surf. Interface Anal.* **1992**, *18*, 824.

(9) Willingham, D.; Kucher, A.; Winograd, N. *Chem. Phys. Lett.* **2009**, *468*, 264.

(10) Willey, K. F.; Vorsa, V.; Braun, R. M.; Winograd, N. *Rapid Commun. Mass Spectrom.* **1998**, *12*, 1253.

(11) Wucher, A. *Phys. Rev. B* **1994**, *49*, 2012.

(12) Wucher, A.; Staudt, C.; Neukermans, S.; Janssens, E.; Vanhoutte, F.; Vandeweert, E.; Silverans, R. E.; Lievens, P. *New J. Phys.* **2008**, *10*, 103007.

(13) Garrison, B. J.; Postawa, Z.; Ryan, K. E.; Vickerman, J. C.; Webb, R. P.; Winograd, N. *Anal. Chem.* **2009**, *81*, 2260.

(14) Takahashi, L. K.; Zhou, J.; Wilson, K. R.; Leone, S. R.; Ahmed, M. *J. Phys. Chem. A* **2009**, *113*, 4035.

(15) Hanley, L.; Zimmermann, R. *Anal. Chem.* **2009**, *81*, 4174.

(16) Hoogerbrugge, R.; Bobeldijk, M.; Kistemaker, P. G.; Los, J. *J. Chem. Phys.* **1988**, *88*, 5314.

(17) Heimann, P. A.; Koike, M.; Hsu, C. W.; Blank, D.; Yang, X. M.; Suits, A. G.; Lee, Y. T.; Evans, M.; Ng, C. Y.; Flaim, C.; Padmore, H. A. *Rev. Sci. Instrum.* **1997**, *68*, 1945.

(18) Byrd, J. M. *Nucl. Instrum. Methods Phys. Res. Sect. A-Accel. Spectrom. Dect. Assoc. Equip.* **1999**, *427*, 614.

(19) Frisch, M. J.; Trucks, G. W.; Schlegel, H. B.; Scuseria, G. E.; Robb, M. A.; Cheeseman, J. R.; J. A. Montgomery, J.; Vreven, T.; Kudin, K. N.; Burant, J. C.; Millam, J. M.; Iyengar, S. S.; Tomasi, J.; Barone, V.; Mennucci, B.; Cossi, M.; Scalmani, G.; Rega, N.; Petersson, G. A.; Nakatsuji, H.; Hada, M.; Ehara, M.; Toyota, K.; Fukuda, R.; Hasegawa, J.; M. Ishida, T. N., Y. Honda, O. Kitao, H. Nakai, M. Klene, X. Li, J. E. Knox, H. P. Hratchian, J. B. Cross, V. Bakken, C. Adamo, J. Jaramillo, R. Gomperts, R. E. Stratmann, O. Yazyev, A. J. Austin, R. Cammi, C. Pomelli, J. W. Ochterski, P. Y. Ayala, K. Morokuma, G. A. Voth, P. Salvador, J. J. Dannenberg, V. G. Zakrzewski, S. Dapprich, A. D. Daniels, M. C. Strain, O. Farkas, D. K. Malick, A. D. Rabuck, K. Raghavachari, J. B. Foresman, J. V. Ortiz, Q. Cui, A. G. Baboul, S. Clifford, J. Cioslowski, B. B. Stefanov, G. Liu, A. Liashenko, P. Piskorz, I. Komaromi, R. L. Martin, D. J. Fox, T. Keith, M. A. Al-Laham, C. Y. Peng, A. Nanayakkara, M.

Challacombe, P. M. W. Gill, B. Johnson, W. Chen, M. W. Wong, C. Gonzalez, and J. A. Pople *GAUSSIAN 03*; Gaussian, Inc.: Wallingford CT, 2004.

(20) Ervin, K. M.; Ramond, T. M.; Davico, G. E.; Schwartz, R. L.; Casey, S. M.; Lineberger, W. C. *J. Phys. Chem. A* **2001**, *105*, 10822.

(21) Ervin, K. M. *Fortran PESCAL* **2004**.

(22) Metz, R. B. Ph. D. Thesis, University of California, Berkeley, 1991.

(23) http://www.webbook.nist.gov/chemistry.

(24) Lombardi, J. R.; Davis, B. *Chem. Rev.* **2002**, *102*, 2431.

(25) Schuchardt, K. L.; Didier, B. T.; Elsethagen, T.; Sun, L. S.; Gurumoorthi, V.; Chase, J.; Li, J.; Windus, T. L. *J. Chem. Inf. Model.* **2007**, *47*, 1045.

(26) Choi, K. W.; Lee, J. H.; Kim, S. K. *J. Am. Chem. Soc.* **2005**, *127*, 15674.

(27) Zhou, Z.; Xie, M.; Wang, Z.; Qi, F. *Rapid Commun. Mass Spectrom.* **2009**, *23*, 3994.

(28) Solomko, V.; Delcorte, A.; Garrison, B. J.; Bertrand, P. *Appl. Surf. Sci.* **2004**, *231*, 48.

(29) MacLennan, M. S.; Sutherland, K. N.; Orlova, G. *J. Mol. Struct. THEOCHEM* **2007**, *822*, 21.

(30) Cheeseman, M. A.; Eyler, J. R. *J. Phys. Chem.* **1992**, *96*, 1082.

(31) Yoo, R. K.; Ruscic, B.; Berkowitz, J. *J. Chem. Phys.* **1992**, *96*, 6696.

(32) Wilson, K. R.; Jimenez-Cruz, M.; Nicolas, C.; Belau, L.; Leone, S. R.; Ahmed, M. *J. Phys. Chem. A* **2006**, *110*, 2106.

(33) Campbell, S.; Beauchamp, J. L.; Rempe, M.; Lichtenberger, D. L. *Int. J. Mass Spec. Ion Proc.* **1992**, *117*, 83.

(34) Hager, J. W.; Wallace, S. C. *Anal. Chem.* **1988**, *60*, 5.

(35) Jochims, H. W.; Schwell, M.; Baumgartel, H.; Leach, S. *Chem. Phys.* **2005**, *314*, 263.

(36) Improta, R.; Scalmani, G.; Barone, V. *Int. J. Mass. Spectrom.* **2000**, *201*, 321.

(37) Khan, S. *J. Mod. Opt.* **2008**, *55*, 3469.

(38) http://newscenter.lbl.gov/feature-stories/2009/12/21/accelerators-tomorrow-part1/.

Chapter 5

VUV-SNMS and Molecular Beams Study of Internal Energy and Fragmentation in Ion-Sputtered Monolignols

Adapted with permission from Journal of Physical Chemistry A, 2011, 115 pp 3279-3290.

The fragmentation mechanisms of monolignols under various energetic processes are studied with jet-cooled thermal desorption molecular beam (TDMB) mass spectrometry (MS), 25 keV Bi_3^+ secondary ion MS (SIMS), synchrotron vacuum-ultraviolet secondary neutral MS (VUV-SNMS) and theoretical methods. Experimental and calculated appearance energies of fragments observed in TDMB MS indicate that the coniferyl alcohol photoionization mass spectra contain the molecular parent and several dissociative photoionization products. Similar results obtained for sinapyl alcohol are also discussed briefly. Ionization energies of 7.60 eV ± 0.05 eV for coniferyl alcohol and <7.4 eV for both sinapyl and dihydrosinapyl alcohols are determined. The positive ion SIMS spectrum of coniferyl alcohol shares few characteristic peaks (m/z = 137 and 151) with the TDMB mass spectra, shows extensive fragmentation, and does not exhibit clear molecular parent signals. VUV-SNMS spectra, on the other hand, are dominated by the parent ion and main fragments also present in the TDMB spectra. Molecular fragmentation in VUV-SNMS spectra can be reduced by increasing the extraction delay time. Some features resembling the SIMS spectra are also observed in the desorbed neutral products. The monolignol VUV-SNMS peaks shared with the TDMB mass spectra suggest that dissociative photoionization of ion-sputtered neutral molecules predominate in the VUV-SNMS mass spectra, despite the extra internal energy imparted in the initial ion impact. The potential applications of these results to imaging mass spectrometry of bio-molecules are discussed.

5.1 Introduction

Lignin is the second most abundant, naturally occurring biopolymer on Earth. Its close association with cellulose in plant cell walls contributes to plants' structural integrity and resistance to pathogens.[1] While these qualities are valuable for plant survival and thereby make studies of lignocellulosic systems fundamentally important, lignin also has broad economic significance. It is a major hindrance in the production of pulp for paper[2] and, more recently, to the rapid conversion of plant materials into monomer sugars and alcohol biofuels.[3] For these reasons, lignin and lignocellulosic materials are active fields of research.[3-5]

Many techniques have been implemented to analyze the chemical makeup of biomass.[6] In particular, a number of mass spectrometry (MS) methods have been used to study lignin, [7] including pyrolysis gas chromatography MS and pyrolysis MS,[8] both of which utilize electron ionization (EI). Single photon ionization time-of-flight MS has also been applied recently to biomass studies,[9] simplifying the mass spectral signatures of lignin degradation products by depositing less energy into the analyte mixture.

The simplification of mass spectral signatures is also desirable in studies involving chemical imaging of lignin within biomass. In secondary ion MS (SIMS) analyses of wood,[10] the characteristic fragments from guaiacyl and syringyl lignin[11,12] have been used to map the chemical composition of wood in its native state. While SIMS is desirable due to its high spatial resolution, its molecular specificity, and the minimal sample preparation required, SIMS spectra of chemically heterogeneous systems are notoriously complicated, and secondary ion signals are often strongly affected by the local chemical environment.[13] SIMS images are therefore non-quantitative and difficult to interpret. It would be advantageous to minimize fragmentation observed with SIMS.

Secondary neutral MS (SNMS) is an alternative to SIMS, and it has been shown to give more quantitative results since the desorption yield of neutrals is less susceptible to the local chemical environment.[13] In SNMS the desorbed neutral analyte molecules must be ionized before analysis. EI has been used for many decades to ionize gas-phase neutrals; however it is often a "hard" ionization technique that can heavily fragment fragile organic molecules found in biological systems.[14] Postionization with laser systems has also been explored,[15,16] but organic molecules ionize in a photon energy region where tunable radiation is difficult to obtain. Multiphoton ionization techniques have been used,[17] but considerable molecular fragmentation results from the excessive energy imparted during the ionization process.

Recently, femtosecond mid-IR lasers have been applied to ionize organic molecules sputtered by 40 keV C_{60}^{+}.[18] It was found that the sensitivity for the molecular parent ions of various molecules could be improved using tunnel ionization with high peak power, long-wavelength laser fields. Ionization with longer-wavelength, 1450 nm laser radiation was found to greatly reduce molecular fragmentation compared to ionization with 800 nm laser radiation.

An alternative to the aforementioned ionization methods is single-photon, near-threshold ionization using wavelength-tunable synchrotron vacuum-ultraviolet (VUV) radiation. This method has been shown to ionize gas-phase organic molecules with minimal fragmentation[19] as well as provide quantitative information on molecular energies. In some cases, synchrotron VUV has aided in the identification of compounds on the basis of their ionization energies (IEs).[20] Single photon ionization has also been used to monitor lignin decomposition products with varying temperature.[9,21] Recently, VUV threshold ionization has been applied to study ion-sputtered neutral inorganic clusters and organic molecules in VUV-SNMS, where it has been shown to simplify mass spectra[22] and provide information on the internal energies of ion-sputtered neutrals.[23]

In this chapter, threshold single photon ionization is applied to study the photoionization of coniferyl alcohol and sinapyl alcohol, two monomer units of lignin (Figure 5.1).[24] The monolignols are introduced into a thermal desorption molecular beam (TDMB) to study the energetics and fragmentation pathways of cold monolignol molecules. Mass spectra of coniferyl and sinapyl alcohol ionized at various near-threshold energies are presented, and fragment appearance energies (AEs) are used together with theoretical values to evaluate the fragmentation mechanisms. TDMB mass spectra of coniferyl alcohol are compared to the corresponding SIMS and VUV-SNMS spectra in detail, and sinapyl alcohol is also briefly discussed. The origins of fragments in the VUV-SNMS spectra are discussed to evaluate the application of near-threshold ionization techniques to ion-probe MS imaging studies of lignin.

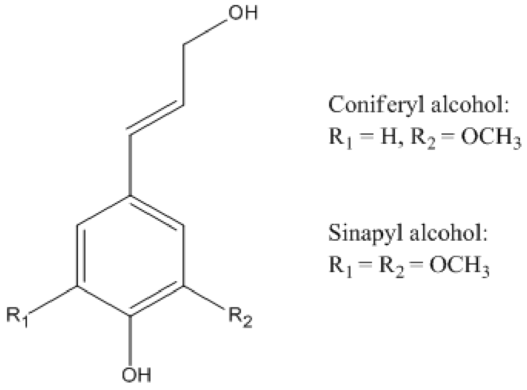

Figure 5.1: The molecular structures of coniferyl and sinapyl alcohol.

5.2 Experimental Methods

Coniferyl and sinapyl alcohol mass spectra are collected using three methods. In TDMB mass spectra, monolignols are introduced into the gas phase by thermally desorbing and cooling them in a supersonic expansion. These low-internal energy gas phase molecules are ionized with wavelength-tunable VUV photons to gain intuition for dissociative photoionization pathways. The TDMB spectra are compared to positive ion SIMS and VUV-SNMS mass spectra collected using a 25 keV Bi_3^+ ion probe for desorption. SIMS mass spectra probe the secondary cations that are sputtered and ionized with the primary Bi_3^+ ion impact. In VUV-SNMS, high-internal-energy neutrals sputtered by the Bi_3^+ ion beam are probed by VUV photoionization. VUV-SNMS is compared to TDMB and SIMS mass spectra to distinguish between the fragmentation induced by the primary ion and the ionizing photon.

5.2.1 Thermal Desorption Molecular Beams (TDMB) with VUV Photoionization

Analysis of thermally vaporized monolignols in a molecular beam is performed in a home-built reflectron-type mass spectrometer that has been previously used in photoionization studies of laser ablated species.[25] The instrument is adapted for the photoionization of monolignols by using a thermally heated nozzle described in detail in a previous study of hydrated DNA bases.[26]

Very briefly, ~50 mg of solid coniferyl alcohol (98% purity, Alfa Aesar and Sigma Aldrich) or sinapyl alcohol (80% purity, Sigma Aldrich) are introduced, without further purification, directly into a stainless steel cylindrical nozzle with a 100 μm-diameter aperture. The tip of the nozzle, where the compound is introduced, is heated with a cartridge heater, and the thermally vaporized monolignols are carried by 145 Torr (19.3 kPa) of argon into the source chamber. A 2 mm-diameter skimmer separates the source chamber from the photoionization region. The ionized molecules are extracted into a perpendicularly configured reflectron-type time-of-flight mass spectrometer where they are ionized with the VUV beam of the synchrotron, and the mass spectrum is recorded using software written with LabVIEW. The nozzle is cleaned between compounds by thoroughly rinsing with methanol, ethanol, and acetone. Although there is no direct measure of the temperature of the molecular beam, the experimental conditions in the TDMB experiments are similar to the 150 μm diameter nozzle and 175 Torr (23.3 kPa) Ar backing pressure used by Amirav et al.,[27] who suggest temperatures of ≈7 K for rotations and <50 K for vibrations for molecules with similar molecular weights.

The ionizing VUV radiation is provided by the 10-cm period undulator of the Chemical Dynamics Beamline at the Advanced Light Source, Lawrence Berkeley National Laboratory. The radiation is quasi-continuous (70 ps pulses at 500 MHz).[28] The synchrotron was recently upgraded to operate in top-off mode,[29] increasing the photon flux available to each beamline. Higher harmonic radiation is filtered by passing the radiation through a gas filter. Argon or krypton gas is used in the filter, depending on the spectral energy range that is being examined. The resulting synchrotron radiation is reflected from a 3-meter monochromator with a 1 mm-horizontal exit slit. The monochromatized light reaches the ionization region with a spectral resolution of ~50 meV and a flux of ~10^{14} photons per second.[30]

In some of the TDMB mass spectra presented below, argon ions are observed below the threshold photon energy for their ionization. This has been observed before in other experiments at the beamline, and it is attributed to either the formation of metastable argon by the synchrotron light and subsequent ionization by the residual higher harmonic radiation that passes the gas filter[31] or by direct ionization by the same residual higher harmonic radiation.

The nozzle temperature is increased while monitoring the monolignol signal at 11 eV photon energy until a satisfactory signal level is obtained for the collection of photoionization efficiency (PIE) curves for the parent molecules. Several datasets are taken as the photon energy is scanned, either in 0.2 eV steps for coarse scans over a large photon energy range or 0.05 eV steps for fine scans over smaller energy ranges. Mass spectra from $3x10^5$ time-of-flight cycles are summed for each photon energy data point. Photon flux curves for normalization of collected PIE curves are determined using a NIST-calibrated photodiode (SXUV-100, International Radiation Detectors) attached near the light exit port.

5.2.2 Secondary Ion and VUV-Secondary Neutral Mass Spectrometry (SIMS / VUV-SNMS)

A modified commercial reflectron-type time-of-flight secondary ion mass spectrometer (TOF.SIMS V; IonTOF, Germany) is coupled to a non-monochromatized synchrotron VUV light port on the same beamline. Mass-selected Bi_3^+ ions with 25 keV kinetic energy impact the sample surface at 45°, ejecting cationic, anionic, and neutral chemical species. Unless otherwise noted, SIMS spectra are acquired with 12.5 ns Bi_3^+ pulses over an area of 150 μm x 150 μm, with a 64 pixel x 64 pixel raster scan at a repetition rate of 10 kHz, and secondary ions are extracted with a 10 μs long, -2000 V pulse.

The VUV-SNMS analysis of the monolignol samples is performed using the TOF.SIMS V instrument over the same sample location as the SIMS analysis, with the same 64 pixel x 64 pixel raster scan. Due to the limited photon flux used for photoionization, VUV-SNMS signals are significantly weaker than the corresponding SIMS signals, so the spectra of the photoionized neutrals are collected using longer pulses of Bi_3^+ that span 50 ns. Datasets used for the VUV-SNMS PIE curves presented below are collected over the same location on the sample.

For the VUV-SNMS mass spectra, a previously-described double pulsing ion-extraction scheme[22] is used with a repetition rate of 2500 Hz to minimize surface charging effects and to suppress secondary ion signals. Unless otherwise noted, the majority of prompt secondary ions are extracted by the first -2000 V pulse, of 1.15 μs duration, the end of which coincides (within ~0.1 μs) with the surface impact of the last of the primary ions (50 ns primary ion pulse width). Most of the sputtered neutrals have not yet interacted with the VUV beam during the application of the first extraction pulse. These neutrals are photoionized in the extraction region for 0.55 μs while the extraction potential is zero, until the second -2000 V extraction pulse of 5 μs duration is applied.

Despite the suppression of the SIMS ions under these extraction conditions, some secondary ions are still transmitted through the analyzer, necessitating the collection of three datasets: the synchrotron-only background, the residual SIMS background, and the total signals resulting from both the synchrotron and the Bi_3^+ ion beam together. The VUV-SNMS spectra presented in this chapter are the result of the subtraction of both the synchrotron-only background and residual SIMS background from the total signal. Analyzer conditions for VUV-SNMS spectra (including the background scans) are optimized for the detection of photoionized neutrals, and no electrons are used to neutralize the surface, as sample charging is not observed.

The VUV spectral resolution at the beamline port used for VUV-SNMS is determined to be 0.2 eV by measuring the full width at half maximum of the autoionizing resonance of ion-sputtered silicon atoms at 9.8 eV.[22] Argon is used in the gas filter for all VUV-SNMS experiments, and a 100 μm horizontal slit in the gas filter is used to narrow the vertical height of the VUV beam. The resultant beam delivers ~10^{15} photons/s with a spot size of approximately 200 μm (vertical) × 600 μm (horizontal) to the photoionization interaction region. As in the TDMB experiments, VUV-SNMS PIE curves are normalized using photon flux curves determined using a NIST-calibrated photodiode.

Samples analyzed by SIMS and VUV-SNMS are prepared on silicon substrates (Wafer World, Inc.; P/N 1183) by directly depositing the monolignols onto the silicon and subsequently dissolving and dispersing the applied compound with high-purity (99.9%) methanol. Samples are allowed to air-dry. After the samples are introduced into the main chamber, they are cooled to -20 °C to suppress background signals from the photoionization of thermally evaporating monolignols. For this purpose, a heating-cooling (H/C) stage that is thermally coupled to a reservoir of liquid nitrogen is used. A thermocouple is placed under the silicon substrate to monitor the sample temperature, and the temperature is maintained at -20 °C by the SurfaceLab

6.1 software. Modified sample clamps are used with the H/C stage to permit the VUV light to pass as close as possible over the sample surface.

5.2.3 Calculations of Energetics

Calculations are performed to estimate the IEs and fragment AEs for comparison to experiment. Geometry optimization and vibrational frequency calculations of the neutral and ionic species and the main fragments for coniferyl alcohol are carried out using the Gaussian 03 program[32] at the B3LYP level with the 6-311++G(2df,2pd) basis set. The approximate initial geometry for coniferyl alcohol is taken from Wei et al.[33] Adiabatic IEs, including the zero point energy (ZPE) corrections, are obtained for the coniferyl alcohol parent and the m/z = 124, 137, 151, and 152 fragments from the difference of the computed energies of the optimized cations and neutral structures. 4-ethylguaiacol is used as a benchmark molecule. The calculated and measured TDMB IEs for 4-ethylguaiacol are 7.4 eV and 7.6 eV ± 0.1 eV, respectively.

Single-point MP2 calculations are performed for coniferyl alcohol with the same 6-311++G(2df,2pd) basis set on the B3LYP-optimized structures to improve the calculated IE so that it is 0.3 eV lower than the measured TDMB IE value. ZPEs for the neutral and cation structures of coniferyl alcohol are determined at the B3LYP level with the same basis set and are included in the final calculated value of the coniferyl alcohol IE.

In order to assist in the interpretation of the experimentally observed AEs of the coniferyl alcohol fragments, the difference between the energies of the parent cation and the optimized fragments (with ZPE corrections) are used to determine the minimal energy required for fragmentation. These differences are referred to as AEs throughout this chapter. Minimal structural rearrangement is assumed when optimizing the geometry of the fragments; therefore the results are representative of local minima only. Higher-energy transition states and potential energy barriers are not considered in calculating these AEs. Due to the size of the molecules and the complexity of the potential energy surfaces, a unique identification of the transition pathways is not performed, as it is beyond the scope of this chapter.

5.3 Results and Discussion

5.3.1 TDMB Photoionization of Coniferyl Alcohol

Coniferyl alcohol is thermally desorbed at a series of nozzle temperatures (40 °C – 110 °C) and is ionized at 11 eV photon energy. Mass spectra acquired at several nozzle temperatures are shown in Figures 5.2a-5.2c. Between 40 °C and 50 °C, no signal is observed for the coniferyl alcohol parent ion at a mass-to-charge ratio (m/z) of 180 (Figure 5.2a). At ~60 °C, the signal from the parent ion appears, and lower mass peaks (m/z = 124, 137 and 152) also grow in as the parent ion signal increases with increasing nozzle temperature (Figures 5.2b-5.2c). Scans over a larger mass range at 11 eV photon energy and 110 °C yield no evidence for features in the mass region of the coniferyl alcohol dimer within a parent signal-to-baseline ratio of 90. The peak at m/z = 181 also shows the expected intensity relative to the coniferyl alcohol parent mass from isotope distributions, which illustrates the negligible presence of protonated coniferyl alcohol that would arise from the fragmentation of coniferyl alcohol clusters.

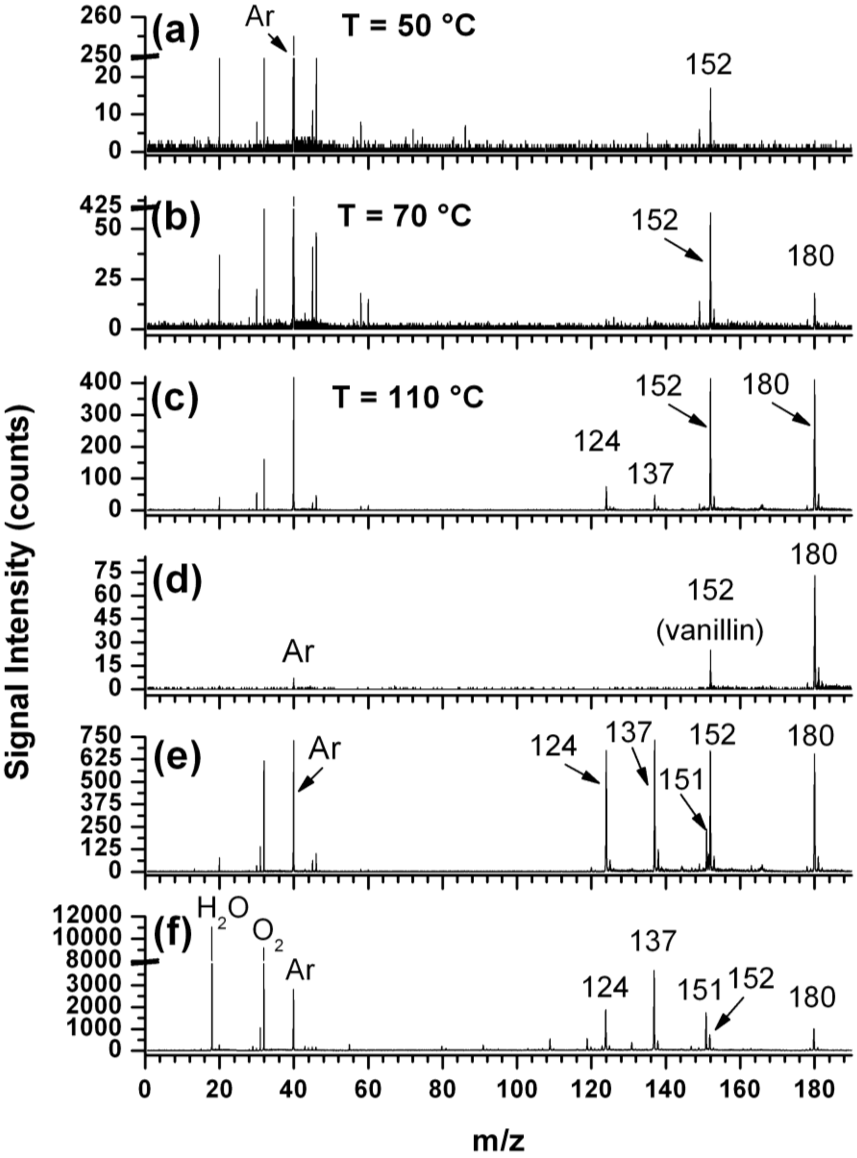

Figure 5.2: Thermal desorption molecular beam (TDMB) mass spectra of coniferyl alcohol collected with the nozzle at (a) 50 °C, (b) 70 °C and (c) 110 °C and photoionization at 11 eV. TDMB mass spectra for coniferyl alcohol at (d) 9.1 eV, (e) 12.1 eV and (f) 15.1 eV at a nozzle temperature of 110 °C.

In the lower-temperature spectra, the m/z = 152 feature is predominant. This signal decreases relative to the parent peak as the nozzle temperature is increased, and this decrease continues even when the nozzle is held at a constant temperature. This suggests that m/z =152 results from a contaminant, although it is possible that there is a small, underlying contribution to the m/z = 152 peak from the dissociative photoionization of the parent molecule. Drastic fluctuations in the intensity of m/z = 152 relative to the parent mass at m/z = 180 are observed when different bottles of coniferyl alcohol obtained from Alfa Aesar or Sigma Aldrich (all 98% purity) are used, which is indicative of accumulated degradation products from prolonged sample storage or from residual contaminants from synthesis. The m/z = 152 peak is assigned below to vanillin. Other characteristic fragments at m/z = 124 and 137 have signal intensities that exhibit constant ratios with respect to the parent peak with increasing nozzle temperature and are thus attributed to dissociative photoionization of the parent molecule.

After increasing the nozzle temperature to 110 °C to obtain workable signal counts, mass spectra are collected as a function of photon energy. Spectra of coniferyl alcohol at 9.1 eV, 12.1 eV and 15.1 eV are shown in Figures 5.2d-5.2f. The parent signal at m/z = 180 dominates below 9 eV and has a signal-to-baseline ratio of ~35, highlighting the capability of threshold single-photon ionization to obtain fragment-free mass spectra.[19,34] As the photon energy is increased, features at m/z = 124, 137, and 151 appear (Figures 5.2e-5.2f). The strongest lower m/z peaks appear at 18, 32 and 40 amu, which correspond to H_2O, O_2 and argon, respectively. The presence of argon in the mass spectrum below its IE of 15.76 eV was discussed above.

The parent molecule is a prominent peak at all photon energies examined in the TDMB experiments, although dissociative photoionization increases at higher photon energies. At 9.1 eV, the ratio of the molecular parent signal intensity to the summed intensity of the main fragments is essentially infinite (here, m/z = 124 and 137 constitute the main fragments since the transient sample contaminant dominates the contributions to m/z = 152 and 151), while at 12.1 eV and 15.1 eV, the parent-to main fragments ratio decreases to ~0.4 and ~0.2, respectively. The integrated peak intensity for coniferyl alcohol is plotted versus photon energy in Figure 5.3. By performing a linear fit to the low photon energy baseline and onset slope of the PIE curve, the IE is determined to be 7.60 eV ± 0.05 eV. This disagrees with the calculated results of ten Have *et al.*[35] who predict an IE of 8.60 eV ± 0.06 eV, but is in reasonable agreement with calculations by Wei *et al.*[33], who predict an IE of 7.26 eV, and with calculations in this work, which predict an adiabatic IE of 7.3 eV.

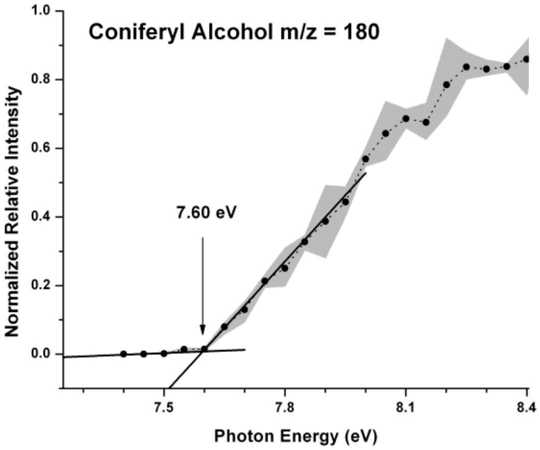

Figure 5.3: Signal intensity of coniferyl alcohol plotted versus ionizing photon energy. The extrapolation lines used for determining the AEs are in bold. Error bars are indicated by the gray shading. Adjacent data points are normalized with respect to each other with the measured photon flux curves.

Main Fragment[a] (+cofragments)		IE of Main Fragment	Theoretical AE of Main Fragment Cation	TDMB AE	VUV-SNMS AE
Coniferyl Alcohol Sample					
Coniferyl Alcohol m / z = 180		8.60 ±0.06[d]; 7.26[e]; 7.3[b]	—	7.60±0.05	8.0±0.5
m / z = 152	Structure A (+CO)	6.8[b]	8.4[b]	—	—
	4-Ethylguaiacol	7.4[b]; 7.6±0.1[c]	—	—	—
	Vanillin	8.30±0.05[f]; 8.30±0.05[c]	—	8.3±0.2	—
m / z = 151	Structure B (+CO+H)	6.6[b]	11.0[b]	—	8.3±0.5
	Vanillin – H	—	—	11.5±0.2	
Structure D m / z = 137 (+·CH_2CHO)		6.5[b]	8.9[b]	10.35±0.05	8.2±0.5
Guaiacol m / z = 124	(+propargyl alcohol)	7.95[e]; 7.7[b]	9.6[b]	10.50±0.05	8.4±0.5
	(+2-propenal)		8.2[b]		
Sinapyl Alcohol Sample					
Dihydrosinapyl Alcohol m / z = 212		—	—	<7.4	—
m / z = 168 (+C_2H_4O)		—	—	10.80±0.05	—
Sinapyl Alcohol m/z = 210		7.10[e]	—	<7.4	—
m/z = 182		—	—	10.30±0.05	—
m/z = 181		—	—	10.8±0.2	—
m/z = 167		—	—	11.6±0.2	—
m/z = 154		—	—	11.00±0.05	—

[a]Nominal mass; [b]Calculations from this work; [c]Evaluated from the TDMB PIE of the pure compound, this work; [d]Ref 35; [e]Ref33; [f]Ref36

Table 5.1: Calculated and experimental ionization energies (IEs) and appearance energies (AEs). Errors next to each experimental IE and AE are based on the spectral resolution of the light and the size of the photon energy steps between data points. AEs are calculated assuming that the co-fragments are given by the chemical structures in parentheses. "—" indicates that theoretical or experimental values are either not available or not applicable to the given situation. All calculations in this work are performed at the B3LYP level except for the IE for coniferyl alcohol, which is calculated using MP2. All energies are in eV.

The major fragments of coniferyl alcohol observed with VUV photoionization are comparable to those observed in EI spectra, and the similarities increase with increasing photon energy. Previous structural assignments for fragments from EI[37] are used to decipher the fragmentation mechanism in this experiment. IEs and AEs for the proposed structures[37] are calculated and compared to the experimentally-determined AEs and previous theoretical IE values in Table 5.1. The structures involved in the various coniferyl alcohol fragmentation mechanisms considered here, together with their sinapyl alcohol analogues, are shown in Figure 5.4. The photoionization of vanillin and 4-ethylguaiacol are also included in the figure as possible sources of the m/z = 152 contaminant.

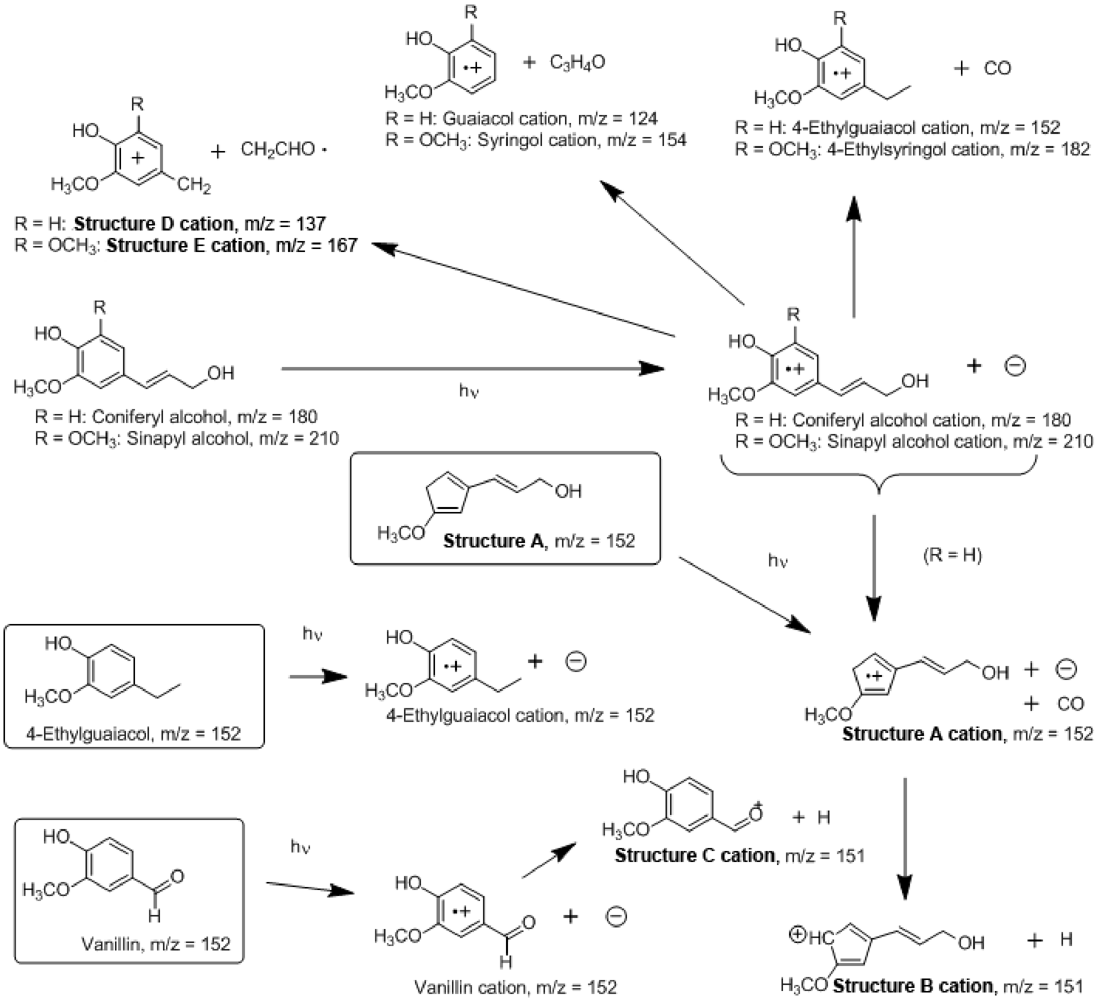

Figure 5.4: Diagram of the main fragmentation pathways examined in experiments on coniferyl alcohol (R = H). Possible contaminant or degradation products are indicated by the boxes. Sinapyl alcohol structural analogues (R = OCH_3) are also shown with their names.

In EI spectra, m/z = 152 is assigned to a five-member ring structure (Figure 5.4, Structure A cation),[37] arising from CO elimination from the ring structure. Due to the aforementioned decay of the m/z = 152 signal with respect to the parent in the TDMB experiments reported here, it is uncertain to what extent dissociative photoionization contributes to the m/z = 152 signal.

Instead, it appears that the obtained appearance curve of m/z = 152 is dominated by the ionization of a transient degradation product or contaminant.

4-ethylguaiacol, an observed thermolysis product of coniferyl alcohol,[38] and vanillin, a pyrolysis product found in dehydrogenation lignin polymers and milled wood lignin[8] are two possibilities for m/z = 152. The TDMB AE of m/z = 152 is 8.3 eV ± 0.2 eV. The IEs of neutral 4-ethylguaiacol (7.6 eV ± 0.1 eV, this work) and vanillin (8.30 eV ± 0.05 eV)[36] are included in Table 5.1 for comparison. Based on these values, vanillin is determined to be the most likely source of m/z = 152 in the TDMB spectra. TDMB experiments are performed for pure vanillin to verify this assignment, and the resulting PIE curve and IE (8.30 eV ± 0.05 eV, this work) agree with the appearance curve and AE of m/z = 152 in the coniferyl alcohol TDMB spectrum (Figure 5.5a).

In a previous EI analysis, m/z = 151 has been assigned to the cation of Structure B, a fragment of the five-member ring m/z = 152 (Structure A) cation.[37] While this structural assignment has at most a minimal contribution to the signals observed in these experiments, the concurrent decay of m/z = 151 with m/z = 152 over time indicate that m/z = 151 is related to the m/z = 152 peak. From the shape of the two appearance curves (Figure 5.5b) it can be seen that the m/z = 152 (vanillin) signal intensity plateaus after 11.8 eV, which coincides roughly with the onset of the m/z = 151 signal at 11.5 eV. This implies that m/z = 151 arises from the fragmentation and depletion of vanillin, thus making the vanillin – H cation the most likely assignment (Structure C cation). This assignment is further supported by the similar appearance curve of m/z = 151 observed in the TDMB spectra of pure vanillin (data not shown). This vanillin – H structural assignment has also been previously made for m/z = 151 in SIMS spectra.[12]

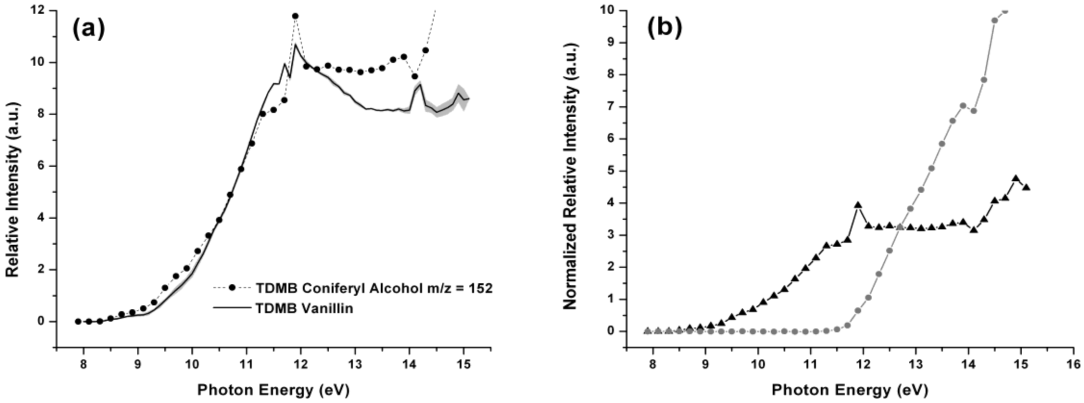

Figure 5.5: (a) Vanillin TDMB PIE (solid line) with error bars in gray and the TDMB appearance curve of m/z = 152 from the coniferyl alcohol spectrum (black circles with dashed line – larger photon energy step size). PIEs are normalized with respect to each other at 10.5 eV. Features near 12 eV and 14 eV arise from absorption lines of the argon in the gas filter. (b) Appearance curves of m/z = 151 (gray circles) and 152 (black triangles) from the coniferyl alcohol mass spectrum over a broad photon energy range. The two curves are scaled with respect to each other by an arbitrary factor for visual clarity.

The fragment at m/z = 137 has been attributed to the molecular rearrangement of the parent ion and subsequent loss of a neutral radical CH_2CHO in the EI[37] and SIMS[12] mass spectra

(Structure D cation). In the TDMB experiments, the m/z = 137 cation has an experimental AE of 10.35 eV ± 0.05 eV. The calculated IE (6.5 eV) of the optimized neutral structure for m/z = 137 is much lower than the observed AE at this mass, and there is no evidence, within the signal-to-noise, of the co-fragment at m/z = 43; hence the 137 mass fragment is attributed to dissociative photoionization of the parent molecule.

A calculated AE for the dissociative ionization that leads to the m/z 137 cation was explored theoretically. The calculated AE for the optimized m/z = 137 cation structure and its corresponding neutral radical CH_2CHO fragment is 8.9 eV. This is lower than the experimental TDMB AE, indicative of the presence of higher energy barrier(s) involved in the fragmentation, a feasible scenario given that the neutral parent molecule must undergo rearrangement of two of its hydrogen atoms before fragmentation. A detailed theoretical mapping of the dissociation pathway is outside the scope of the current work.

The fragment at m/z = 124 is assigned to the guaiacol cation, which has an experimentally-observed TDMB AE of 10.50 eV ± 0.05 eV. This AE is much higher than is expected for direct ionization of neutral guaiacol, calculated by Wei et al[33] and also in the present chapter (7.95 eV and 7.7 eV, respectively). This disparity and the absence of ion signal from the complementary neutral C_3H_4O fragment at m/z = 56 provide evidence that the observed guaiacol ion signal arises from the dissociative photoionization of coniferyl alcohol.

As was noted, the complementary neutral fragment for the guaiacol cation has a mass of 56 amu. While this mass may correspond to several different structures, propargyl alcohol and 2-propenal are considered as the two most feasible possibilities since they require the least amount of atomic rearrangement during the dissociation process. Calculation of the AE for the guaiacol cation with these two possible m/z = 56 neutral fragments shows that the propargyl alcohol is the more likely co-fragment (see Table 5.1), with a calculated AE of 9.6 eV, compared to 8.2 eV for the 2-propenal.

5.3.2 TDMB Photoionization of Sinapyl Alcohol

Sinapyl alcohol is similar to coniferyl alcohol in structure, differing only by an additional $–OCH_3$ group that replaces a hydrogen on the aromatic ring (Figure 5.1); therefore it shares many fragmentation patterns with coniferyl alcohol, resulting in similar mass peaks shifted by 30 mass units, which is the difference in mass due to the OCH_3 subgroup versus the H subgroup.

During TDMB experiments, the nozzle temperature is varied from 40 °C to 140 °C, and photoionization is observed with 11 eV photons. The parent ion (m/z = 210) appears concurrently with dihydrosinapyl alcohol (m/z = 212) and high mass fragments from both species (m/z = 154, 167, 168, 181, 182) when the nozzle temperature reaches approximately 65 °C. Similar to coniferyl alcohol, TDMB mass spectra collected over a larger mass range at 10 eV photon energy and 140 °C show no peaks in the dimer mass region within a parent signal-to-baseline ratio of 75, and the peak at m/z = 211 shows the expected intensity with respect to the m/z = 210 from natural isotopic distributions; hence fragment peaks are assumed to arise from the monomer and any contaminants within the sample, and not from clusters of sinapyl alcohol.

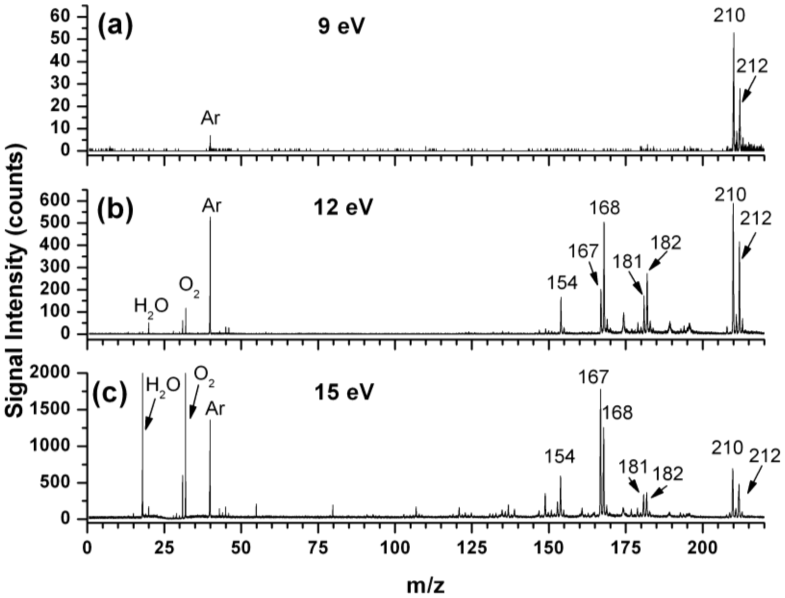

Figure 5.6: TDMB mass spectra of sinapyl alcohol at 140 °C and (a) 9 eV, (b) 12 eV and (c) 15 eV. M/z = 210 and 212 appear at approximately the same temperatures, but exhibit independent behavior with temperature.

Select spectra at different photon energies are shown in Figure 5.6. As with coniferyl alcohol, sinapyl alcohol TDMB mass spectra at low photon energies below 9 eV (Figure 5.6a) are essentially fragment free (dihydrosinapyl alcohol, a common contaminant in syntheses of sinapyl alcohol[39], and its fragments are ignored). The parent signal persists at all photon energies investigated in this study, even as dissociative photoionization becomes more dominant. At 9 eV, the ratio of the molecular parent signal intensity to the summed intensity of the main fragments is essentially infinite (here, m/z = 154, 167, and 182 constitute the definitive main fragments; m/z = 181 could not be confirmed to originate from sinapyl alcohol), while at 12 eV and 15 eV, the parent-to main fragments ratio decreases to ~0.8 and ~0.3, respectively.

The peaks at m/z = 18 and 32 (Figures 5.6b-5.6c) are assigned to H_2O and O_2; this assignment is confirmed by the observed IEs, which agree well with literature values.[40,41] The m/z = 212 peak, seen in Figures 5.6a-5.6c is attributed to the presence of unsaturated dihydrosinapyl alcohol, which is a common contaminant in syntheses of sinapyl alcohol.[39] As with coniferyl alcohol, the peak at m/z = 40 corresponds to ionization of metastable argon, and the low molecular weight co-fragments of m/z = 182, 167 and 154 (m/z = 28, 43, and 56) are notably absent even at 15 eV (Figure 5.6c). This suggests that the heavier mass fragments arise from dissociative photoionization of either sinapyl alcohol or the dihydrosinapyl alcohol contaminant.

Figure 5.7a shows the PIE of sinapyl alcohol, from which an adiabatic IE of <7.4 eV is determined. The lowest available photon energy at the beamline is 7.4 eV, however the IE can be estimated further by extrapolating the PIE curve to a zero baseline. A zero baseline is regularly achieved at the monochromatized light port on the beamline in the low photon energy range since few background gas species are ionized at these energies. Such an extrapolation yields an estimated sinapyl alcohol IE of 7.35 eV. With the lack of a measurable baseline, error bars for this value cannot exactly be determined, but it can likely be safely assumed that the IE values are correct within 0.5 eV. A similar extrapolation is used to determine the IE of dihydrosinapyl alcohol to be 7.30 eV (Figure 5.7b).

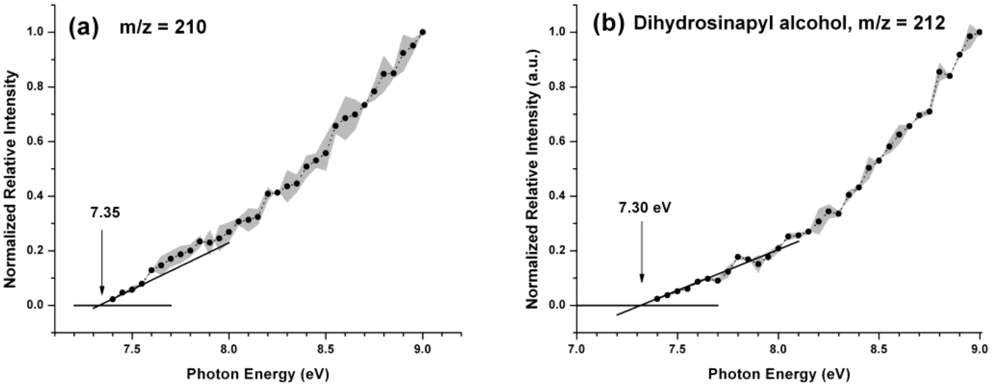

Figure 5.7: TDMB PIEs of (a) sinapyl alcohol and (b) dihydrosinapyl alcohol at a fixed nozzle temperature of 140 °C. Ionization onsets are estimated by extrapolating (bold lines) to a zero baseline.

The mass m/z = 182 is attributed to the loss of a carbon and oxygen atom, one possible resultant structure being 4-ethylsyringol. This peak increases with the sinapyl alcohol signal (m/z = 210) as the nozzle temperature is increased, consistent with a constant-fraction dissociative photoionization product of sinapyl alcohol. This correlative dependence on the parent molecule is in contrast to the distinctly different behavior of vanillin (m/z = 152) in the case of coniferyl alcohol.

Structure E (m/z = 167) appears at about 1.3 eV higher in photon energy than the corresponding m/z = 137 from coniferyl alcohol, which may be due to a higher activation energy associated with the prerequisite rearrangement of the alcohol tail in the sinapyl alcohol molecule. The m/z = 167 mass peak is also accompanied by a mass peak at m/z = 168. This latter peak is assigned to 4-methylsyringol, which likely arises from hydrogen rearrangement and loss of C_2H_4O from the non-negligible amounts of the contaminant dihydrosinapyl alcohol. This conclusion is supported by the temperature dependence of the m/z = 168 peak intensity, which varies with the signal intensity of dihydrosinapyl alcohol (data not shown).

The syringol cation is the tentative assignment of the m/z = 154 peak in the sinapyl alcohol mass spectrum. Syringol has an experimental AE of 11.00 eV ± 0.05 eV, which is about 0.5 eV higher than the AE of guaiacol (m/z = 124) from coniferyl alcohol. Syringol arises from sinapyl alcohol via the loss of the long alcohol tail and a hydrogen donation to the charged fragment.

Both coniferyl alcohol and sinapyl alcohol exhibit fragment-free TDMB photoionization mass spectra at low photon energies (*e.g.* below 9 eV) and exhibit characteristic dissociative ionization fragments at higher photon energies, although the parent masses remain clearly observable at all photon energies used. As will be seen in the next section, these same signature fragments are also observed in the VUV-SNMS mass spectra. The analysis of the TDMB experiments is therefore fully applicable for a thorough understanding of the origins of the mass spectral features in VUV-SNMS.

5.3.3 SIMS and VUV-SNMS of Coniferyl Alcohol

Secondary ion and secondary neutral mass spectra are collected from Bi_3^+ ion sputtering of coniferyl alcohol deposited onto silicon substrates. Figure 5.8 presents comprehensive mass spectral results for SIMS ions, the TDMB data taken on the other apparatus, and VUV-SNMS analyses, the latter two at two different photon energies around 9 eV and 15 eV. The SIMS data (Figure 5.8a) reproduces the main SIMS signatures published previously.[12] The m/z = 137 feature has been tentatively assigned to the cation fragment $C_8H_9O_2^+$ (Structure D), and the m/z = 151 feature has been assigned mainly to the $C_8H_7O_3^+$ fragment (Structure C).[12] Figure 5.8a illustrates the great complexity of the SIMS spectrum, compared to the TDMB spectra presented in Figures 5.8b-5.8c.

Qualitatively, the VUV-SNMS mass spectra are simpler than the corresponding SIMS spectra, although they share similar spectral features with both SIMS and TDMB mass spectra. As can be seen in Figure 5.8a, the SIMS spectrum shows only a few strong characteristic fragments at m/z = 137 and 151, along with a huge array of other masses, while the VUV-SNMS spectra (Figures 5.8d-5.8e) show clear characteristic peaks at m/z = 124, 137, 151 and 180, similar to the TDMB experiments (Figures 5.8b-5.8c). The m/z = 152 (*e.g.* vanillin) peak does not appear as a major fragment in VUV-SNMS spectra, which may be a result of the rapid energy input from the ion beam (and subsequently reduced degradation compared to the long exposure periods to high temperature in the nozzle region of the TDMB experiments).

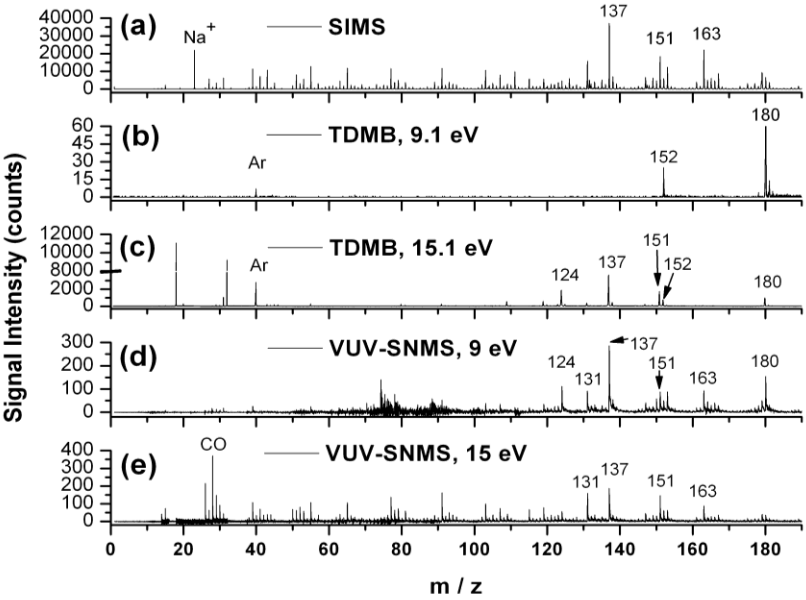

Figure 5.8: Comparison of coniferyl alcohol mass spectra obtained with (a) positive ion SIMS, TDMB at (b) 9.1 eV and (c) 15.1 eV, and VUV-SNMS at (d) 9 eV and (e) 15 eV. SIMS data is collected using 12.5 ns pulses of Bi_3^+ under analyzer conditions optimized for secondary ion detection.

The presence of several common fragments in the VUV-SNMS and TDMB experiments may be indicative of dissociative photoionization of the ion-sputtered parent molecules; however it is also likely that the VUV-SNMS spectra have contributions from other sources, including the ionization of sputtered neutral fragments or released surface reaction products. While dissociative photoionization can be minimized by reducing the photon energy used to ionize the molecules, possible gas-phase neutral fragments can lead to an unavoidable source of fragment ions, since they arise from the initial ion impact. Such mechanisms are likely responsible for the clusters of peaks in the coniferyl alcohol VUV-SNMS spectra in the regions around m/z = 150 and 165, which are also visible in the SIMS spectra, but are completely absent in the TDMB mass spectra even at 15 eV.

The prominent m/z = 28 peak in the VUV-SNMS mass spectrum at 15 eV (Figure 5.8e) is one such VUV-SNMS feature that does not arise from dissociative photoionization of the molecular parent. It is most likely due to CO and provides a simple starting point for evaluating the relative contributions of different sources of neutrals. This mass peak is not present in the TDMB experiments on coniferyl alcohol, and hence the CO cation is not believed to arise from dissociative photoionization of the coniferyl alcohol parent at the photon energies used. The observed CO also cannot be attributed to the ionization of any background gas by the synchrotron beam.

Although it is tempting to suggest that the photoionized CO may arise from neutral CO desorbed directly from the surface, there are other possible sources that must be considered. The neutral CO may be a co-fragment of a secondary fragment ion, a co-fragment of another neutral fragment, or a product of a more complex process. To partly distinguish between the many possibilities, a brief estimate is performed. The CO photoionization cross section at 14.9 eV is ~15.3 Mb (1 Mb = 1 x 10^{-18} cm^2).[42] This photoionization cross section, the observed CO signal counts in the VUV-SNMS mass spectra at 15 eV, and the synchrotron flux at 15 eV can be used to estimate the number of neutral CO molecules being desorbed using the relation:[23]

$$N \approx \frac{Z}{0.08 \cdot \sigma F \tau}, \tag{5.1}$$

where N is the number of neutral CO molecules being desorbed from the surface, Z is the number of CO ions that are observed, σ is the CO photoionization cross section at 15 eV, F is the photon flux, and τ is the time that the desorbed CO molecules take to traverse the height of the ionizing beam (approximately 0.2 μs).[23] The calculated number of desorbed CO molecules is approximately five orders of magnitude larger than the total observed secondary ion counts at the same Bi_3^+ flux. This indicates that the amount of neutral CO observed cannot arise as a complementary fragment to the m/z = 151 and 152 (or other) secondary ions formed during the desorption event. The majority of neutral CO may be produced from larger neutral fragments or may be sputtered from a chemically modified surface (among other mechanisms). Distinguishing between the remaining possible sources of neutral CO is difficult since many parameters such as the ionization cross sections for m/z = 152, 151, and other possible species involved are unknown; however from the presence of released CO it is clear that dissociative photoionization of parent molecules is not the only process contributing to VUV-SNMS signals; other complex processes complicate the VUV-SNMS mass spectra compared to TDMB mass spectra.

Despite this possible limitation on the potential simplicity of the VUV-SNMS spectra of coniferyl alcohol, the parent mass at m/z = 180 is one of the major peaks in the VUV-SNMS spectrum. This contrasts with the corresponding SIMS spectrum, where m/z = 180 is just one of a number of mass peaks near the parent mass. By scanning the ionizing photon energy in coarse steps, a rough PIE curve is obtained for the ion-sputtered parent molecules at this mass. Relatively large energy spacing between data points is used due to the rapid decay of VUV-SNMS signal from the accumulation of ion-induced chemical damage of the sample during analysis. The VUV-SNMS PIE curve for coniferyl alcohol (Figure 5.9a) has an ionization onset of 8.0 eV ± 0.5 eV, where the uncertainty corresponds to the largest step size of the three averaged VUV energy scans. Within the error bars, this AE does match the IE of coniferyl alcohol obtained in the TDMB experiments (7.60 eV ± 0.05 eV). It may be thought that the ion desorbed species would harbor considerable internal energy and thus would have a lower IE, however it has been found that additional internal energy can have minimal effect on the absorption cross section and resulting IE for a neutral parent molecule in certain cases.[34]

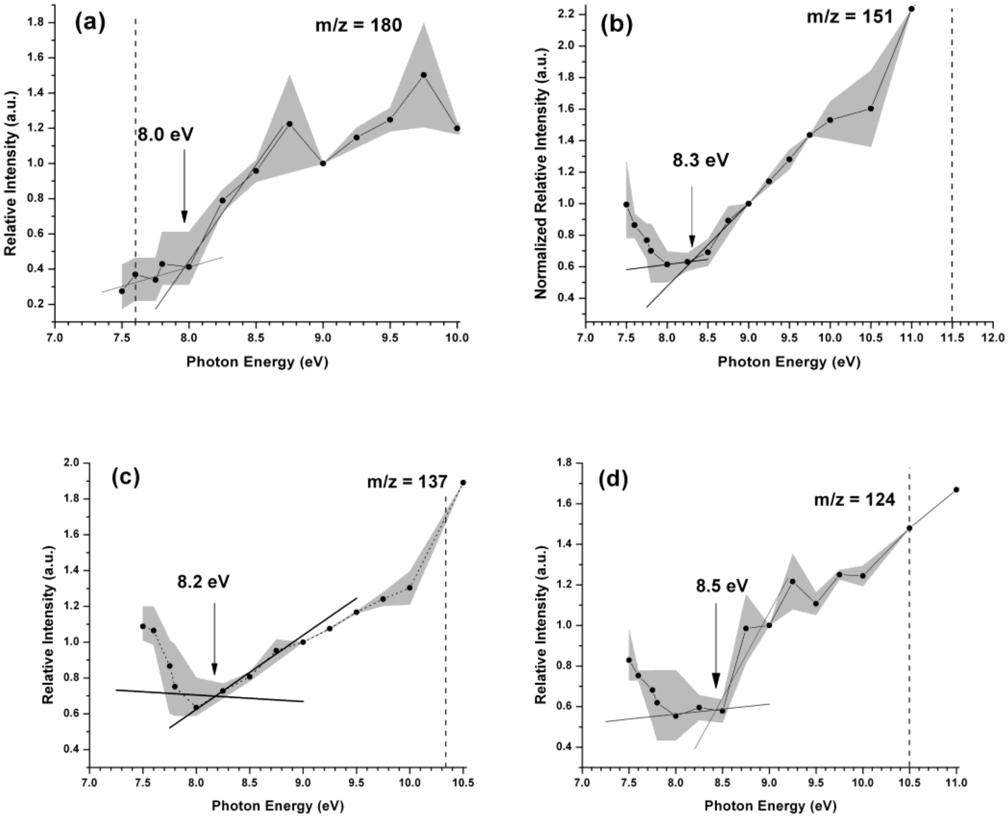

Figure 5.9: VUV-SNMS appearance curves for (a) coniferyl alcohol and the main VUV-SNMS fragments (b) m/z = 151, (c) m/z = 137 and (d) m/z = 124. The bold lines are the extrapolations, and the dashed vertical lines mark the ionization onsets observed in the TDMB experiments. Black circles represent averages of three datasets, collected at staggered photon energies and normalized with respect to each other at 9 eV. Error bars (gray shading) are determined for each point by linear interpolation of datasets. IEs are rounded to the nearest 0.1 eV.

Unlike the VUV-SNMS AE of the coniferyl alcohol parent, those of the fragments at m/z = 151 (loss of CO + H), m/z = 137 (loss of radical CH_2CHO), and m/z = 124 (guaiacol) are definitely shifted to lower photon energies compared to the TDMB experiments (see Table 5.1, Figures 5.9b-5.9d). This shift is apparent even with the relatively coarse photon energy steps, and it may be due to direct photoionization of ion-sputtered neutral fragments or the dissociative photoionization of vibrationally excited parent molecules. These two possibilities are considered below.

The m/z = 151 peak in the coniferyl alcohol VUV-SNMS spectra has an AE of 8.3 eV ± 0.5 eV (Figure 5.9b). The relatively high signal below 7.9 eV of the PIE curve is attributed to ionization from second harmonic radiation from the undulator, which passes through the argon-filled gas filter at lower photon energies. This baseline is not present in the TDMB data since krypton was used in the gas filter for those experiments. Since VUV-SNMS analysis does not expose the sample to high temperatures for prolonged periods of time and is performed with a much lower chamber pressure than in the TDMB experiments, it is possible that the m/z = 151 observed in VUV-SNMS is not derived from the same transient species observed in the TDMB experiments (previously assigned to vanillin – H).

The observed VUV-SNMS AE for the coniferyl alcohol m/z = 151 lies 1.7 eV above the calculated IE of the optimized five-member ring neutral structure (Structure B)[37] resulting from CO and H loss, and over 2 eV below either the calculated or experimental (TDMB) AEs. The differences of these values compared to the AEs predicted for dissociative photoionization can be justified by the 2 eV to 2.5 eV of internal energy that is likely deposited into the neutral molecule during the ion sputtering event[22]. This reduces the energy needed from the ionizing photon to fragment the molecule, resulting in a lower AE for the ion-sputtered fragment. By the same reasoning, the dissociative photoionization of vanillin – H may also contribute, although its TDMB AE has a larger difference of 3.5 eV with the VUV-SNMS m/z = 151 AE. 4-ethylguaiacol does not exhibit a fragment at m/z = 151 in TDMB experiments of pure 4-ethylguaiacol (data not shown), so the VUV-SNMS signal does not arise from dissociative photoionization of 4-ethylguaiacol. The direct photoionization of neutral vanillin – H (Structure C) and 4-ethylguaiacol – H are further possibilities that cannot be eliminated.

The m/z = 137 in the VUV-SNMS spectra has an AE of 8.2 eV ± 0.5 eV (Figure 5.9c), which is about 2.2 eV lower than the AE in the TDMB experiments (10.35 eV). The calculated IE of neutral m/z = 137 (Structure D) is 6.5 eV. Since the AE is much higher than the calculated IE for Structure D, the m/z = 137 signal in the VUV-SNMS spectra is attributed to the dissociative photoionization of internally excited neutral parent molecules.

Guaiacol (m/z = 124) in the VUV-SNMS spectra has an AE of 8.4 eV ± 0.5 eV (Figure 5.9d), which is over 2 eV lower than the corresponding AE observed in the TDMB experiments (10.50 eV). The lowered AE may be due to internal energy imparted to coniferyl alcohol during the sputtering event or from the direct ionization of sputtered neutral guaiacol. The VUV-SNMS AE of guaiacol cannot rule out the latter possibility because, within error bars, photoionization of ion-sputtered neutral guaiacol (theoretical IE = 7.7 eV in this work, or 7.95 eV;[33] experimental IE = 8.0 eV[36]) is consistent with the VUV-SNMS AE.

The presence of common fragments between the coniferyl alcohol VUV-SNMS mass spectra and TDMB mass spectra imply that dissociative photoionization of intact sputtered neutral coniferyl alcohol molecules are the main source of fragmentation in the VUV-SNMS mass spectra. Although more complex surface processes undoubtedly contribute to these spectra due to the high-energy primary ions involved, dissociative photoionization cannot be eliminated as an explanation for the formation of either m/z = 151 or guaiacol (m/z = 124) in the VUV-

SNMS spectra. Dissociative photoionization is also the most likely mechanism for the appearance of m/z = 137 in VUV-SNMS.

5.3.4 SIMS and VUV-SNMS of Sinapyl Alcohol

The SIMS, TDMB and VUV-SNMS spectra of sinapyl alcohol are shown in Figure 5.10. The VUV-SNMS spectra show significantly more SIMS-like character than coniferyl alcohol, as is evident by the many small peaks in the spectral baseline in Figure 5.10d. This increased neutral fragmentation may be due to the higher number of fragments possible for sinapyl alcohol due to its higher complexity and from the destabilizing effect of the additional OCH_3 group that is substituted for an H on the aromatic ring. It may also be due to the overlay of fragments from sample contaminants such as dihydrosinapyl alcohol due to the lower (80%) sample purity. Despite these complications, the sinapyl alcohol mass spectrum also exhibits the characteristic peaks observed in the TDMB photoionization experiments, including the molecular parent.

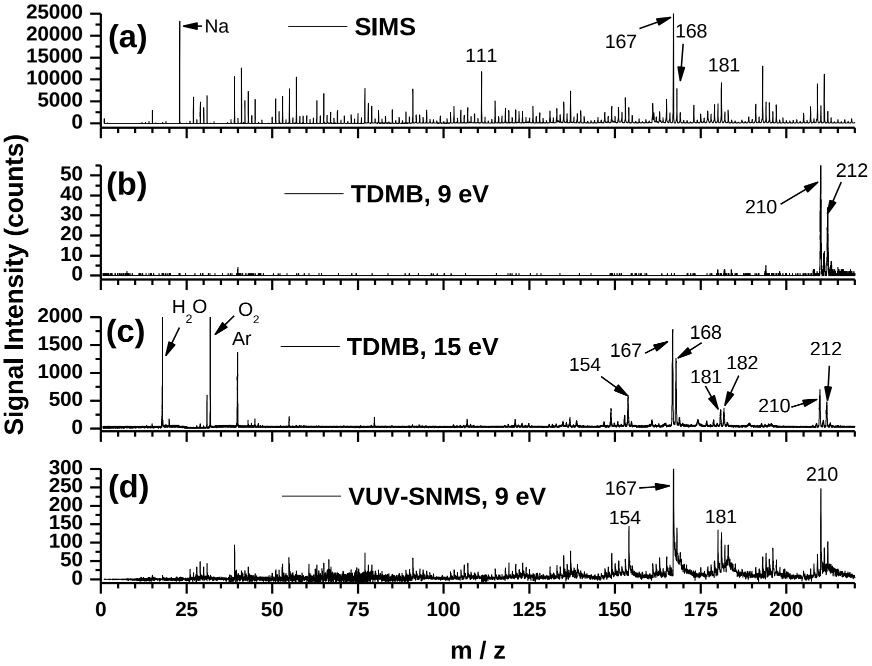

Figure 5.10: Mass spectra of sinapyl alcohol obtained using (a) positive ion SIMS, TDMB at (b) 9 eV and (c) 15 eV and (d) VUV-SNMS at 9 eV. SIMS data is collected using 12.5 ns of Bi_3^+ under analyzer conditions optimized for secondary ion detection. VUV-SNMS is obtained after the subtraction of background synchrotron and SIMS contributions. The feature at m/z = 111 in (a) is from a known contaminant in the spectrometer.

5.3.5 Probing of Cooler Molecules with Increased Extraction Delay

VUV-SNMS spectra of coniferyl alcohol at 9 eV are collected with several different extraction time delays and shown in Figure 5.11. The quoted delay values correspond to the time from the end of the first extraction pulse that suppresses secondary ions formed by the Bi_3^+ pulse to the beginning of the second pulse. This time also corresponds (within ~0.1 μs) to the time between the end of the primary ion pulse and the beginning of the second extraction pulse. As can be seen from Figure 5.11, the parent-to-fragment ratio increases with increasing delay time until 2.85 μs, at which point the intensity of the lower mass fragments increase from the relatively large contribution of the incompletely subtracted secondary ion background. The decreased fragmentation with longer delay time is understandable since molecules with lower internal energy are expected to leave the surface with less kinetic energy.[43] Longer extraction delay thus preferentially extracts VUV-postionized neutrals with lower internal energy and correspondingly reduced amounts of dissociative photoionization. The effect of the extraction delay is fairly dramatic in the case of coniferyl alcohol, possibly due to the particular energies needed to fragment the parent molecule. From the TDMB data, it is observed that coniferyl alcohol starts to fragment into m/z = 137 with the additional input of ~2.75 eV over the coniferyl alcohol ionization energy. This is comparable to the ~2.5 eV of internal energy that is deposited into the molecule from the ion sputtering event.[22]

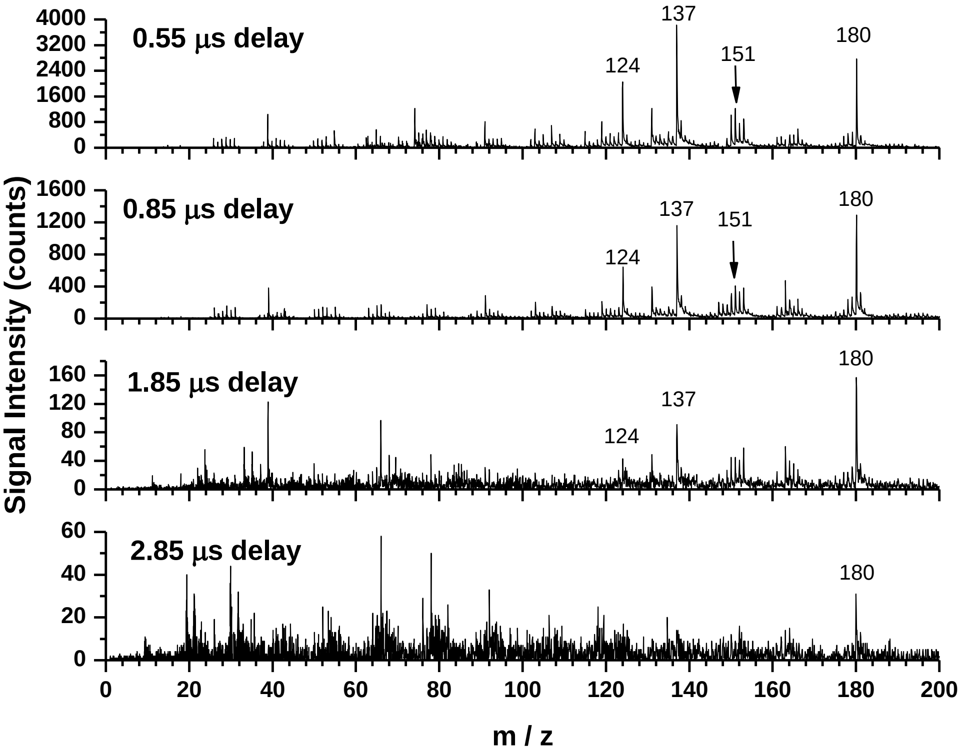

Figure 5.11: VUV-SNMS spectra of coniferyl alcohol at 9 eV, taken with increasing extraction delay. The parent-to-fragment ratio increases with increasing delay, until residual, background SIMS contributions dominate at 2.85 μs.

5.3.6 VUV-SNMS Sensitivity and Improvements

The more predictable fragmentation patterns observed in VUV-SNMS provide a significant advantage over SIMS analysis, where the amount of useful information extracted is often limited by the interpretation of complicated mass spectra. VUV-SNMS also has the benefit of being a more quantitative technique due to the reduced matrix effects observed in ion-sputtered neutrals[23]; hence the relative abundances of a compound from spot to spot can be more readily determined. As was alluded to earlier, however, this simplification of data interpretability comes at the price of sensitivity. From the intensity scales in Figures 5.8 and

5.10, it can be seen that the typical signal counts of SIMS are $10\text{-}10^3$ times more intense than those for VUV-SNMS. This diminished sensitivity stems from the limited synchrotron photon flux and from the fact that most of the (quasi-continuous) VUV photons arrive at a time that does not coincide with the desorption event. Improved suppression of secondary ions could reduce the extraction delay necessary for the current double pulsing scheme, thus increasing VUV-SNMS signal intensities. Other future improvements to the sensitivity may arise by enhancing neutral desorption yields or by performing photoionization with a higher peak power, next generation light source.[44]

5.4 Conclusion

Coniferyl alcohol is studied in detail using single photon ionization with TDMB, VUV-SNMS and SIMS. The IE of coniferyl alcohol is measured to be 7.6 eV ± 0.05 eV. Sinapyl alcohol is also briefly investigated, and the IEs of sinapyl and dihydrosinapyl alcohols are both <7.4 eV. Fragments observed in the TDMB experiments are mainly the products of dissociative photoionization of the parent cation. M/z = 152 and 151 in the coniferyl alcohol sample arise from small amounts of vanillin within the sample. With these exceptions, the measured coniferyl alcohol fragment AEs are consistent with calculated AEs of optimized structures described in previously-postulated fragmentation mechanisms.[37]

The presence of CO in the coniferyl alcohol VUV-SNMS spectra indicates that the photoionization of released neutral gas-phase species as well as dissociative photoionization of sputtered parent molecules contribute to the VUV-SNMS signals of the monolignols. Mechanisms that lead to the release of neutral gas-phase fragments may account for the clusters of "SIMS-like" peaks in the VUV-SNMS spectra around m/z = 150 and 165, since these peaks do not arise as dissociative photoionization products in the TDMB experiments. Such sources of neutrals may contribute to the VUV-SNMS spectra even when single-photon ionization is performed at threshold energies. CO formed as a co-fragment of positive secondary ion fragments contributes negligibly to the total CO observed.

Although it may not be possible to obtain completely fragment-free VUV-SNMS spectra, they are more straightforward to interpret compared to the corresponding SIMS spectra since VUV-SNMS have similar fragments as TDMB experiments. These shared fragments may be due to large contributions from dissociative photoionization of internally hot sputtered neutral parent molecules, and can be suppressed with the use of longer extraction delays, wherein the cooler populations of the desorbed neutral plume are sampled. Furthermore, the common peaks in the VUV-SNMS and TDMB experiments allow for the identification of characteristic mass markers for compounds of interest, thus improving the practical feasibility of more comprehensive chemical imaging studies of lignin and related compounds.

References

(1) Lin, Z.; Qinghu; Xu, Y. *Progress in Natural Science* **2003**, *13*, 321

(2) Boerjan, W.; Ralph, J.; Baucher, M. *Annu. Rev. Plant Biol.* **2003**, *54*, 519.

(3) Hisano, H.; Nandakumar, R.; Wang, Z.-Y. *In Vitro Cellular & Developmental Biology - Plant* **2009**, *45*, 306.

(4) Humphreys, J. M.; Chapple, C. *Current Opinion in Plant Biology* **2002**, *5*, 224.

(5) Schmidt, M.; Schwartzberg, A.; Perera, P.; Weber-Bargioni, A.; Carroll, A.; Sarkar, P.; Bosneaga, E.; Urban, J.; Song, J.; Balakshin, M.; Capanema, E.; Auer, M.; Adams, P.; Chiang, V.; Schuck, P. *Planta* **2009**, *230*, 589.

(6) Bahng, M. K.; Mukarakate, C.; Robichaud, D. J.; Nimlos, M. R. *Analytica Chimica Acta* **2009**, *651*, 117.

(7) Reale, S.; Di Tullio, A.; Spreti, N.; De Angelis, F. *Mass Spectrometry Reviews* **2004**, *23*, 87.

(8) Izumi, A.; Kuroda, K. *Rapid Communications in Mass Spectrometry* **1997**, *11*, 1709.

(9) Streibel, T.; Fendt, A.; Geißler, R.; Kaisersberger, E.; Denner, T.; Zimmermann, R. *Journal of Thermal Analysis and Calorimetry* **2009**, *97*, 615.

(10) Tokareva, E. N.; Pranovich, A. V.; FardiM, P.; Danie, G.; Holmbom, B. *Holzforschung* **2007**, *61*, 647.

(11) Saito, K.; Kato, T.; Takamori, H.; Kishimoto, T.; Fukushima, K. *Biomacromolecules* **2005**, *6*, 2688.

(12) Saito, K.; Kato, T.; Tsuji, Y.; Fukushima, K. *Biomacromolecules* **2005**, *6*, 678.

(13) Kollmer, F.; Bourdos, N.; Kamischke, R.; Benninghoven, A. *Applied Surface Science* **2003**, *203-204*, 238.

(14) McLafferty, F. W.; Turecek, F. *Interpretation of Mass Spectra*, 4 ed.; University Science Books: Sausalito, CA, 1993.

(15) Wood, M.; Zhou, Y.; Brummel, C. L.; Winograd, N. *Analytical Chemistry* **1994**, *66*, 2425.

(16) Wittig, A.; Arlinghaus, H. F.; Kriegeskotte, C.; Moss, R. L.; Appelman, K.; Schmid, K. W.; Sauerwein, W. A. G. *Molecular Cancer Therapeutics* **2008**, *7*, 1763.

(17) Müller, U.; Schittenhelm, M.; Schmittgens, R.; Helm, H. *Surface and Interface Analysis* **1999**, *27*, 904.

(18) Willingham, D.; Kucher, A.; Winograd, N. *Chemical Physics Letters* **2009**, *468*, 264.

(19) Mysak, E. R.; Wilson, K. R.; Jimenez-Cruz, M.; Ahmed, M.; Baer, T. *Analytical Chemistry* **2005**, *77*, 5953.

(20) Cool, T. A.; Nakajima, K.; Mostefaoui, T. A.; Qi, F.; McIlroy, A.; Westmoreland, P. R.; Law, M. E.; Poisson, L.; Peterka, D. S.; Ahmed, M. *Journal of Chemical Physics* **2003**, *119*, 8356.

(21) Streibel, T.; Geißler, R.; Saraji-Bozorgzad, M.; Sklorz, M.; Kaisersberger, E.; Denner, T.; Zimmermann, R. *Journal of Thermal Analysis and Calorimetry* **2009**, *96*, 795.

(22) Zhou, J.; Takahashi, L. K.; Wilson, K. R.; Leone, S. R.; Ahmed, M. *Analytical Chemistry* **2010**, *82*, 3905.

(23) Takahashi, L. K.; Zhou, J.; Wilson, K. R.; Leone, S. R.; Ahmed, M. *Journal of Physical Chemistry A* **2009**, *113*, 4035.

(24) Freudenberg, K.; Neish, A. *Constitution and Biosynthesis of Lignin*; Springer-Verlag: Berlin, 1968.

(25) Nicolas, C.; Shu, J.; Peterka, D. S.; Hochlaf, M.; Poisson, L.; Leone, S. R.; Ahmed, M. *Journal of the American Chemical Society* **2005**, *128*, 220.
(26) Belau, L.; Wilson, K. R.; Leone, S. R.; Ahmed, M. *The Journal of Physical Chemistry A* **2007**, *111*, 7562.
(27) Amirav, A.; Even, U.; Jortner, J. *Chemical Physics* **1980**, *51*, 31.
(28) Heimann, P. A.; Koike, M.; Hsu, C. W.; Blank, D.; Yang, X. M.; Suits, A. G.; Lee, Y. T.; Evans, M.; Ng, C. Y.; Flaim, C.; Padmore, H. A. *Review of Scientific Instruments* **1997**, *68*, 1945.
(29) Byrd, J. M. *Nuclear Instruments & Methods in Physics Research, Section A: Accelerators, Spectrometers, Detectors, and Associated Equipment* **1999**, *427*, 614.
(30) Kaiser, R. I.; Maksyutenko, P.; Ennis, C.; Zhang, F.; Gu, X.; Krishtal, S. P.; Mebel, A. M.; Kostko, O.; Ahmed, M. *Faraday Discussions* **2010**.
(31) Suits, A. G.; Heimann, P.; Yang, X.; Evans, M.; Hsu, C.-W.; Lu, K.-t.; Lee, Y. T.; Kung, A. H. *Review of Scientific Instruments* **1995**, *66*, 4841.
(32) Frisch, M. J., Trucks, G. W., Schlegel, H. B., Scuseria, G. E., Robb, M. A., Cheeseman, J. R., Montgomery, Jr., J. A., Vreven, T., Kudin, K. N., Burant, J. C., Millam, J. M., Iyengar, S. S., Tomasi, J., Barone, V., Mennucci, B., Cossi, M., Scalmani, G., Rega, N., Petersson, G. A., Nakatsuji, H., Hada, M., Ehara, M., Toyota, K., Fukuda, R., Hasegawa, J., Ishida, M., Nakajima, T., Honda, Y., Kitao, O., Nakai, H., Klene, M., Li, X., Knox, J. E., Hratchian, H. P., Cross, J. B., Bakken, V., Adamo, C., Jaramillo, J., Gomperts, R., Stratmann, R. E., Yazyev, O., Austin, A. J., Cammi, R., Pomelli, C., Ochterski, J. W., Ayala, P. Y., Morokuma, K., Voth, G. A., Salvador, P., Dannenberg, J. J., Zakrzewski, V. G., Dapprich, S., Daniels, A. D., Strain, M. C., Farkas, O., Malick, D. K., Rabuck, A. D., Raghavachari, K., Foresman, J. B., Ortiz, J. V., Cui, Q., Baboul, A. G., Clifford, S., Cioslowski, J., Stefanov, B. B., Liu, G., Liashenko, A., Piskorz, P., Komaromi, I., Martin, R. L., Fox, D. J., Keith, T., Al-Laham, M. A., Peng, C. Y., Nanayakkara, A., Challacombe, M., Gill, P. M. W., Johnson, B., Chen, W., Wong, M. W., Gonzalez, C., and Pople, J. A. Gaussian 03; Gaussian, Inc: Wallingford, CT, 2004.
(33) Wei, K.; Luo, S. W.; Fu, Y.; Liu, L.; Guo, Q. X. *Journal of Molecular Structure-Theochem* **2004**, *712*, 197.
(34) Wilson, K. R.; Jimenez-Cruz, M.; Nicolas, C.; Belau, L.; Leone, S. R.; Ahmed, M. *Journal of Physical Chemistry A* **2005**, *110*, 2106.
(35) ten Have, R.; Rietjens, I. M. C. M.; Hartmans, S.; Swarts, H. J.; Field, J. A. *FEBS Letters* **1998**, *430*, 390.
(36) Ponomarev, D.; Sergeev, Y. *Chemistry of Natural Compounds (Translation of Khimiya Prirodnykh Soedinenii)* **1982**, *18*, 764.
(37) Kovacik, V.; Skamla, J.; Joniak, D.; Kosikova, B. *Chem. Ber.-Recl.* **1969**, *102*, 1513.
(38) Masuku, C. P. *Journal of Analytical and Applied Pyrolysis* **1992**, *23*, 195.
(39) Kim, H.; Ralph, J. *Journal of Agricultural and Food Chemistry* **2005**, *53*, 3693.
(40) Page, R. H.; Larkin, R. J.; Shen, Y. R.; Lee, Y. T. *Journal of Chemical Physics* **1988**, *88*, 2249.
(41) Tonkyn, R. G.; Winniczek, J. W.; White, M. G. *Chemical Physics Letters* **1989**, *164*, 137.
(42) Cairns, R. B.; Samson, J. A. R. *J. Geophys. Res.* **1965**, *70*, 99.
(43) Chatterjee, R.; Postawa, Z.; Winograd, N.; Garrison, B. J. *Journal of Physical Chemistry B* **1998**, *103*, 151.
(44) Khan, S. *Journal of Modern Optics* **2008**, *55*, 3469

Chapter 6

Analysis of Coniferyl Alcohol and Alkali and Organosolv Lignins with Synchrotron Vacuum-UV Photoionization Mass Spectrometry

6.1 Introduction

Lignin is the second most abundant biopolymer on Earth, after cellulose, and it interacts closely with cellulose and hemicelluloses in plant cell walls. It is responsible for conferring strength and rigidity to plants and is also resistant to bacterial and fungal degradation,[1] which has implications for its role in the environment. From a more practical point of view, lignin presents problems in the production of products such as paper and lignocellulose-based ethanol biofuels. It decreases ethanol biofuel yields and slows the hydrolysis of cellulose, thus impeding economically viable production of renewable fuels from plant biomass.

Several groups have sought to address this problem by reducing the lignin content in plants by making it more easily degradable;[2] however genetic modifications can have a negative impact on plant growth[3] or can lead to changes to the lignin distribution and structure within plant tissues.[4] There are groups working on the development of novel pretreatment methods, which are optimized for separating the cellulose from lignin and other components efficiently. New biological[5] and ionic liquid solvent[6] pretreatments, as well as the conversion of lignin to valuable products are being explored.[7] In each process, however, the details of the lignin chemistry that govern the generation of end-products are not well understood.

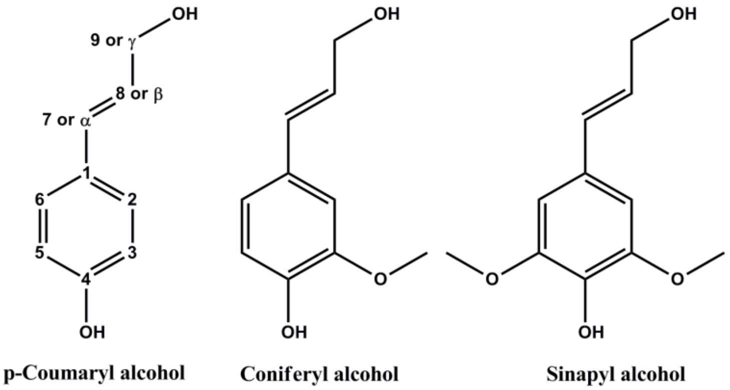

Figure 6.1: Major monomer structures and the commonly-used carbon atom designations

In order to improve biomass pretreatment methods and to utilize lignin more efficiently, it would be desirable to understand the chemical and structural transformations of lignin upon various perturbations; however lignin has been a difficult material to study, and the details of its unmodified structure within native plant tissue remain elusive. It is well-known that lignin is a cross-linked polymer composed of monomer units, which primarily includes p-coumaryl, coniferyl and sinapyl alcohol (see Figure 6.1 for monomer structures and commonly-used bond designations). It is also well established by NMR that β-O-4 bonds (β carbon atom bonded to oxygen atom on carbon 4; see Figure 6.1) form the majority of inter-monomer linkages; however the less abundant structures within the polymer are more difficult to determine. To date, there remains no routine way for determining lignin primary structure.[8]

Complete structural information of lignin is difficult to obtain with traditional analytical methods. It is difficult to study using gas chromatography (GC) because of its high molecular weight and low vapor pressure. Pyrolysis has been used, usually in combination with mass spectrometry, to determine lignin polymer structure. Pyrolysis gas chromatography (Py-GC) and mass spectrometry (MS) have been used extensively in the past to study lignin structure.[9] While these studies have provided valuable information, the detected compounds are only partially reflective of the composition of the original sample.[10] Py-GC naturally involves the introduction of thermal energy into the system, which can induce chemistry and modify the sample. Py-GC MS may contain compounds with altered functional groups not reflective of the original molecules in the system.[10] Furthermore, the ionization techniques typically used to probe pyrolyzed material in the gas phase often introduce excess energy, which can lead to molecular fragmentation during ionization. This further complicates data interpretation and makes it difficult to determine the identity of the original compound.

The problem of lignin sequencing or "lignomics" has been the subject of study in previous work involving negative ion liquid chromatography (LC) mass spectrometry of model lignin oligomers.[8,11] This represents progress in the molecular-level understanding of lignin structure and chemistry. By identifying mass signatures that are characteristic of single oligomer standards and extending this data to real systems,[8] chemical bonding information can be deduced. Due to the variations of lignin structure even within a single plant or plant cell, however, it would be desirable to obtain such lignin structural information while preserving its spatial context.

Sub-micron spatial information can be used to resolve the relative concentrations of lignin and other plant biopolymers within and between individual cells, while spatial resolution of 30 µm or more can be used to obtain information within specific parts of a plant tissue. Chemical information on these spatial length scales is obtained by imaging mass spectrometry. SIMS or MALDI (see Section 6.1) are two examples of imaging mass spectrometry, which both utilize a probe (primary ions for SIMS and a desorption laser for MALDI) for performing localized removal of material from a sample. SIMS has previously been used to identify characteristic lignin ions[12,13] and to image lignin distributions in plant sections with high spatial resolution;[14,15] however the ions that are detected in such studies are generally limited to the mass regions around the monomers and their fragments. MALDI imaging of plant tissue has also been performed,[16] and it can be used to identify larger fragments; however MALDI has lower spatial resolution (>30 µm) and requires the addition of matrix compounds that can interfere or cluster with mass features of interest. Laser desorption ionization (LDI) of plant tissue has also been performed, without the addition of a matrix compound,[17] but like MALDI, the desorption and ionization events are coupled. As a result, LDI requires higher laser peak powers compared to postionization techniques, which have been observed to enhance clustering and other effects within the ablation plume over inorganic systems.[18]

Synchrotron VUV light has been shown to be a soft ionization source that can yield fragment-free mass spectra for a variety of molecule types. Synchrotron VUV has been recently coupled to a SIMS instrument and applied to the analysis of inorganic and organic systems.[19,20] Previous work using VUV photoionization of ion-sputtered coniferyl and sinapyl alcohols showed that intact monomers can be effectively detected using VUV photoionization;[21] however the large amounts of internal energy[20] introduced into the monomers during ion sputtering results in significant molecular fragmentation.[21] More recently, the SIMS instrument has also been equipped with a laser, permitting experiments using laser desorption and synchrotron VUV-postionization (VUV-LDPI). VUV-LDPI experiments show that laser-desorbed molecules can leave the surface with much less internal energy compared to ion sputtered molecules.[22] During the analysis of extracted lignin polymers, lignin oligomers are observed, indicating that gentle desorption combined with soft photoionization may preserve valuable chemical bonding information.

In this chapter, coniferyl alcohol, a monomer unit of lignin, is investigated as a test molecule to examine the effectiveness of VUV-LDPI for intact detection of lignin-like compounds. The results are compared to previous results obtained for the same system with ion-sputtering (VUV-secondary neutral mass spectrometry – VUV-SNMS), secondary ion mass spectrometry (SIMS), and low internal energy molecules in thermal desorption molecular beams (TDMB – see Chapter 5).[21] These results are then used to interpret similar analyses of commercially isolated lignins (alkali and organosolv lignin; Sigma Aldrich) and organosolv lignin isolated from *Miscanthus giganteus* using SIMS, VUV-SNMS, VUV postionization of thermally desorbed molecules with an effusive source (VUV-TD) and VUV-LDPI. From the laser dosage and laser power dependence of these spectra as well as the photoionization efficiency (PIE) curves for the observed mass features, the mechanisms for the appearance of detected fragments are deduced. The implications of these results to lignin laser pyrolysis and lignin structure are also discussed.

6.2 Experimental Methods

6.2.1 Secondary Ion / Neutral Mass Spectrometry

Coniferyl alcohol and lignin samples are prepared on silicon wafers. For SIMS analyses, positive ion species ejected from a sample held at ground potential are recorded following bombardment with ~1 ns pulses of 25 kV Bi_3^+ primary ions focused to a spot diameter of ~2 µm. Areas of 150 µm x 150 µm are scanned 20 times with a 64 x 64 raster with no electron charge compensation.

VUV-SNMS of the lignin samples is performed using un-bunched, 50 ns pulses of Bi_3^+ ions of the same kinetic energy, over the same sample area. The neutral population of the desorbed plume is probed with synchrotron VUV photoionization (~0.2 eV spectral width, ~10^{15} photons/s) at various photon wavelengths. The light source and the double pulse extraction scheme used to detect the photoionized neutrals have been described earlier (see Chapters 4 and 5).[20,21] For the VUV-SNMS mass spectra presented here, a 0.5 µs delay is used between the two extraction pulses.

6.2.2 Laser Desorption with Synchrotron Vacuum-Ultraviolet Postionization

Laser desorption with synchrotron photoionization is performed on coniferyl alcohol and the lignin samples dispersed on silicon wafers. The experimental setup is described previously[22] (see also Chapter 2). A 349 nm (3.55 eV) Nd:YLF desorption laser emitting ns pulses is focused to a spot diameter of ~30 µm and is used at various laser peak power densities ranging from ~1 MW/cm^2 to 20 MW/cm^2, depending on the sample type and analysis desired. Mass spectra are typically collected while the sample is linearly scanned at a fixed speed, although data are also collected on fixed sample spots. Postionization at several different photon energies is performed with synchrotron radiation passing approximately 50 µm to 150 µm above the sample surface. The spectral width of the ionizing light are the same as in the VUV-SNMS experiments (~0.2 eV); however in some cases flux-limiting slits (HBDA and VBDA; see Chapter 2) are employed to reduce the photon flux to avoid detector saturation.

6.2.3 Effusive Thermal Desorption with Vacuum-Ultraviolet Photoionization

Effusive thermal desorption is performed on a home-built apparatus equipped with a cartridge heater that heats the chemical compounds below the repulsive electrode in the extraction / ionization region. Here, thermally desorbed neutral molecules pass through a 1 mm diameter hole in the repulsive electrode and are ionized 5 mm above the repulsive electrode before being photoionized with a monochromatized photon beam (0.05 eV spectral width, ~10^{14} photons/s) and being extracted into a reflectron time-of-flight mass (ToF) spectrometer.

Effusive thermal desorption (VUV-TD) experiments are also performed on the imaging apparatus, utilizing the heating/cooling (H/C) stage (see Chapter 2) with non-monochromatized light (~0.2 eV spectral bandwidth).

6.2.4 Sample Preparation

Coniferyl alcohol samples for SIMS, VUV-SNMS and VUV-LDPI analysis are prepared by placing several mg of coniferyl alcohol (Alfa Aesar, 98% purity) directly onto a piece of silicon wafer. The coniferyl alcohol is dispersed across the silicon surface with a drop of high-purity methanol, and the solvent is allowed to air dry.

Lignin samples are prepared using two different methods. Most of the data presented is collected on samples that were dissolved in high-purity methanol. A few mg of lignin is mixed with ~5 ml of high-purity methanol and allowed to sit undisturbed for ~10 minutes. A few drops of the top dissolved solution are deposited onto a silicon wafer and is allowed to air dry. To see if the solvent has any impact on the mass spectra, alkali lignin samples are also prepared with the lignin powder, without dissolving in a solvent. In this case, a pointed metal probe is used to gently spread the finest pieces of the lignin powder onto the silicon substrate, and larger lignin particles are gently wiped away with a piece of lens paper to ensure a flat sample surface.

6.3 Results & Discussion

6.3.1 Photoionization Studies of Coniferyl Alcohol

SIMS and VUV-SNMS analysis of coniferyl alcohol have been performed previously (see Chapter 5).[21] To gain insight into how laser desorption of lignin-like compounds compares to these methods, coniferyl alcohol is investigated here with VUV-LDPI. Figure 6.2a shows the mass spectrum of coniferyl alcohol with 9 eV photoionization, a 2 mm / s sample scanning rate and a 2500 Hz repetition rate. Under these conditions, each 30 µm area of the sample is exposed to ~38 laser pulses of approximately 0.9 µJ and ~8 ns duration (laser peak power density ~15.9 MW/cm^2), and the total probed area for each mass spectrum is less than 0.3 mm^2.

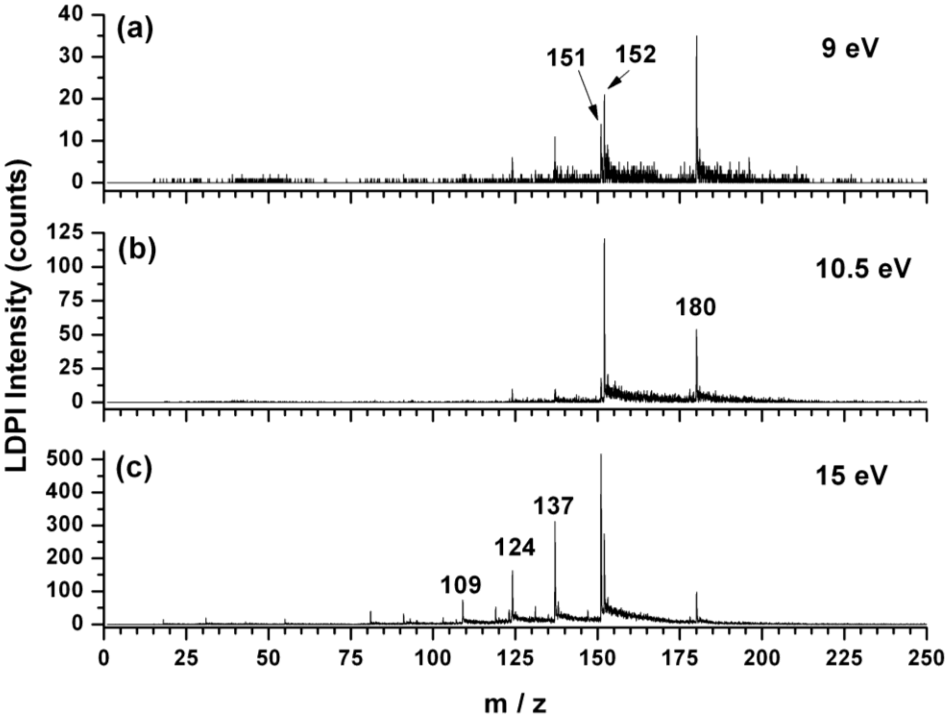

Figure 6.2: VUV-LDPI mass spectra of coniferyl alcohol collected with sample scan rate of 2 mm / s, corresponding to ~38 laser pulses per 30 µm area and a laser peak power density of ~15.4 MW/cm^2

The coniferyl alcohol parent (m/z = 180) is the most dominant feature in the VUV-LDPI mass spectrum at 9 eV (Figure 6.2a), which is consistent with the low dissociative photoionization yield that is observed at this low photon energy for cold coniferyl alcohol molecules.[21] When the photon energy is increased to 10.5 eV (Figure 6.2b), dissociative photoionization fragments m/z = 124 and 137 increase in relative intensity with respect to coniferyl alcohol parent, such that the m/z 124:137:180 ratios are 1:1.8:6.4, and the ionization cross section of the sample contaminant vanillin (m/z = 152) increases. At 15 eV (Figure 6.2c), the relative intensity of the parent (m/z = 180) has clearly decreased with respect to the m/z = 124 and 137 fragments due to dissociative photoionization, and the m/z 124:137:180 ratios are 1:1.8:0.5. Background signals from prompt ions and the synchrotron's ionization of background gas are not significant at any of the photon energies examined under the conditions used to collect the spectra of Figure 6.2.

In previous experiments of coniferyl alcohol in a molecular beam using monochromatized light, it was observed that it is possible to obtain fragment-free mass spectra with photoionization at 9 eV, and dissociative photoionization fragments at m/z = 124 and 137 only appear at higher photon energies.[19] In the present VUV-LDPI experiment, fragments are observed at 9 eV (Figure 6.2a), and peaks at m/z = 152 and a fragment at m/z = 151 are also observed indicating the presence of vanillin. This increase in dissociative photoionization in the present VUV-LDPI experiments can be attributed to the fact that non-monochomatized light is used. In addition to having a much broader spectral bandwidth (~0.2 eV compared to ~0.05 eV), non-monochromatized synchrotron VUV light contains larger contributions from higher harmonic radiation. This small fraction of higher energy photons yield the observed fragment ions at m/z = 124 and 137.

To evaluate the internal energy imparted into laser-desorbed coniferyl alcohol molecules in a more quantitative way, mass spectra are collected versus photon energy in 0.15 eV steps using non-monochromatized light for photoionization. The integrated signal intensities from individual mass peaks are plotted versus photon energy, producing the PIE curves of coniferyl alcohol (m/z = 180) and vanillin (m/z = 152) and the appearance energy (AE) curves for their fragments, some of which are shown in Figure 6.3. Overlaid in Figure 6.3 in gray are the areas between two AE curves obtained from coniferyl alcohol thermally desorbed from an effusive source at 60 °C (*i.e.* VUV-TD), which agree nicely with the curves obtained with VUV-LDPI. Extrapolations of the onset slope and baselines for each of the AE curves yields the AEs for each species, which are summarized and compared to previous values[21] for internally cold molecules produced in a molecular beam (*i.e.* TDMB) and ion sputtered coniferyl alcohol (*i.e.*VUV-SNMS) in Table 6.1.

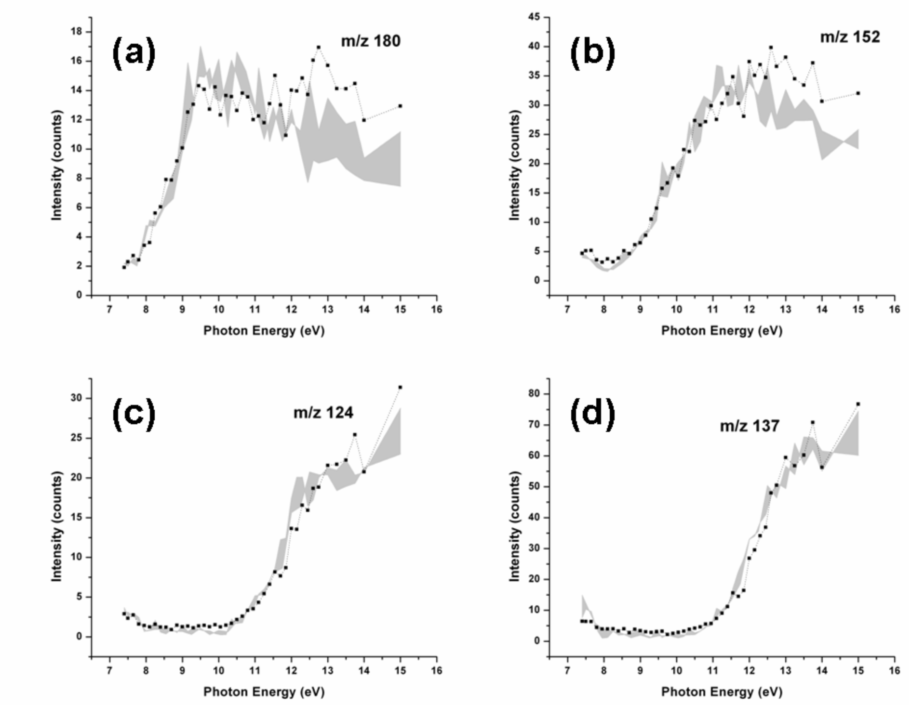

Figure 6.3: PIEs of VUV-LDPI coniferyl alcohol fragments compared to two AE curves for coniferyl alcohol in VUV-thermal desorption with an effusive source (gray shading), both collected with photoionization by 0.2 eV spectral width synchrotron radiation and a laser peak power density of ~3 MW/cm^2

	VUV-LDPI and VUV-TD (this work)	**TDMB[21] (lowest internal energy)**	**VUV-SNMS[21] (highest internal energy)**
m/z 124	10.3±0.3	10.50±0.05	8.4±0.5
m/z 137	10.2±0.3	10.35±0.05	8.2±0.5
m/z 152 (vanillin)	8.3±0.3	8.3±0.2	--
m/z 180 (coniferyl alcohol)	8.0±0.5	7.60±0.05	8.0±0.5

Table 6.1: Comparison of AEs for various coniferyl alcohol- and vanillin-related peaks. "--" indicates that no accurate value is available. VUV-TDMB stands for VUV-thermal desorption molecular beam.

As can be seen in Table 6.1, the AEs for the major known fragments of coniferyl alcohol (m/z = 124 and 137) are similar in VUV-LDPI and in TDMB. In TDMB experiments, thermally desorbed molecules are introduced into a molecular beam, producing a population of internally cold molecules. It was found previously that the fragments at m/z = 124 and 137 arise from dissociative photoionization and have AEs of 10.50 eV ± 0.05 and 10.35 eV ± 0.05 eV, respectively.[21] Although the TDMB AEs were obtained with higher spectral-resolution ionizing radiation, thus leading to subtle differences in the obtained PIE curves, these AE values agree well with those observed in the VUV-LDPI experiments, which are 10.3 eV ± 0.2 eV and 10.2 eV ± 0.2 eV for m/z = 124 and m/z = 137, respectively. The differences observed in the AEs are within error bars, which are dominated by the ~0.2 eV spectral width of the ionizing light. The similarities of the AEs for m/z = 124 and 137 suggest that in VUV-LDPI experiments these two masses arise predominantly from dissociative photoionization of intact coniferyl alcohol in the gas phase, and are not the result of photoionization of desorbed neutral fragments.

Since the AEs of dissociative photoionization molecular fragments are an indicator of the internal energy contained within the neutral parent molecules, the minimal differences in the AE curves also indicate that little internal energy is imparted to laser-desorbed molecules. This is in contrast to previous results using the same system for the DNA bases, where a ~0.85 eV shift can clearly be observed in the AE curves of the fragments arising from more ablative laser conditions.[22] This difference in internal energy may be due to the fact that the desorption laser in the present case is operated at much lower peak power densities (energy per pulse per area / pulse duration ≈ 15.3 MW/cm^2) such that no massive material ejection (ablation) is visible. This lower peak power is chosen to minimize induced chemistry on the sample by the sample probe (*e.g.* pyrolysis). Under these thermal desorption conditions, the energy that is deposited into the sample is believed to go toward increasing the local temperature of the sample surface.[22]

The minimal shifts in the fragment AE curves also contrasts with the dramatic differences in the AE curves observed for ion-sputtered coniferyl alcohol molecules, where the AEs are shifted by several eV.[21] This result confirms that the degree of fragmentation observed in each of these methods depends highly on the method for introducing the molecules into the gas phase. The laser desorption methods used here impart less internal energy into released surface molecules than ion sputtering, and therefore laser desorption results in much less dissociative photoionization. This also yields less complicated mass spectra, which is particularly valuable for simplifying molecular assignments within a sample that is a heterogeneous mixture of compounds. Under optimal VUV-LDPI conditions, there are no additional peaks in the VUV-LDPI mass spectra of coniferyl alcohol that cannot be explained by dissociative photoionization or the presence of vanillin, which is not the case in VUV-SNMS analysis.[21] Thus, VUV-LDPI also apparently induces fewer chemical modifications than VUV-SNMS to the probed sample.

Although little sample damage is apparent with the laser desorption scheme used for the spectra in Figure 6.2, the laser can induce a gradual change in the sample surface. In order to investigate the laser's potential to induce chemical damage, the sample is scanned at different speeds, thereby changing the laser dosage per area. By probing the sample in this manner, the overall effect of sample damage on the detection and identification of a single-component is made clear. Figure 6.4 shows scans for coniferyl alcohol collected with 2 mm/s (38 pulses / 30 µm), 0.01 mm/s (760 laser pulses / 30 µm-diameter area) and 0 mm/s (2 x 10^5 laser pulses / 30 µm-diameter area) sample scanning rates and photoionization at 10.5 eV. At a desorption laser energy of ~0.25 µJ/pulse, corresponding to a peak power density of ~3 MW/cm^2, the mass spectrum is initially dominated by vanillin within the sample (Figure 6.4a). At 0.01 mm/s, the sample shows the characteristic dissociative photoionization fragments of coniferyl alcohol at m/z = 137 and 124, as well as a possible degradation product at m/z = 164 (Figure 6.4b). When the sample is fixed (Figure 6.4c), pyrolysis peaks are visible at nearly every mass. This illustrates the importance of minimizing the laser dosage to the probed sample areas if detection of the native sample chemical composition is desired.

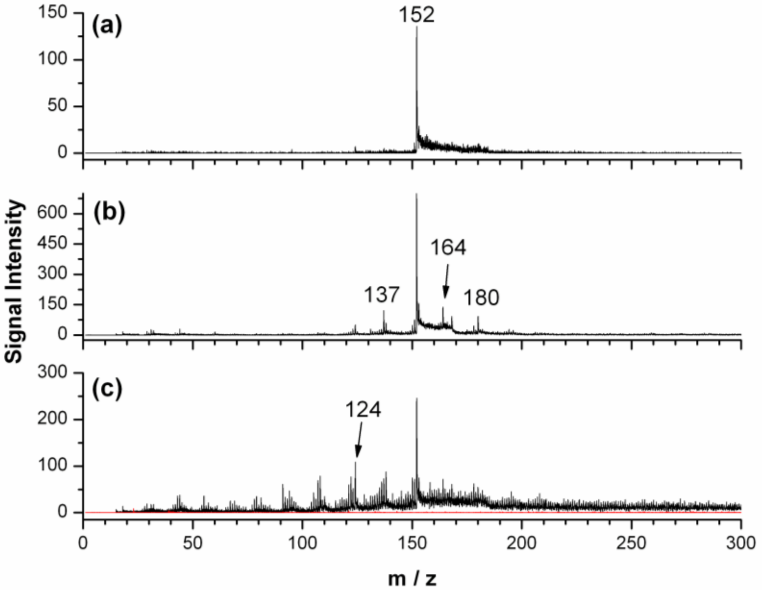

Figure 6.4: Coniferyl alcohol VUV-LDPI mass spectra collected with sample scanning at (a) 2 mm/s, (b) 0.01 mm/s. and (c) 0 mm/s (no scanning). Laser peak power density is ~3 MW/cm^2.

6.3.2 Photoionization Studies of Alkali Lignin

From a previous mass spectrometry study of coniferyl alcohol performed with VUV-SNMS, SIMS and TDMB (see Chapter 5), it was determined that ion-sputtered neutral coniferyl alcohol molecules undergo dissociation upon photoionization and possibly other transformations while exposed to primary ion bombardment on the sample surface.[21] The characteristic signatures that are observed in SIMS and VUV-SNMS depend on how the sample responds to the extra energy of the ion probe. VUV-SNMS and SIMS experiments are performed here to compare how VUV-SNMS signatures of lignin polymers compare with those observed from the monomers.

Figure 6.5 shows the VUV-SNMS mass spectrum of alkali lignin acquired with 25 keV Bi_3^+ bombardment and 10.5 eV photoionization. The spectrum is the sum of nine datasets collected over the same sample area in quick succession, where each dataset is the result of a subtraction: signal from ion gun and synchrotron together – signal from synchrotron background – signal from secondary ions only. By averaging the data in this way, artifacts from charging and/or sample damage are reduced. Despite this averaging, however, there are some residual fluctuations in the secondary ion background from scan to scan, which result in the negative dips in the mass spectrum; nevertheless it can be clearly seen that the most intense mass peaks appear below m/z = 200. This mass range represents the monomers of lignin and their fragments.

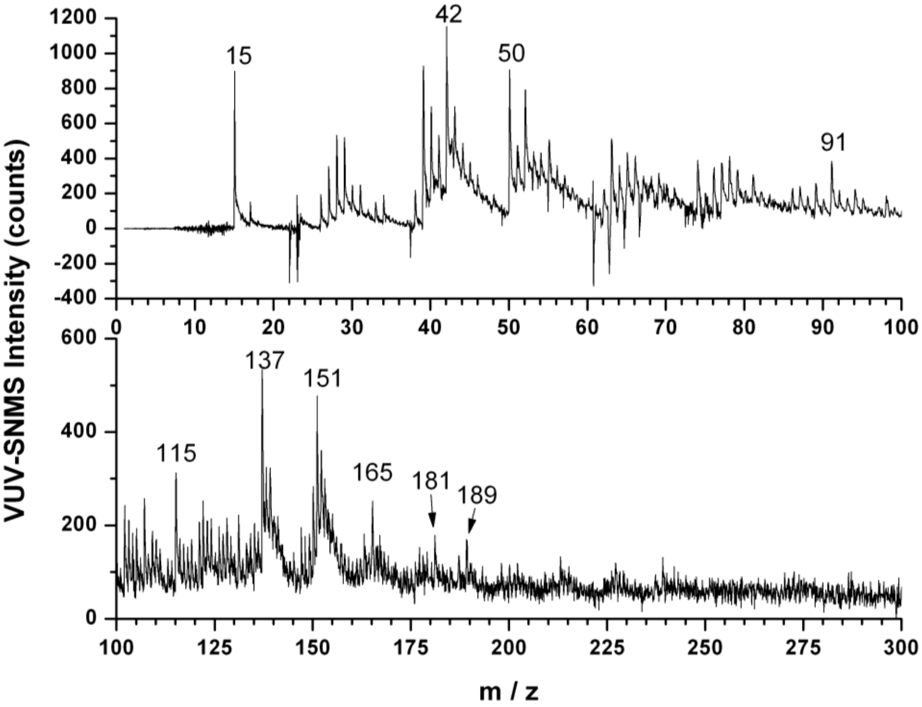

Figure 6.5: VUV-SNMS of alkali lignin with 10.5 eV photoionization

As has been deduced from photoionization studies of monolignols, the ion-sputtered molecular species in VUV-SNMS may fragment during both the ion sputtering step and the photoionization step due to the large amount of internal energy imparted into the released surface molecules. Since the average molecular weight of the alkali lignin sample is expected to be on the order of 10,000 mass units and the dominant features in the VUV-SNMS mass spectrum in Figure 6.5 are under 200 mass units, the ion probe appears to be poorly-suited for detecting higher-mass species that would provide insight into the chemical bonding within the lignin polymer.

One example of a gentler desorption method that can introduce intact neutral molecules to the gas phase is thermal desorption (TD). Figure 6.6 shows the mass spectra obtained for thermally desorbed alkali lignin with VUV photoionization (VUV-TD) at 10.5 eV, collected at three different temperatures. From 100 ºC to 150 ºC (Figure 6.6a-b), very few characteristic signatures of lignin appear, and the mass spectrum is dominated by low masses. M/z = 17 is assigned to ammonia, most likely a contaminant of the alkali lignin sample from the extraction process, due to the agreement between its ~10 eV AE and ammonia's IE.[23] At higher desorption temperatures (Figure 6.6c), larger mass features appear beyond the monomer mass region.

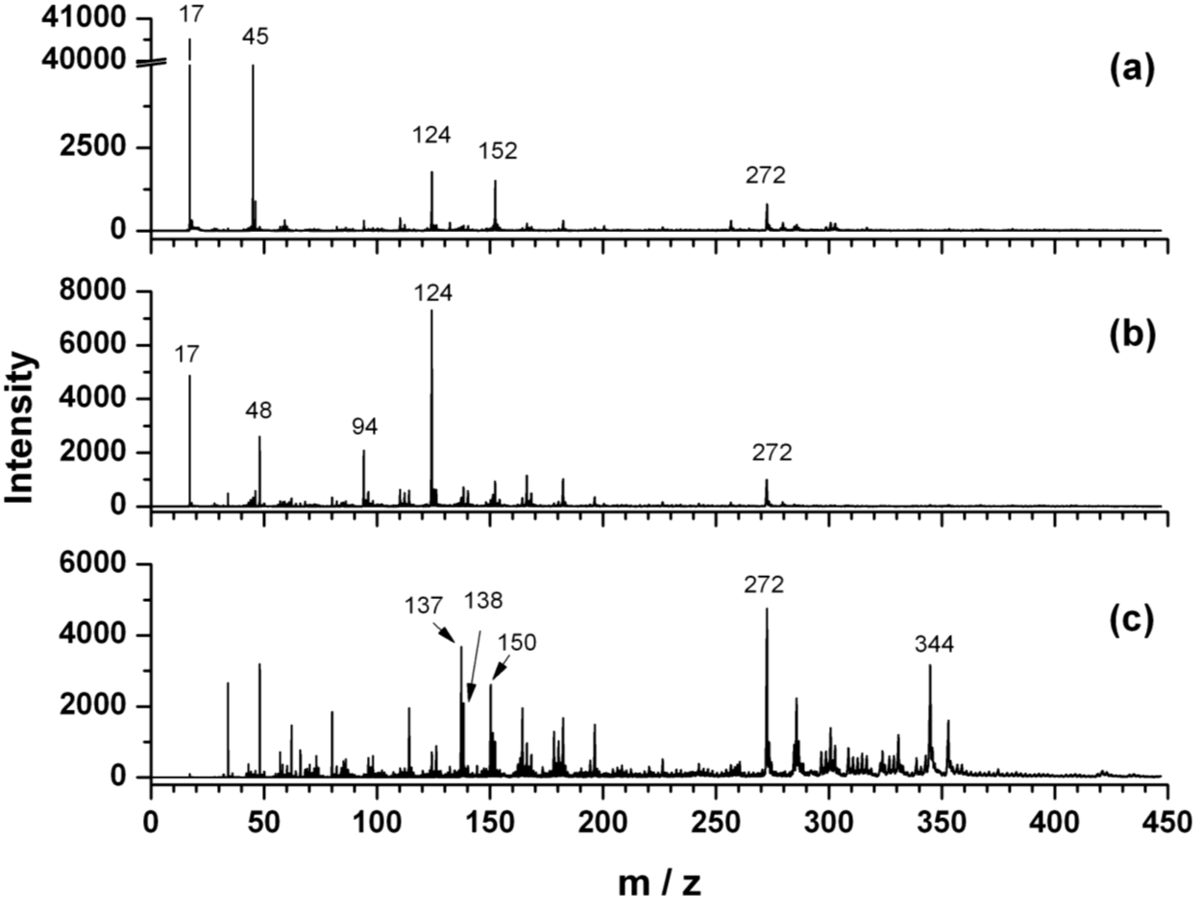

Figure 6.6: Thermal desorption of alkali lignin at (a) 100 °C, (b) 150 °C, and (c) 200 °C with 10.5 eV photoionization.

PIEs for the low-mass features in Figure 6.6 can be compared to commercially available standard molecules to provide insight to their chemical origins. Figure 6.7 shows the AE curves of mass features arising from the thermal desorption of alkali lignin at m/z =124, 152, 164 and 182 overlaid with two PIE curves of pure guaiacol (m/z = 124), vanillin (m/z = 152), eugenol (m/z = 164) and syringaldehyde (m/z = 182) taken at 150 °C and 200 °C. From the curves shown in Figure 6.7a, the m/z = 124 feature from the alkali lignin sample appears to have significant contributions from the direct photoionization of neutral guaiacol molecules, although the AE curves taken at 150 °C and 200 °C deviate slightly at higher photon energies, possibly

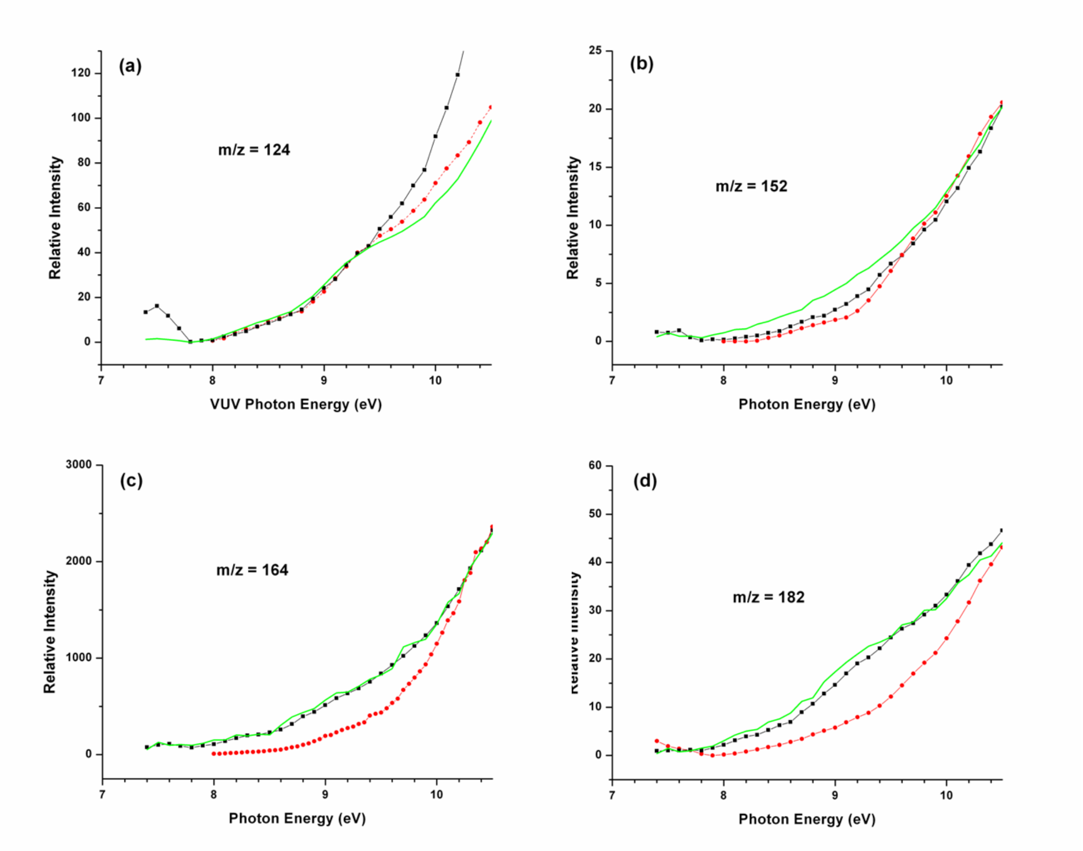

Figure 6.7: AE curves of m/z = 124 (a), 152 (b), 164 (c) and 182 (d) from effusive thermal desorption of alkali lignin at 150 °C (green line) and 200 °C (black squares) compared to the PIEs of known standard molecules of the same mass (a: guaiacol, b: vanillin, c: eugenol, d: syringaldehyde; each in red), collected with 0.05 eV spectral resolution ionizing radiation

indicating that the major contribution to m/z = 124 in the alkali lignin mass spectrum changes with increasing temperature. From the reasonable agreement of the PIE curves in 6.7b, the m/z = 152 feature appears to arise largely from the photoionization of desorbed neutral vanillin molecules. The curve of the m/z = 164 mass feature from lignin heated at 200 °C agrees well with the PIE curve of eugenol, but does not agree well with the AE curve collected at 150 °C (see Figure 6.7c). This may indicate that eugenol dominates this mass channel at higher temperatures, while another species (perhaps isoeugenol) contributes more at lower temperatures. From the different AEs and shape of the AE curves of m/z = 182 in Figure 6.7d, the desorption of neutral syringaldehyde does not appear to be a major contribution to the m/z = 182 signal from lignin.

While the VUV-TD mass spectra of Figure 6.7 can be used to tentatively identify mass features by their AEs and show much higher mass features than mass spectra obtained with a 25 keV Bi_3^+ ion beam, such bulk analysis is not capable of providing spatially resolved chemical information. For this, laser desorption is implemented. Figure 6.8 shows a comparison of the VUV-LDPI mass spectrum for alkali lignin, the VUV-SNMS mass spectrum from Figure 6.5, the thermal desorption mass spectrum of Figure 6.6c, and the positive ion SIMS mass spectrum. The VUV-LDPI mass spectrum is collected using a 2 mm/s sample scanning rate, with a laser peak power density of ~15 MW/cm^2 (~0.9 μJ/pulse laser pulse energy) and 10.5 eV ionizing synchrotron radiation.

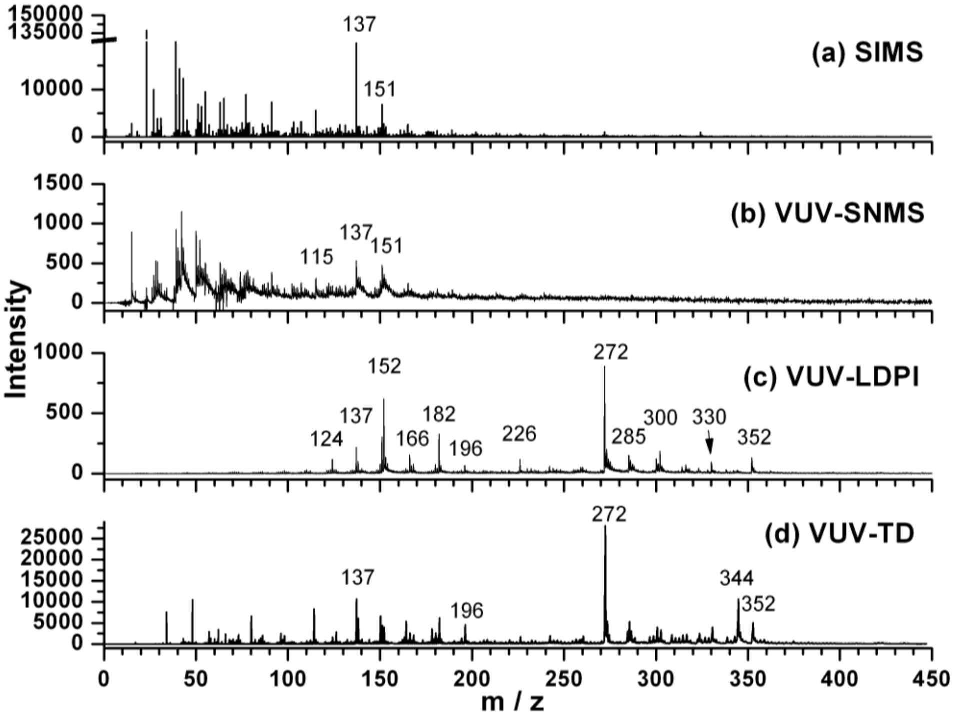

Figure 6.8: Positive ion SIMS, VUV-SNMS, VUV-LDPI and TD of alkali lignin at 10.5 eV

The mass signatures in the SIMS and VUV-SNMS mass spectra are concentrated about the monomer mass region or lower, whereas VUV-TD and VUV-LDPI mass spectra show signatures that extend into the lignin dimer region. The appearance of higher molecular weight species in the VUV-TD and VUV-LDPI mass spectra is consistent with the expectation that both thermal desorption and laser desorption are much gentler desorption methods than sputtering by 25 keV Bi_3^+ primary ions.[20,22] The ability to detect larger species of lignin is highly desirable for imaging chemical change in lignin within plant tissues, therefore the rest of this work will focus on analyzing the origins of the lignin signatures observed with VUV-LDPI.

To begin to understand the desorption mechanism involved in laser desorption, the VUV-LDPI data is compared to VUV-TD. As can be seen from Figure 6.8, the two MS techniques share many features at certain VUV-TD temperatures, however, unlike the VUV-TD mass spectra, the VUV-LDPI mass spectrum shows very low intensity for ammonia (m/z = 17) and has fewer mass features below m/z = 100. The higher relative intensity of other smaller mass species in the VUV-TD mass spectra may be due to contaminants on the heater surface, the relatively large surface area of the sample heater compared to that of the lignin sample, and the lack of replenishment of the lignin sample. Because the VUV-LDPI experiments probe a very small (~30 µm diameter) sample area localized at the surface of the lignin, the relative intensity of low molecular weight contaminants from the underlying substrate are reduced compared to the VUV-TD mass spectra. This fact is most apparent by comparing the ammonia VUV-TD peak of Figure 6.6a to that of the VUV-LDPI mass spectrum of Figure 6.8. Furthermore, the small spot size of the laser allows the sample to be scanned, effectively replenishing the sample that is being probed.

With any laser desorption experiments, one question that naturally arises is whether there is a significant probability for clustering or reactions within the desorbed plume. Here, a simple calculation is performed to estimate the nature of the desorbed plume in the present experiments.

The observed signal intensities are higher with increasing laser power. With a peak laser power density of ~6.5 MW/cm^2 and a 2 mm/s sample scan rate, ~1.1x10^5 counts arise from photoionized neutrals, while prompt ion formation is minimal (~760 counts) after ~12300 laser pulses operating at 2.5 kHz. The detection efficiency of the analyzer has been previously measured to be approximately 8% (see Chapter 3),[19] thus implying that approximately 1.3 x 10^6 ions are formed. Dividing this number by the number of laser pulses, approximately 110 photoionized neutrals are being formed per ToF cycle (one laser pulse). If one assumes an photoionization cross section of 20 x 10^{-18} cm^2 for the desorbed molecules,[24] a flux of 10^{18} photons/(cm^2 s), and an average speed of a desorbed molecule being between 30 m/s and 240 m/s, then the ionization probability is in the range 10^{-5} to 10^{-6}. With this rough estimate, 110 photoionized neutrals indicates the desorption of approximately 5.3 x 10^6 to 5.3 x 10^7 neutral molecules per laser pulse. The relative proportion of desorbed neutrals and ions is consistent with previous observations with MALDI, where the ion-to-neutral ratio is estimated to range from approximately 10^{-3} to approximately 10^{-5}.[24]

The number of molecules desorbed per laser pulse under these conditions is four to five orders of magnitude lower than observed in previous experiments that utilized higher laser peak power (more ablative conditions).[22] With 10^6 to 10^7 molecules desorbed for each ~5 ns laser pulse, the kinetic theory of gases predicts a very low probability for collisions between molecules within the desorbed neutral plume; thus no higher masses due to post-desorption clustering should appear. Furthermore, the shape of the mass features, which consist of a peak followed by an elevated baseline,[25] indicates the continuous desorption of molecules from the surface only during laser irradiation. From this behavior, it can be deduced that the laser desorption is largely due to local laser heating of the sample. Despite the gentle desorption mechanism, chemistry may still be induced on the surface by the added energy from the desorption laser.

Alkali lignin samples are investigated using different sample preparation methods in order to determine whether the act of dissolving the lignin in methanol would affect the observed mass spectrum. Figure 6.9a shows the VUV-LDPI mass spectra that are obtained with dissolved lignin (very small lignin particles) compared to lignin samples that were smeared onto the silicon substrate (Figure 6.9b; both large and small lignin particles). As can be seen, the dissolved samples create uniform and flat samples. The mass spectra show very little elevated baseline following each peak, indicating better thermal conductivity to the underlying silicon substrate. In the less homogeneous sample, large and small particles of lignin are seen, and elevated baselines are clearly visible following each of the most intense mass spectral peaks. These baselines are due to the ionization of a continuous flow of thermally desorbing molecules, indicating that, at least in certain local areas of the sample, there is poorer thermal dissipation to the substrate. This also leads to a higher surface temperature, which results in higher relative intensities of the mass features in the dimer mass region (m/z ~270 to 450). Due to the inhomogeneous nature of the non-dissolved samples and the difficulty of reproducing results reliably from such samples, dissolved samples are used for all other experiments discussed here.

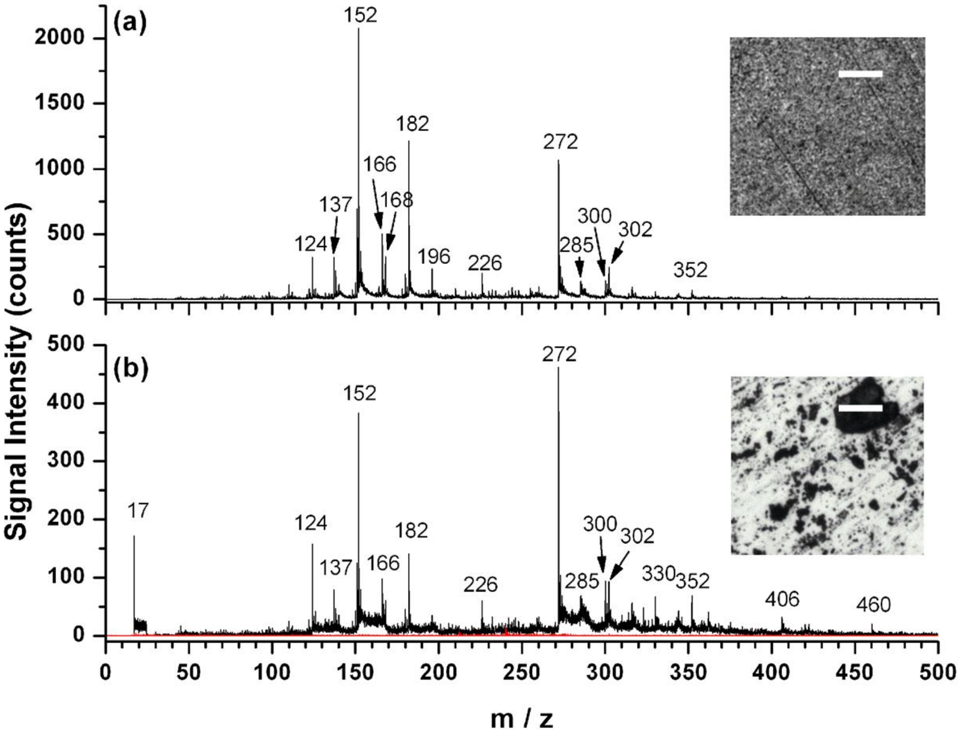

Figure 6.9: VUV-LDPI MS of alkali lignin with two methods of sample preparation, both collected with 10.5 eV ionizing photon energy, 2 mm/s sample scan rate and ~2.4 MW/cm^2 laser peak power density (0.15 µJ/pulse at 8.5 ns pulse width). Scale bars in images are 30 µm.

VUV-LDPI has several advantages over VUV-TD. VUV-LDPI analysis requires much less sample than VUV-TD experiments, and because only a small amount of sample is heated, the mass spectra are less biased toward species that are more volatile. At the same time, VUV-LDPI also preserves volatile species (like ammonia), which are still visible in the VUV-LDPI mass spectra, whereas ammonia is completely absent in the VUV-TD mass spectra that are taken at higher temperatures. This characteristic arises due to the very controlled (time-triggered) nature of the sample heating. Furthermore, because laser desorption occurs only in localized areas of the sample, chemical imaging is possible, and multiple experiments can be performed on the same sample in quick succession. This second property can be exploited to study the kinetics of sample pyrolysis, as is discussed later.

Figure 6.10 shows the VUV-LDPI mass spectra of a commercially-available alkali lignin with 10.5 eV postionization for various desorption laser peak powers. Collected using a sample scanning rate of 2 mm/s and a repetition rate of 2500 Hz, each 30 µm diameter sample area is exposed to an average of ~38 laser pulses. The mass spectra are collected at room temperature (~25 ºC) and do not show any significant background signal from thermally desorbing molecules from the sample surface, from residual gas in the vacuum chamber (synchrotron-only background), or from prompt ion formation. As would be expected from a thermal desorption mechanism, the less volatile higher mass features such as m/z = 272 increase in intensity as the laser peak power is increased. At a laser peak power density of 10 MW/cm^2, the intensities at m/z = 152, 166, and 272 have relative intensities of 0.5:0.13:1.

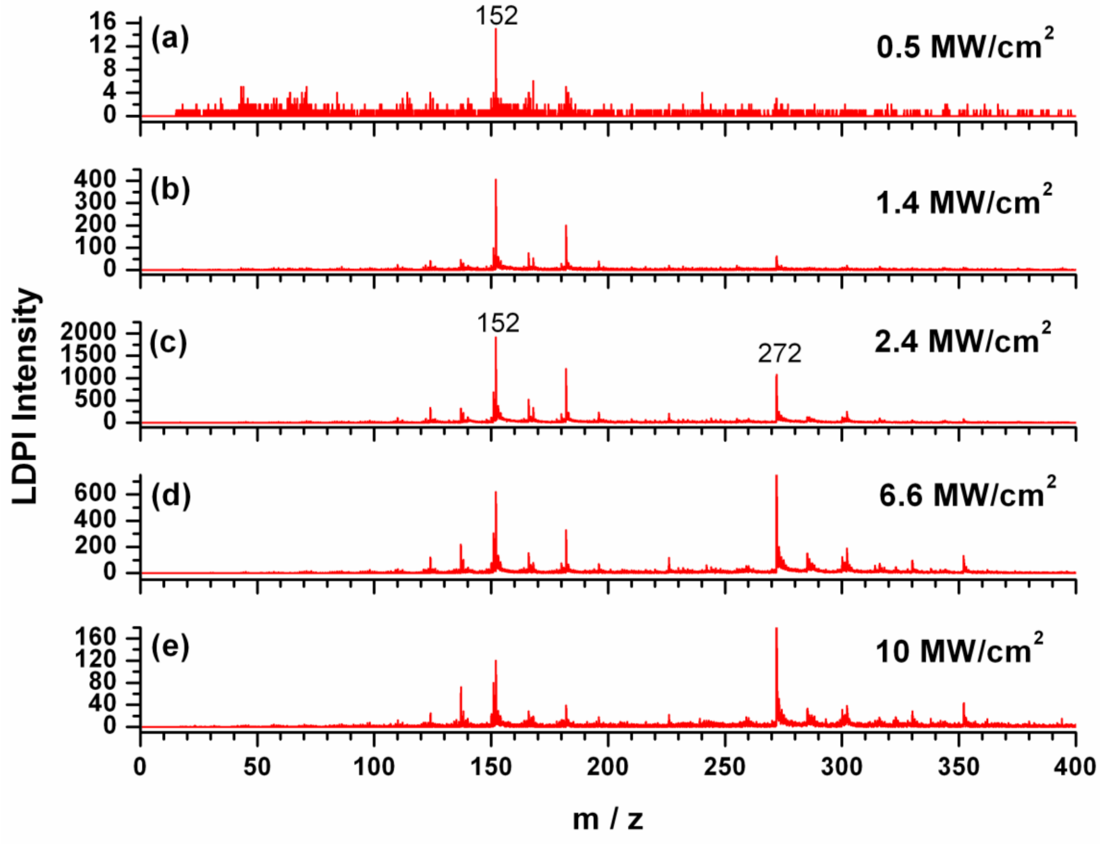

Figure 6.10: VUV-LDPI mass spectra of alkali lignin collected with 10.5 eV postionization and ~38 laser pulses per 30 µm-diameter spot

Figure 6.11 shows the lignin VUV-LDPI mass spectra for a slower scan rate of 0.125 mm/s, where each 30 µm-diameter sample spot is irradiated by an average of 608 laser pulses. The mass spectra are collected such that the spectra from Figure 6.10 and 6.11 analyze the same sample area – the mass spectra of Figure 6.11 have 16 times more pulses (the sample scan rate is 16 times slower) than the spectra of Figure 6.10. All other experimental variables are held constant. At lower laser peak powers (Figures 6.11a-c), increasing the laser dosage appears to again enhance only the thermal desorption of higher mass features. At higher laser peak powers (Figures 6.11d-e), however, it can be seen that the relative intensity of m/z = 272 decreases compared to m/z = 152 with the slower scan rate. With the increased laser dosage, the m/z = 152, 166 and 272 peaks have an intensity ratio of 0.16:0.31:1. This would indicate that either sample damage and/or selective chemical depletion are taking place. Unfortunately, due to the limited dynamic range of the current instrumental setup, it is not possible to quantify the laser peak power dependence of the production of individual mass peaks to determine whether the change could be a result of molecular excitation by multiple photons.

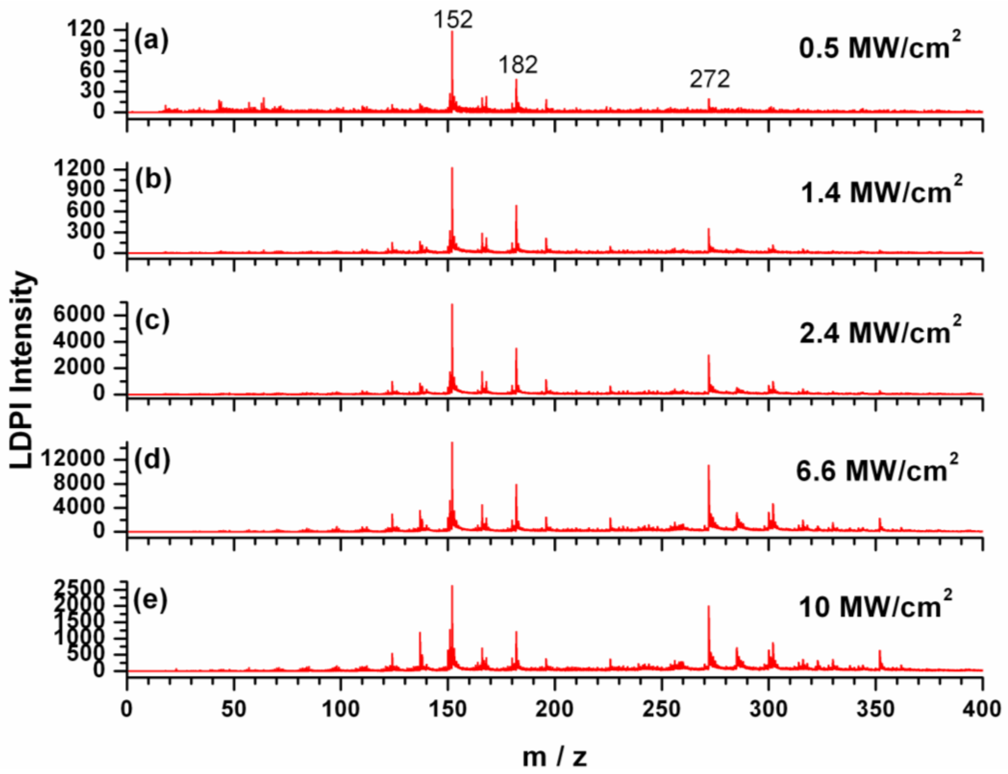

Figure 6.11: VUV-LDPI of alkali lignin at different laser peak powers for 0.125 mm/s scan rate, collected with 10.5 eV postionization

Under optimal conditions, VUV-LDPI is dominated by a thermal desorption mechanism. The differences between VUV-LDPI and VUV-TD data can be explained by the different timescales between the two experiments. In the VUV-TD experiments, the entire sample is heated gradually, so more volatile components (which may be quite minor components within the mixture) dominate the mass spectra at low temperatures, while less volatile components dominate the mass spectra at higher temperatures. In VUV-LDPI, a very local sample area is instantly heated to a high temperature. This results in a more representative mass spectrum wherein both volatile and less volatile species are desorbed at the same time.

6.3.3 Monitoring Chemical Changes upon Laser Pyrolysis

Because the desorption laser deposits thermal energy into the lignin samples in a controlled way, it is possible to monitor the gradual chemical change of lignin (and other) samples upon exposure to specific amounts of laser energy. To study signal decay and the evolution of laser pyrolysis products for lignin and other biopolymers of interest, the laser repetition rate and sample scanning speed are adjusted such that each 30 µm diameter area of the surface are probed by ~4 laser pulses. The same area is analyzed in this way 25 times. The integrated intensity of masses of interest can then be monitored as a function of laser exposure. For lignin, under the low-peak power conditions (~15 MW/cm^2) used here, an exponential decay of all major peaks originally present in the sample can be clearly seen from the curves shown in Figure 6.12. The value of $S_{1/2}$ shown in Figures 6.12a-b corresponds to the number of laser pulses that are required to make the mass signal intensity decrease to half of its original value.

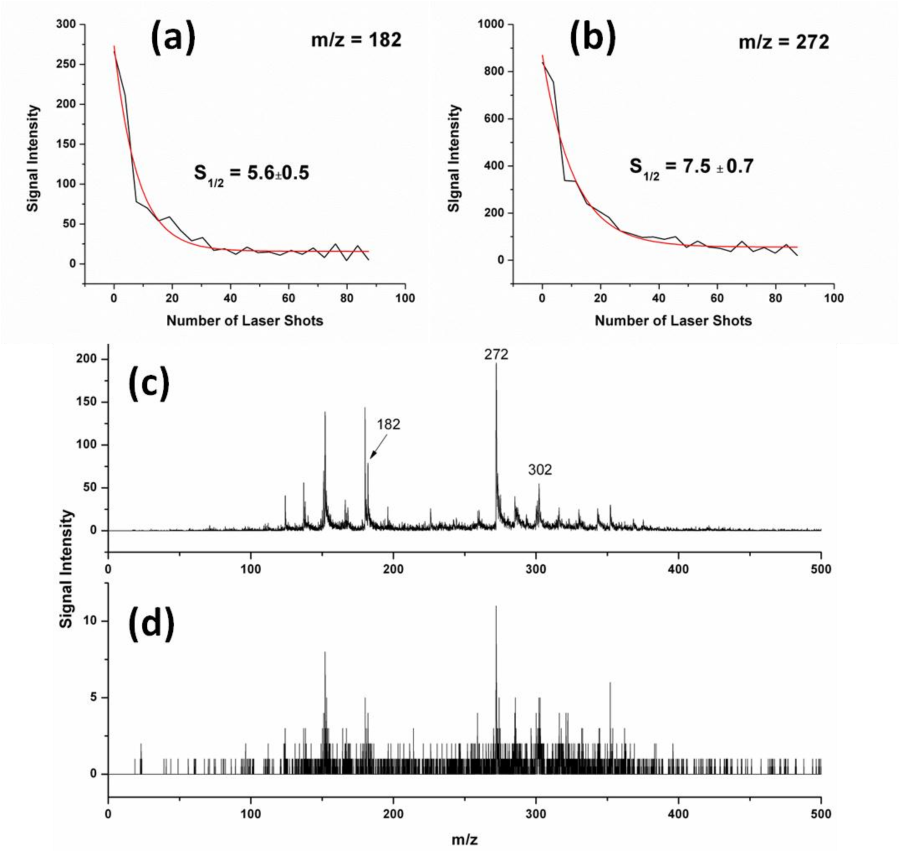

Figure 6.12: Decay of VUV-LDPI signal of (a) m/z = 182 and (b) m/z = 272 from alkali lignin upon laser irradiation with a peak power density of ~15 MW/cm^2. $S_{1/2}$ indicates the number of pulses for the signal to decay to half of its original value. (c) The initial mass spectrum resulting from the first 4 laser pulses and (d) from the last 4 laser pulses after ~85 laser pulses. Some contributions from some residual coniferyl alcohol in the instrument chamber are visible at m/z = 180, 124, and 137 but do not contribute to the signals at m/z = 182 and 272.

While these initial experiments indicate that different molecular species do decay at different rates and can provide a good representation of the original surface composition (Figure 6.12c) the poor signal to noise with increasing laser exposure (Figure 6.12d) makes it difficult to definitively identify the formation of pyrolysis products from specific species in the original sample. Future experiments with more sample averaging, thorough analysis and temperature measurements will be necessary to identify and quantify the formation of new chemical species during lignin pyrolysis. This mass spectral monitoring of pyrolyzed biomass can also be applied to the study of other important plant biopolymers such as cellulose, which has been observed to form very obvious pyrolysis products under the laser conditions typically used in the current apparatus (data not shown).

6.3.4 Structural Differences of Different Lignin Extracts

In analyzing the VUV-LDPI mass spectra of lignin, one question that arises is whether the distribution of peaks can provide any insight into the chemical structure of lignin. To address this question, different lignin samples are investigated, including commercial organosolv lignin (Sigma Aldrich) and organosolv lignin from *Miscanthus giganteus*. These different lignins, being produced by different extraction methods and plant sources, should exhibit different mass spectral patterns.[26] This is due to the fact that different extraction methods perform different chemistry (break different bonds), and various plant species have lignin with different bonding and relative contributions of monomer units.

While certain mass spectral peaks such as the m/z = 152,182 and 272 are shared between the two commercial lignins isolated from woody plants (Figures 6.13a-b), the relative peak intensities are dramatically different. This may be a result of the different extraction methods used. The organosolv lignin from *Miscanthus giganteus* (Figure 6.13c) shows very different mass spectral patterns, possibly due to the fact that it is isolated from a different type of plant (a grass, not a woody plant); thus, while all three samples represent lignin polymer extracts, there are clearly chemical differences among the samples that can be seen by analyzing the mass spectra.

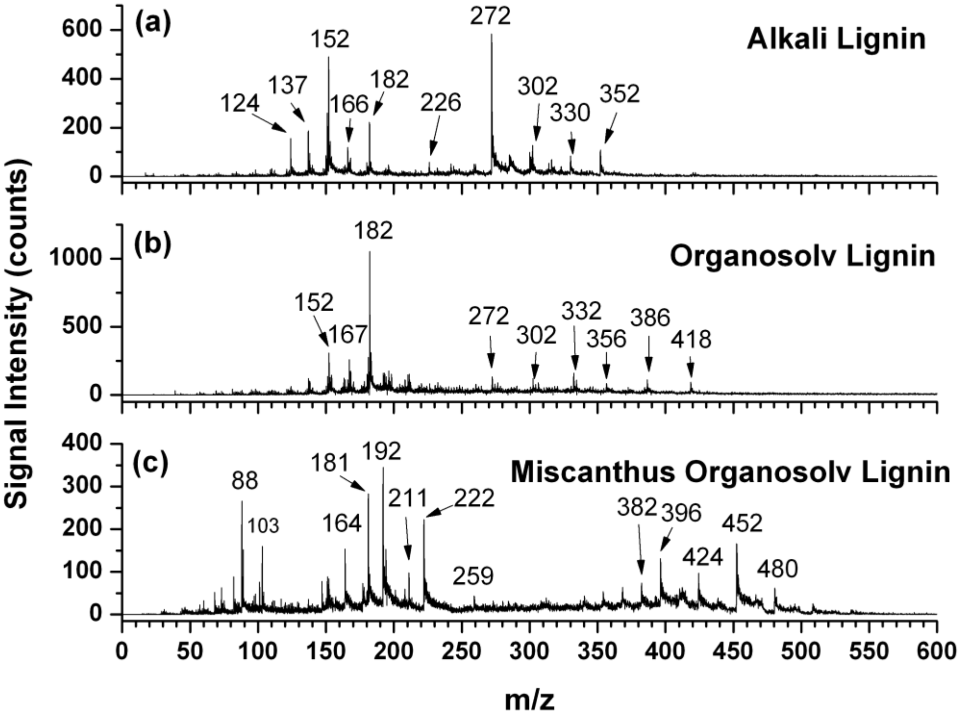

Figure 6.13: (a) VUV-LDPI mass spectra taken with 38 laser pulses / 30 μm-diameter spot of (a) alkali lignin (Sigma Aldrich) collected using a laser peak power density of ~6.6 MW/cm^2, (b) organosolv lignin (Sigma Aldrich) taken with ~16.5 MW/cm^2 and (c) *Miscanthus giganteus* organosolv lignin taken with ~4.2 MW/cm^2.

6.3.5 Assignment of Lignin Oligomers

The VUV-LDPI mass spectra and VUV-TD PIE curves can be used to help determine the dominant structures present in the lignin samples. From additional work (Chapters 5 and 6.3) it is known that the major dissociative photoionization fragments of coniferyl alcohol, a major monomer unit of lignin, are m/z = 124 and 137. Vanillin (m/z = 152) also appears to be a major monomer-like contaminant that may accumulate in the coniferyl alcohol samples from gradual degradation during sample storage, and a mass feature at m/z = 164 also appears in the VUV-LDPI mass spectrum with prolonged laser exposure (see Figure 6.4). M/z = 164 has been previously observed in thermolysis experiments[27] and has been assigned to eugenol and isoeugenol, although this assignment has yet to be verified in VUV-LDPI experiments. All of these structures differ only by the atoms attached to C_1 (see Figure 6.1), and not by the –OH or –OCH_3 groups on the aromatic ring.

Earlier it was noted that m/z = 182 in the alkali lignin mass spectra does not appear to have significant contributions from syringaldehyde (see Section 6.3.2). There are many other possible structures m/z = 182, however, including dihydroconiferyl alcohol. This assignment can also explain the feature at m/z = 166, which could correspond to 4-propylguaiacol, a reasonable fragment of dihydroconiferyl alcohol.

These same fragmentation patterns should also be present in the dimer and other oligomer structures of lignin. As a starting point, m/z = 272, the dominant dimer mass feature, is considered. M/z = 272 has been previously hypothesized to have one of the structures shown in Figure 6.15.[28] Although its exact structure is under debate, it is separated from the next major mass feature, m/z = 285, by 13 mass units, which is the same mass difference between m/z = 124 and m/z = 137. M/z = 285 could correspond to a dissociative photoionization fragment that has a similar structure to m/z = 272 (Figure 6.15) with a -CH_2 group instead of an H. The next peak, m/z = 300, is 28 mass units heavier than m/z = 272. This mass difference is consistent with the difference between m/z = 124 and vanillin. It is therefore feasible that m/z = 300 has an additional CH=O group instead of an H atom.

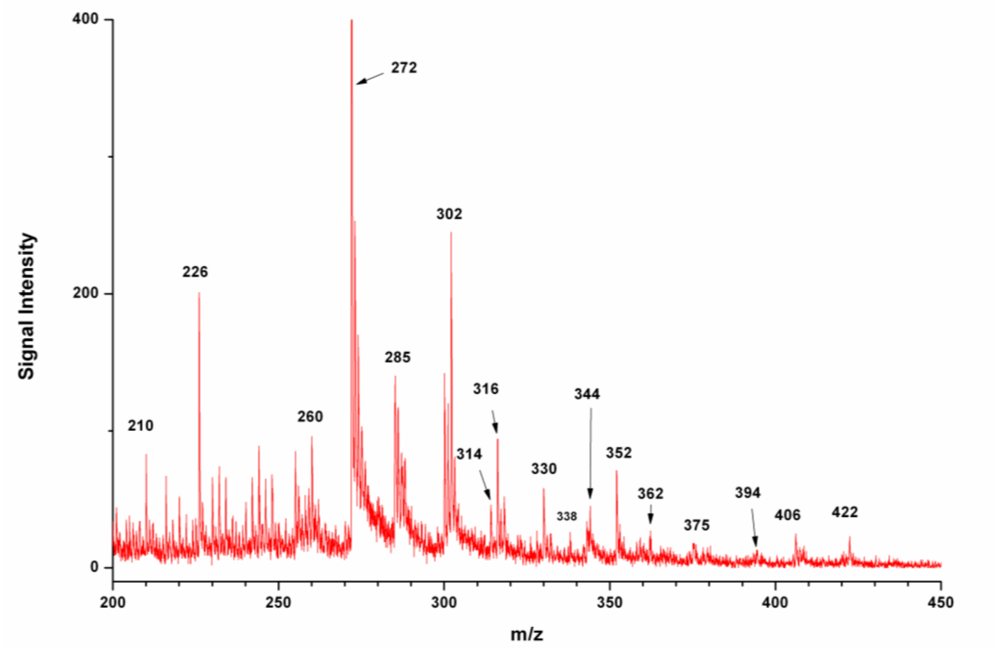

Figure 6.14: Zoomed-in view of the dimer mass region of the alkali lignin VUV-LDPI mass spectrum of Figure 6.9a. The mass feature at m/z = 272 extends beyond the intensity range shown.

Previous groups have suggested that m/z = 272 is likely a guaiacyl-guaiacyl (G-G) dimer.[28-31] If the proposed structure in 6.15d is assumed, it would be capable of having two additional –OCH_3 substitutions at positions R_1 and R_2. The feature at m/z 302 has a mass difference of 30 with respect to m/z = 272, which suggests that it could be a guaiacyl-syringyl (G-S) dimer that has an additional –OCH_3 substituted onto one of the aromatic rings. The near absence of a mass feature at m/z = 332 may indicate that the syringyl-syringyl (S-S) dimer is either highly unstable or not a common unit found in this sample of extracted alkali lignin, since its low intensity cannot be explained by completely random statistical bonding between G and S units. This could also indicate that structure 6.15d is not the dominant structure. In any case, the near-absence of m/z = 332 contrasts with results of other groups by laser desorption ionization (LDI)-MS[30] and pyrolysis field ionization MS.[28,31]

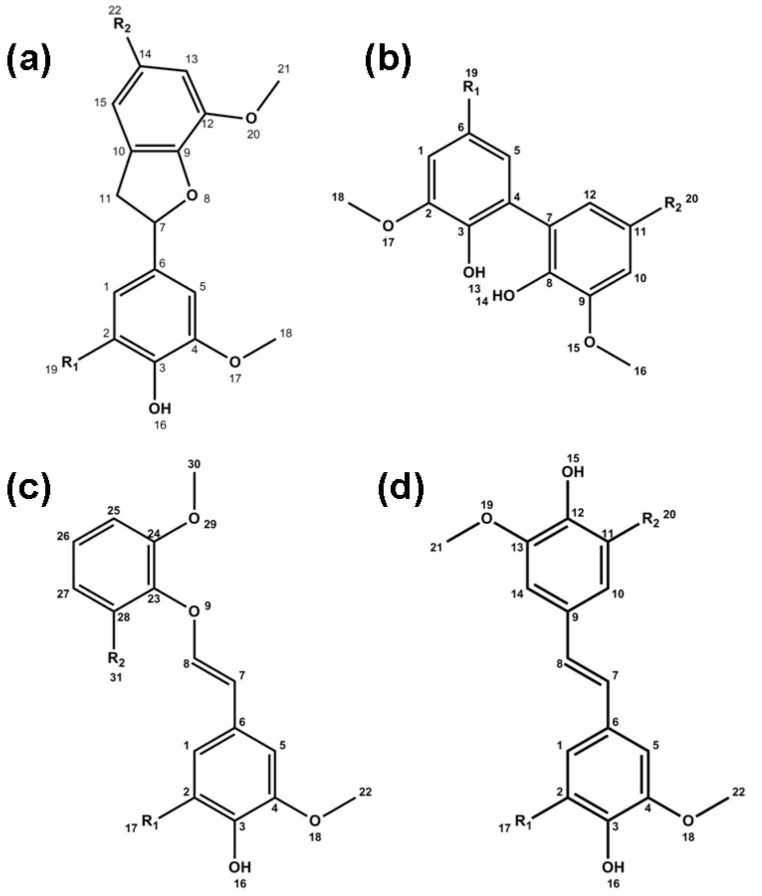

Figure 6.15: Proposed structures for the mass feature at m/z = 272. (a) phenylcoumaran, (b) biphenyl, (c) ether bonded and (d) diarylpropane – type structures. $R_1 = R_2 = H$ for m/z = 272, but they indicate sites for substitution.

To aid in these assignments, additional studies observing the fragmentation patterns of model dimer compounds with linkages found commonly in lignin such as guaiacylglycerol-β-guaiacyl ether are underway. Further structural certainty in the mass assignments can be gained with MS/MS data.

6.4 Conclusions

Coniferyl alcohol, a monomer unit of lignin is used as a case study to examine the effects of laser desorption on lignin model compounds. From the mass spectra and the PIEs and AEs of the major fragments, it is determined that very little internal energy is deposited into the molecules during the desorption process. This contrasts with the measurable internal energy imparted to molecules of similar molecular weight during more ablative laser desorption (~0.8 eV) and ion sputtering by 25 keV Bi_3^+ (~2-3 eV). Coniferyl alcohol also exhibits marked chemical degradation upon prolonged laser exposure, illustrating that the UV desorption laser can induce chemical damage.

Lignin polymers are also investigated. VUV-SNMS and SIMS analysis result in mass spectra that reflect only lignin fragments in the monomer mass range. Thermal desorption with VUV photoionization is used to observe higher mass species that can provide insight into the chemical bonding in the lignin polymer. Comparison of the AE curves of the observed lignin fragments with PIEs of lignin model compounds are used to determine that neutral guaiacol, vanillin and eugenol may be desorbed from the lignin sample. Desorbed neutral syringaldehyde does not appear to be a major contributor to the mass signature at m/z = 182 at 150 °C and 200 °C.

Comparison of VUV-LDPI and VUV-TD mass spectra indicate that many of the same mass signatures are observed using both methods. This observation, plus the observed peak shapes and the increasing high-mass signal intensities with increasing laser power indicate that a thermal desorption mechanism is dominant. A brief calculation shows that the number of molecules in the desorbed laser plume is insufficient for inter-molecular collisions or reactions to occur in the gas phase.

Although gas-phase reactions are not a concern under the experimental conditions used here, the laser is capable of inducing chemical damage. Since the laser is not energetic enough to ionize the surface molecules, this damage likely occurs via homolytic or heterolytic bond cleavage and subsequent surface reactions.[32] This effect of laser pyrolysis on lignin and other important plant biopolymers can be quantified in future experiments with better signal averaging and by observing the change in the relative mass spectral intensities as a function of laser irradiation.

Laser desorption and VUV photoionization is a powerful tool for studying fragile molecular systems such as lignin and other biopolymers because it allows polymer fragments to be detected with minimal fragmentation. With careful tuning of the VUV photon energy and laser power, both spectroscopy and mass spectrometry are used to follow the chemistry of important biopolymers with preserved spatial resolution. Already, the technique has been used to obtain tantalizing mass spectrometry results over ground plant biomass (see Figure 6.16). Despite these developments, there remains much room for improvement. While the identity of small masses in the alkali lignin mass spectrum can be partially inferred from AEs of the fragments (see Section 6.3.2 and Figure 6.7), the chemical formula and the spatial arrangement of the atoms of higher mass species in lignin and other samples cannot be determined presently with much confidence. This problem is made clear when attempting to determine the structure even of the most dominant dimer mass feature at m/z = 272. Additional VUV-LDPI work with model lignin dimer compounds is underway to investigate typical fragmentation patterns that are specific to particular kinds of inter-unit linkages; however studies of model compounds are insufficient for universal identification of hitherto unknown chemical structures.

To achieve its full potential, VUV-LDPI requires improved mass resolution and a better method for determining molecular structure. Accurate determinations of chemical formulas can be obtained by increasing the mass resolution of the current mass spectrometer. In this way, overlapping masses can be distinguished, and the number of oxygen, carbon and hydrogen atoms can be confidently determined by exact mass measurements. More definitive determination of the spatial arrangement of the atoms (isomer form) corresponding to each of the mass features in the VUV-LDPI mass spectra can be achieved by the implementation of multistage mass

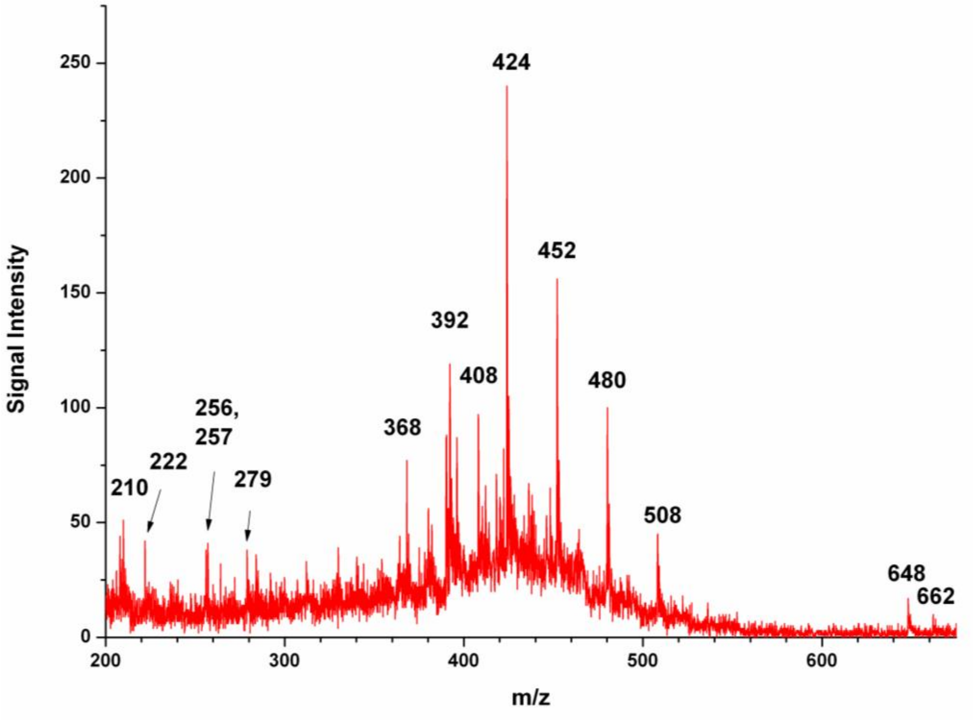

Figure 6.16: VUV-LDPI mass spectrum of ground plant tissue from *Miscanthus giganteus*

spectrometry (MS/MS) techniques. Furthermore, because the current experiments are dominated by a thermal desorption mechanism that results in higher sensitivity to more volatile chemical species, the detection of less volatile components requires greater dynamic range in the detection system. The thermal desorption mechanism, while facilitating studies into biomass pyrolysis, may also cause unintended pyrolysis of other samples during chemical imaging. Such sample degradation can be remedied by using a shorter (ps to fs) laser pulse to desorb molecules before thermal degradation effects manifest. Each of these improvements can drastically increase the utility and analytical power of the VUV-LDPI technique for studying chemical changes within structurally and chemically complicated real-world systems.

References

(1) Grabber, J. H.; Ralph, J.; Lapierre, C.; Barrière, Y. *Comptes Rendus Biologies* **2004**, *327*, 455.

(2) Sticklen, M. B. *Nat Rev Genet* **2008**, *9*, 433.

(3) Li, X.; Bonawitz, N. D.; Weng, J.-K.; Chapple, C. *The Plant Cell Online*, *22*, 1620.

(4) Schmidt, M.; Schwartzberg, A. M.; Perera, P. N.; Weber-Bargioni, A.; Carroll, A.; Sarkar, P.; Bosneaga, E.; Urban, J. J.; Song, J.; Balakshin, M. Y.; Capanema, E. A.; Auer, M.; Adams, P. D.; Chiang, V. L.; Schuck, P. J. *Planta: An International Journal of Plant Biology* **2009**, *230*.

(5) Gupta, R.; Mehta, G.; Khasa, Y.; Kuhad, R. *Biodegradation*, *22*, 797.

(6) Singh, S.; Simmons, B. A.; Vogel, K. P. *Biotechnology and Bioengineering* **2009**, *104*, 68.

(7) Kleinert, M.; Barth, T. *Energy & Fuels* **2008**, *22*, 1371.

(8) Morreel, K.; Dima, O.; Kim, H.; Lu, F.; Niculaes, C.; Vanholme, R.; Dauwe, R.; Goeminne, G.; Inzé, D.; Messens, E.; Ralph, J.; Boerjan, W. *Plant Physiology*, *153*, 1464.

(9) Martin, F.; Saizjimenez, C.; Gonzalezvila, F. J. *Holzforschung* **1979**, *33*, 210.

(10) Saiz-Jimenez, C. *Environmental Science & Technology* **1994**, *28*, 1773.

(11) Morreel, K.; Kim, H.; Lu, F.; Dima, O.; Akiyama, T.; Vanholme, R.; Niculaes, C.; Goeminne, G.; Inzé, D.; Messens, E.; Ralph, J.; Boerjan, W. *Analytical Chemistry*, *82*, 8095.

(12) Saito, K.; Kato, T.; Tsuji, Y.; Fukushima, K. *Biomacromolecules* **2005**, *6*, 678.

(13) Saito, K.; Kato, T.; Takamori, H.; Kishimoto, T.; Yamamoto, A.; Fukushima, K. *Applied Surface Science* **2006**, *252*, 6734.

(14) Goacher, R. E.; Jeremic, D.; Master, E. R. *Analytical Chemistry*, *83*, 804.

(15) Li, Z.; Chu, L.-Q.; Sweedler, J. V.; Bohn, P. W. *Analytical Chemistry*, *82*, 2608.

(16) Lunsford, K. A.; Peter, G. F.; Yost, R. A. *Analytical Chemistry*, null.

(17) Li, Z.; Bohn, P. W.; Sweedler, J. V. *Bioresource Technology*, *101*, 5578.

(18) Gibson, J. K. *Journal of Vacuum Science and Technology* **1995**, *13*, 1945.

(19) Takahashi, L. K.; Zhou, J.; Wilson, K. R.; Leone, S. R.; Ahmed, M. *The Journal of Physical Chemistry A* **2009**, *113*, 4035.

(20) Zhou, J.; Takahashi, L. K.; Wilson, K. R.; Leone, S. R.; Ahmed, M. *Analytical Chemistry* **2010**, *82*, 3905.

(21) Takahashi, L. K.; Zhou, J.; Kostko, O.; Golan, A.; Leone, S. R.; Ahmed, M. *The Journal of Physical Chemistry A*, *115*, 3279.

(22) Kostko, O.; Takahashi, L. K.; Ahmed, M. *Chemistry – An Asian Journal* **2011**, *6*, 3066.

(23) Qi, F.; Sheng, L.; Zhang, Y.; Yu, S.; Li, W.-K. *Chemical Physics Letters* **1995**, *234*, 450.

(24) Akhmetov, A.; Moore, J. F.; Gasper, G. L.; Koin, P. J.; Hanley, L. *Journal of Mass Spectrometry*, *45*, 137.

(25) Gasper, G. L.; Takahashi, L. K.; Zhou, J.; Ahmed, M.; Moore, J. F.; Hanley, L. *Analytical Chemistry*, *82*, 7472.

(26) Pandey, M. P.; Kim, C. S. *Chemical Engineering & Technology*, *34*, 29.

(27) Masuku, C. P. *Journal of Analytical and Applied Pyrolysis* **1992**, *23*, 195.

(28) Izumi, A.; Kuroda, K.-i. *Rapid Communications in Mass Spectrometry* **1997**, *11*, 1709.

(29) Evans, R. J.; Milne, T. A. *Energy & Fuels* **1987**, *1*, 123.

(30) Bayerbach, R.; Nguyen, V. D.; Schurr, U.; Meier, D. *Journal of Analytical and Applied Pyrolysis* **2006**, *77*, 95.

(31) Hempfling, R.; Schulten, H. R. *Organic Geochemistry* **1990**, *15*, 131.

(32) Zhang, X. L.; Li, J.; Yang, W. H.; Blasiak, W. *Energy & Fuels*, *25*, 3739.